# A STUDY OF CROSSFLOW FILTRATION USING DILUTE SUSPENSIONS OF MONODISPERSE SPHERICAL PARTICLES

NIGEL JAMES BLAKE B.Eng. A.C.G.I.

A thesis submitted for the degree of
Doctor of Philosophy of the University of London

Department of Chemical Engineering and Chemical Technology
Imperial College
London S.W.7

## ABSTRACT

A model to predict the steady state permeate flux of a crossflow filter is presented. The model is based on a frictional force balance applied to a particle at the cake surface. The components of hydrodynamic drag and interparticle forces are resolved into two orthogonal directions at the contact point. It is assumed that if the ratio of tangential to normal force exceeds the coefficient of friction, particulate deposition does not occur. An extension of this concept to characterize dynamic filtration performance is suggested. The cake growth rate is assumed to be the product of convected mass rate towards the filter and a sticking factor dependent on permeate velocity and wall shear stress.

The steady state model was tested by filtering monodisperse suspensions of polystyrene spheres in tubular geometry. These buffered suspensions at 0.5wt% solids were composed of particles of 0.55 or 1.8 microns in diameter. The variables investigated were membrane type ( Carbosep and Ceraver tubes ), crossflow ( 0.5 to 9$dm^3min^{-1}$ ), pressure ( 1 to 3 bar ), particle diameter and suspension pH. The model proposes that at steady state, the set of permeate velocity - shear stress co-ordinates, obtained from tests under different operating conditions, should define a straight line. The slope of this equilibrium line is predicted to increase with particle diameter. Experiments confirmed both features of the model. Tests also demonstrated the importance of considering interparticle forces in the frictional force balance. Cake resuspension was only observed at high crossflow, suggesting that the filtration equilibrium was not reversible due to strong particle attractions.

For a given system, the position of the equilibrium line may be determined from a small number of tests. Use of the model then allows solution for all hydrodynamic aspects of filtration performance. Example predictions for a wide range of operating conditions are presented.

ACKNOWLEGEMENTS

I would like to thank the following people for their help and support in the preparation of this thesis.

Annette Alcock and John Cummings for their technical support,

Clive Hamblin for performing the particle size analysis on the Malvern Mastersizer,

Paul Luckham of Imperial College for assistance in the preparation of polystyrene latex,

Chris Hawes of Oxford University for taking the electron micrographs of the latex particles,

my collegues and supervisors at Harwell: Ian Reed, Iain Cumming, Keith Robinson and Richard Gutman for their helpful discussions and suggestions about the work, particularly Iain and Richard for the onerous task of commenting on the text while in preparation,

my supervisor Mike Streat for his guidance during the work and comments on the manuscript,

and Heather for her understanding and encouragement during the time consuming period of writing the thesis.

To Heather

**University of London**
SENATE HOUSE, MALET STREET WC1E 7HU
Tel 01-636 8000 · Fax 01-636 0373

With the compliments of
Examinations Division

TABLE OF CONTENTS


1. INTRODUCTION 10

1.1 Crossflow Filtration: Uses and Problems 10

1.2 Aims of this Study 11

1.3 Structure of Thesis 11

2. FILTRATION MODELS 13

2.1 Concentration Polarization 13

2.2 Alternative Models 15

2.2.1 Axial convection models 16

2.2.2 Shear-induced hydrodynamic diffusion 17

2.2.3 Inertial lift effects 22

2.2.4 Erosion processes 25

2.2.5 Frictional force balances 28

2.3 Summary 34

3. THEORETICAL MODEL OF CAKE DEPOSITION 36

3.1 Equilibrium Conditions 36

3.1.1 Mechanisms of mass transfer 36

3.1.2 Particle force model 39

3.2 Dynamic Performance 49

4. EXPERIMENTAL 55

4.1 Experimental Requirements 55

4.2 Membranes 55

4.3 Experimental Rig 58

4.4 Feed Suspension 60

4.4.1 Manufacture 60

4.4.2 Physical properties 62

4.5 Rig Operations and Experimental Interpretation 67

4.5.1 Run procedures 67

4.5.2 Data evaluation 68

4.5.3 Experimental uncertainties 69

4.6 Experimental Campaigns 72

4.6.1 Steady state behaviour 72

4.6.2 Resuspension effects 72

4.6.3 Dynamic behaviour 73

5. RESULTS AND DISCUSSIONS 74
5.1 Steady State Filtration 74
5.1.1 Monomodal particle distribution 74
5.1.2 Bimodal particle distribution 84
5.1.3 Difficulties in defining the filter cake 88
5.1.4 Data comparison with other theories 95
5.2 Resuspension Effects 103
5.2.1 Technique 103
5.2.2 Observations 104
5.3 Dynamic Filtration 110
5.3.1 Cake growth on a clean membrane 110
5.3.2 Re-establishment of equilibrium 118
5.4 Summary 121

6. PREDICTION OF STEADY STATE FILTRATION 122
6.1 Basis of Solution 122
6.2 Example Predictions 124
6.3 Discussion 137

7. CONCLUSIONS 139

8. SUGGESTIONS FOR FURTHER INVESTIGATION 142
8.1 Steady State Filtration 142
8.2 Resuspension 143
8.3 Dynamic Filtration 143

NOMENCLATURE 144

REFERENCES 147

APPENDIX A Rig Components 150
APPENDIX B Computer Logging Program 152
APPENDIX C Steady State Run Data 156
APPENDIX D Example Calculations 160
APPENDIX E Error Analysis 166

FIGURES


| | | |
|---|---|---|
| 2.1 | Geometric Definitions | 13 |
| 2.2 | Boundary Layer Characteristics for Shear-Induced Hydrodynamic Diffusion | 20 |
| 2.3 | Frictional Force Balance in Simple Geometry | 30 |
| 2.4 | Particle Classification | 32 |
| 3.1 | Frictional Force Balance in Simple Geometry | 40 |
| 3.2 | Frictional Force Balance in Complex Geometry | 41 |
| 3.3 | Forces on a Particle in a Packed Bed | 44 |
| 3.4 | Interparticle Forces | 46 |
| 3.5 | Cross-section of a Membrane Tube | 53 |
| 4.1 | Rig Flow Diagram | 59 |
| 4.2 | Detail of Membrane Housing | 61 |
| 4.3 | Mastersizer Particle Diameter Distributions | 64 |
| 4.4 | Relative Viscosity of Latex as a Function of Concentration | 66 |
| 5.1 | Channel Diameter vs. Crossflow ( Carbosep membrane ) | 76 |
| 5.2 | ( Ceraver 0.1 membrane ) | 77 |
| 5.3 | ( Ceraver 0.2 membrane ) | 78 |
| 5.4 | Permeate Velocity vs. Shear Stress | 79 |
| 5.5 | Permeate Velocity vs. Product of Particle Diameter and Shear Stress | 80 |
| 5.6 | Permeate Velocity vs. Product of Particle Diameter and Shear Stress | 83 |
| 5.7 | Schematic Conditions for Filtration Equilibrium | 84 |
| 5.8 | Influence of Crossflow on the Size Distribution of Deposited Particles | 86 |
| 5.9 | Influence of Equilibrium Lines on Depositing Particles | 87 |
| 5.10 | Development of a Flowing Particle Layer | 89 |
| 5.11 | Correction for Pore Blocking | 94 |
| 5.12 | Rautenbach Analysis : Laminar Sub-Layer Velocity Profile | 100 |
| 5.13 | Rautenbach Analysis : Buffer Layer Velocity Profile | 101 |
| 5.14 | Resuspension : Shear Stress vs. Time | 105 |
| 5.15 | Channel Diameter vs. Time | 106 |
| 5.16 | Effect of Operating Pressure | 109 |

5.17 Permeate Flowrate vs. Time : Influence of Crossflow 111
5.18 Sticking Factor vs. Time : Carbosep Tube & Small Particles 112
5.19 Carbosep Tube & Large Particles 113
5.20 Ceraver Tube & Small Particles 114
5.21 Ceraver Tube & Large Particles 115
5.22 Comparison of Channel Diameter : Measured and Calculated Values 117
5.23 Concentration Effect on Dynamic Permeate Flowrate 119
5.24 Re-establishment of Equilibrium with Changed Crossflow 120

6.1 Channel Diameter vs. Crossflow ( Carbosep Tube ) 125
6.2 Pressure ( Carbosep Tube ) 126
6.3 Particle Diameter ( Carbosep Tube ) 127
6.4 Permeate Flow / Length vs. Crossflow ( Carbosep Tube ) 128
6.5 Pressure ( Carbosep Tube ) 129
6.6 Particle Diameter ( C'sep Tube ) 130
6.7 Channel Diameter vs. Crossflow ( Ceraver Tube ) 131
6.8 Pressure ( Ceraver Tube ) 132
6.9 Particle Diameter ( Ceraver Tube ) 133
6.10 Permeate Flow / Length vs. Crossflow ( Ceraver Tube ) 134
6.11 Pressure ( Ceraver Tube ) 135
6.12 Particle Diameter ( C'ver Tube ) 136

D1 Cake Mass vs. Time 164

PLATES

3.1 Streamlines and Timelines in a Boundary Layer 50
3.2 Streamlines and Timelines in a Boundary Layer 51

4.1 Electron Micrographs of a 0.2 micron Ceraver Membrane 57
4.2 Electron Micrographs of Latex Particles 63

TABLES


| | | |
|---|---|---|
| 2.1 | Comparison of Lift Velocities | 25 |
| 4.1 | Comparison of Membrane Characteristics | 56 |
| 5.1 | Cake Voidage for Small Particle Experiments | 82 |
| 5.2 | Pore Blocking Correction | 93 |
| 5.3 | Height of Concentration Boundary Layer | 97 |
| D1 | Calculation of Cake Mass | 163 |
| D2 | Calculation of Sticking Factor | 165 |


ADDENDA

1. S.I. units are used for calculations throughout this thesis, though values are sometimes quoted in more convenient units.

2. A Kozeny constant of 5 has been assumed for calculation of specific cake resistances, thus the version of the Carmen-Kozeny equation used is

$$r_c = 180\ (1 - e)^2 / d_p^2\ e^3$$

CORRIGENDA

1. p.21, line 7: the inequality should read

$$a\tau/\mu_o v_w < 120$$

2. p.24, line 14: replace 'or' with 'and'

3. p.24, last line: delete 'of'

4. p.48, line 3: delete 'fluid viscosity'

5. p.84: no text is missing at the fourth line

6. p.93, table 5.2: for run 50, $r_c = 8.9 \times 10^{14} m^{-2}$

7. p.95, equation 5.8: the denominator should be $\Phi_b \mu_o^3 x$

8. p.139, para.4, first line: insert 'on' after 'locus'

9. p.148, ref.38: the journal number should be 44(3)

# CHAPTER 1

# INTRODUCTION

## 1.1 Crossflow Filtration: Uses and Problems

Pressure-driven membrane processes fall into three main categories: reverse osmosis, ultrafiltration and microfiltration. Although all three operations are concerned with the removal of suspended or dissolved matter from a liquid stream, they are differentiated by the size of the solute species. Reverse osmosis, a diffusion-based process, is used for removal of dissolved ions or molecules; ultrafiltration for separation of macromolecules or small colloids; and microfiltration for removing suspended matter of 0.1 microns upwards. In practice, the terminology and equipment are partially shared, and distinction between the operations is blurred. The term crossflow filtration is applied to ultrafiltration and microfiltration processes where the liquid stream flows tangentially along the membrane.

Crossflow filtration is a relatively new process of growing importance, allowing separation of smaller particles compared to dead-end filtration. Primary uses for this technology include clarification of wine and fruit juice; treatment of industrial wastewater; and concentration of materials such as fermenter broths or latex particles used for adhesive manufacture. One of its advantages over dead-end filtration is that thinner filter cakes are formed, enabling permeate flowrate to be maintained at acceptable levels. Despite the improvement, crossflow filtration does have operational problems because of cake formation. It is generally accepted that the shear stress associated with tangential flow is responsible for keeping the cake growth to a minimum, however the exact action of the shear stress is largely ill-defined. For optimal operation of a filtration unit, a more precise understanding of the relationship between crossflow, pressure and cake formation is needed. The problem is addressed in this work.

For further information on the nature of crossflow filtration, equipment and techniques used, together with the principal applications, the reader is directed to the recent books by Murkes and Carlsson [1] and Gutman [2].

## 1.2 Aims of this Study

As explained in the previous section, the shear stress inherent in the crossflow process is responsible for minimizing cake growth. To date there has been little work to formulate that effect into a model which can predict the performance of a crossflow filter for a variety of operating conditions. The primary aim of this study was to develop such a model, whereby a knowledge of process operating conditions ( such as crossflow, pressure and geometry ) and nature of the suspension ( particle size and concentration ) allows estimates of the performance of a crossflow unit to be made.

In order to assess the effects of shear and other operational parameters, experimentation was conducted with the following restrictions: the membrane was of tubular, ceramic type; the suspension used was composed of spherical, monodisperse particles; and the concentration remained dilute. Use of these conditions allowed the fundamental influences in crossflow filtration to be studied without the complication of non-ideal suspensions.

## 1.3 Structure of Thesis

The description of the work of this thesis falls into the seven following chapters.

2. Previous work concerning cake deposition and models for crossflow filtration are reviewed, with particular respect to the experimental conditions used in this study.

3. A model of steady state membrane performance is proposed, which is based on a balance of interparticle and hydrodynamic forces acting

on depositing particles. The extrapolation to dynamic performance is suggested.

4. All experimental details are described: the membranes used, the test rig, manufacture and properties of the suspension, operational procedures and the scope of experimental campaigns.

5. The results are discussed with respect to the proposed model in three main sections: steady state performance, cake erosion effects and dynamic filtration. The superiority of the force model over the theories reviewed in chapter 2 is demonstrated.

6. Using only one empirical parameter in the force balance model, predictions of filtration performance are made for a wide range of operating conditions.

7. Conclusions are drawn concerning the success and applicability of the model.

8. Further directions for validation and extension of the model are suggested.

# CHAPTER 2

## FILTRATION MODELS

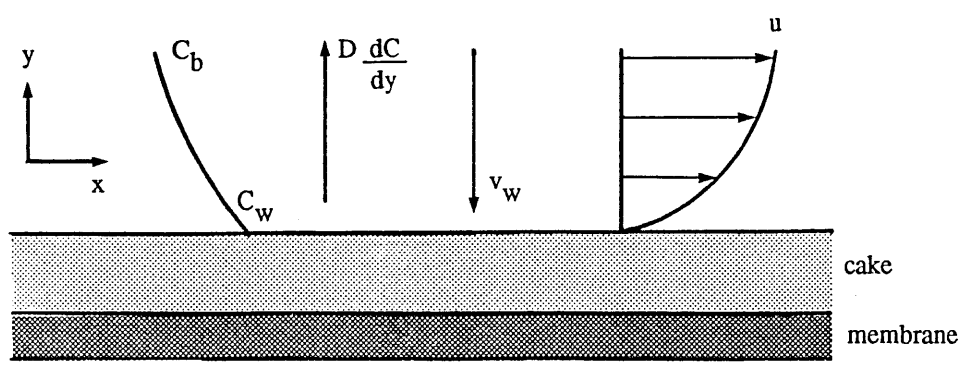
This chapter is divided into three major sections. In the first, the traditional approach to membrane filtration is outlined. This is based on a mass balance of the suspended species, whereby at steady state, mass transfer due to forced convection is balanced by diffusive back-transport. Difficulties in applying this to particulate systems are explained, which leads into the second section where alternative models for crossflow filtration are reviewed. A summary of the important features of each model completes the chapter.

### 2.1 Concentration Polarization

Early work in membrane filtration, which was primarily reverse osmosis or ultrafiltration, modelled the process on a balance between convective mass transport of the dissolved species and diffusive mass transfer back into the bulk [3]. Steady state is reached when these two fluxes became equal due to a drop in permeate flow, which results from an accumulation of solute species at the membrane wall. The crossflow process is illustrated in figure 2.1.

FIGURE 2.1

GEOMETRIC DEFINITIONS



The general mass conservation equation is given by

$$\frac{DC}{Dt} = D\nabla^2 C \qquad (2.1)$$

This may be simplified by neglecting axial convection and axial diffusion which are considered small compared to the normal transport rates. Fully developed flow and constant physical properties are assumed. The mathematical formulation for figure 2.1 can then be expressed

$$vC = D\frac{dC}{dy} \qquad (2.2)$$

where v is the normal velocity, C the concentration of suspended species and D the diffusion coefficient. Upon integration in a geometry with a small radius of curvature compared to the boundary layer dimension ($\delta$), equation 2.2 becomes

$$v_w = \frac{D}{\delta}\ln(C_w/C_b) \qquad (2.3)$$

where $C_w$ and $C_b$ are the wall and bulk concentrations and $v_w$ is the magnitude of permeate velocity at the wall ( permeate flux ). In this analysis, the flux is independent of pressure or membrane resistance, as the concentrated solute layer at the wall ( the so-called gel layer for macrosolutes ) will adjust such that equilibrium is re-established.

It should be noted that the term $D/\delta$ is equivalent to the film theory mass transfer coefficient. Use of a suitable correlation, such as a Leveque solution for laminar flow [4] or the Dittus-Boelter correlation for turbulent flow [5] enables the solution of 2.3. Both these correlations give expressions of the form

$$Sh \sim Re^{k1}\, Sc^{k2} \qquad (2.4)$$

For the turbulent case k1 = 0.8, while in laminar flow k1 = 0.33. Many more correlations for mass transfer coefficients are to be found in the literature: Gekas and Hallstrom [6] presented a comprehensive review of these alternatives, based not only on the momentum-heat-

mass analogy, but on eddy diffusion, surface renewal, coherent turbulent structures and three zone boundary layer concepts. Many of the correlations were developed from experiments with solid walls, but Gekas and Hallstrom outline suggestions to extend the correlations to porous walls.

The exponent on Reynolds number in equation 2.4 gives the dependence of flux on crossflow velocity, which the Leveque and Dittus-Boelter correlations suggest should be 0.33 or 0.8 for laminar and turbulent flow respectively. Belfort and Altena [7] reported that in many instances this exponent varies between 0.3 and 2.0. This seems to suggest that diffusional mass transfer is not entirely responsible for limiting the flux.

Concentration polarization ( CP ) analysis appears to work well for macromolecular solutions in ultrafiltration where the diffusion coefficient is fairly large. This is despite Anderson's finding [8] that the diffusion coefficient for macromolecules is greatly reduced at high concentration. When applied to filtration of particulate suspensions, where the diffusion coefficient is evaluated by the Stokes-Einstein formula, the predicted flux from CP theory is one or two orders of magnitude too low [9]. This has been termed the "flux paradox for colloidal suspensions". Many workers have suggested that other effects must account for the back-transport of particles. These theories are reviewed in the following section.

## 2.2 Alternative Models

As this thesis is concerned with crossflow filtration of particulate matter, attention is now focussed on that system. Alternative models to concentration polarization describing flux behaviour of suspensions fall into five broad categories.

(i) Convection towards the membrane is balanced by axial convection of a flowing cake layer.

(ii) The back-transport mechanism is not Brownian diffusion,

but a process termed "shear-induced hydrodynamic diffusion".

(iii) Lift forces operate on particles in a shear field, which causes migration away from the membrane.

(iv) Simultanous erosion of the filter cake matches the convective flux towards the cake.

(v) Deposition of particles onto the filter cake is inhibited by fluid drag forces operating tangentially along the cake.

Each of these possible mechanisms will now be considered in some detail.

### 2.2.1. Axial convection models

Solution of the general mass conservation equation (2.1) takes different forms according to the simplifying assumptions made. The importance of retaining the axial convection terms was indicated by Blatt et.al. [10] but this form of solution was ignored until Leonard and Vassilieff [11] solved the following form of equation 2.1 by the method of characteristics.

$$\frac{DC}{Dt} = 0 \qquad (2.5)$$

They ignored all diffusion terms and suggested that the rate of convection perpendicular to the membrane is balanced by axial convection of a uniformly concentrated layer. A linear velocity profile in the concentrated layer was assumed, together with a cake viscosity equal to that of the bulk suspension. The height of the flowing layer is expressed in terms of system velocities and concentrations. Steady state is reached when the convective terms become equal.

The part of the analysis which allows a static filter cake to form depends on that cake having Bingham plastic properties. It was proposed that a stationary cake forms if, at the outset, the wall

shear stress is less than cake's yield stress. Upon further build-up of cake the channel diameter is reduced, giving rise to a higher shear stress which approaches the yield value. Erroneously, Leonard and Vassilieff implied that a flowing layer would form on the static cake once the shear stress at the cake / suspension interface exceeded the yield point. This proposal is not consistent with the fact that the shear stress in a tube is highest at the wall. A Bingham fluid would therefore yield at the wall, not at the cake / suspension interface.

Birdsell [12] and Davis and Birdsell [13] extended the convection analysis of Leonard and Vassilieff [11] by proposing parabolic velocity profiles for both the bulk suspension and the flowing cake. The assumption of equal viscosity of the cake and suspension was also relaxed. Their predictions for the height of the flowing cake as a function of axial position were tested with 200 micron spheres suspended in glycerol. Reasonable agreement was demonstrated, but the particles used were so large that the cake layer developed at the end of the filter was always less than 4 particles thick. These experiments cannot be considered an appropriate way of demonstrating the theory.

The main weakness of the convection models is their inability to make predictions of static filter cake formation without applying very restrictive conditions on the nature of the cake. In most crossflow processes the filtration performance is not affected by loosely packed flowing layers, but by static deposits of much higher hydraulic resistance. These convection models, predicting the formation of flowing cake layers, are of limited use in understanding the significant mechanisms of performance loss.

### 2.2.2. Shear-induced hydrodynamic diffusion (SIHD)

This process originates from the complex motion of particles in a concentrated suspension subjected to a shear flow. Each particle rotates, thus exerting drag on its neighbours, and particles in one streamline pass those moving on a slower streamline. These

interactions and mutually induced velocity fields produce a net lateral transport due to random motion of particles which, in its operation down a concentration gradient, is analogous to Fickian diffusion.

Some of the earliest evidence for SIHD comes from studies examining the behaviour of red blood cells. Bernstein et.al. [14], studying haemolysis, correlated the red cell diffusion coefficient as a function of shear rate G as follows ( the red cell radius is 4.2 microns )

$$D = 1.2 \times 10^{-12} G \tag{2.6}$$

Eckstein et.al. [15] measured the SIHD coefficient for spherical particles as a function of concentration and scaled the results

$$D = 0.1 \Phi a^2 G, \quad \text{for } \Phi < 0.2 \tag{2.7}$$

$$D = 0.025 a^2 G, \quad \text{for } \Phi > 0.2 \tag{2.8}$$

where $\Phi$ is the volume fraction of particles and a is the particle radius. Radioactive labelling was used to monitor the lateral position of particles. The smallest particle used in the experiments had a diameter of 1000 microns and the maximum shear rate ( though experimental details are sparse ) appeared to be $1 s^{-1}$.

Ten years later, Leighton and Acrivos [16] used a rather different technique to estimate the SIHD coefficient. They measured the viscosity of concentrated suspensions as a function of time and attributed its progressive decline to a diffusive migration of particles from the gap in a Couette viscometer. The particles used were of 46 and 87 microns diameter, and the maximum shear rate was $76 s^{-1}$. The result was expressed

$$D = k \frac{\Phi^2}{\mu} \frac{d\mu}{d\Phi} G a^2 \tag{2.9}$$

where k is a coefficient with a dependence on concentration ( having values of 0.3 - 1.0 between volume fractions of 0.25 and 0.50 ). The relative viscosity of their suspension ( to the suspending fluid ) was found to be

$$\mu_r = 1 + \left[\frac{0.5\,[\mu]\,\Phi}{1 - \Phi/\Phi_m}\right]^2 \qquad (2.10)$$

where $[\mu]$ is the intrinsic viscosity of the suspension ( defined as $d\mu / d\Phi$ as $\Phi \rightarrow 0$ ), and $\Phi_m$ is the maximum volume fraction of particles ( taken to be 0.58 ).

Based on the above work, it has been suggested that SIHD is the dominant mechanism of back-transport in filtration of particulate systems. Zydney and Colton [17] replaced the Brownian diffusion coefficient in equation 2.3 by the expression of equation 2.7 and then solved for flux using a Leveque solution. Their result suggested that flux is proportional to shear rate to the first power. This result is not particularly useful, as shear rate varies with viscosity over a concentration boundary layer.

Davis and Leighton [18] analysed the one dimensional transport equation in laminar flow rather more rigorously, using the diffusion coefficient of equations 2.9 and 2.10. They allowed for the variation of viscosity across the concentrated particle layer and solved for the concentration profile in the form

$$I(\Phi, \Phi_w) = \frac{v_w \mu_0}{a^2 \tau}\, y \qquad (2.11)$$

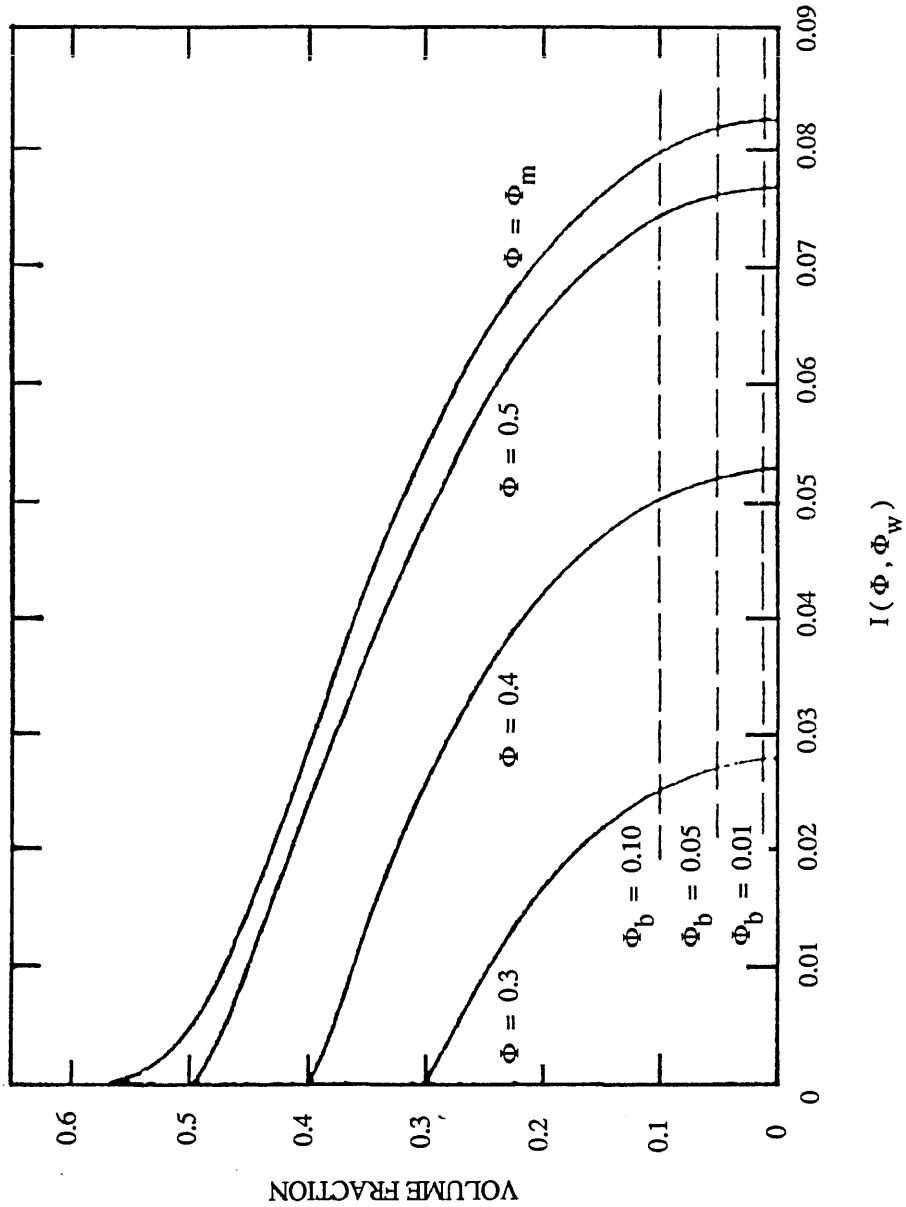
where I is an integral of diffusive and viscous properties between the limits of $\Phi$ and $\Phi_w$ ( I is really a dimensionless distance from the wall ), $\mu_0$ is the permeate viscosity and $\tau$ is the shear stress. $\Phi$ is plotted against I in figure 2.2 for different values of wall and bulk concentrations. It must be pointed out that figure 2.2 shows a discontinuous concentration profile at the edge of the boundary layer.

FIGURE 2.2

BOUNDARY LAYER CHARACTERISTICS FOR

SHEAR INDUCED HYDRODYNAMIC DIFFUSION

Reproduced with permission from ref. 18



An important assumption is that the dimension of the concentrated layer is large compared to the particle size. As an approximation, it might be argued that this assumption is violated when the ratio of boundary layer thickness to particle size falls below 10. From figure 2.2 it is seen that the maximum value of I is 0.083, therefore ( referring to equation 2.11 ) the model breaks down when $a^2 \tau / \mu_o v_w < 120$. This may easily happen in typical microfiltration systems.

The formation of a static cake beneath the flowing layer is allowed if the flux is sufficiently high to drive the wall concentration to the maximum limit. Cake continues to build until the permeate flux is reduced by the growing hydraulic resistance and the convective and diffusive transport become equal.

The approach of Leighton and Davis [18] was to evaluate the formation and nature of a concentrated layer on a membrane surface rather than to make performance predictions for filtration systems. Romero and Davis [19] extended this method to allow prediction of filtration performance by integrating the SIDH equations over the membrane length. The extended model was not supported by experimental data.

While shear-induced diffusion seems to be a physically plausible way to explain the flux paradox for filtration of colloidal systems, there must be some uncertainties in its application. Firstly, the diffusion coefficients are based on some limited work with deformable blood cells or with much larger particles than are of interest to membrane filtration. It is possible that the diffusion coefficients will scale with $a^2 G$ down to micron-sized particles, but this has not yet been demonstrated. Also, there is some uncertainty over the assumption that the thickness of the concentrated layer is always significantly larger than typical particle dimensions. If this is not true, then an analysis based on a concentration profile must break down. Thirdly, all analysis of the fluid flow has been restricted to laminar profiles: in typical tubular systems the boundary layer is turbulent. The mixing associated with turbulence would destroy the regular concentration

gradient, upon which the model is based.

### 2.2.3 Inertial lift effects

Particle migrations in shear flows have been observed for many years. Segre and Silberberg [20] reported that, in 1836, Poiseuille found depletion of blood cells from the wall in capillary flow. They themselves noted that neutrally buoyant, spherical particles in Poiseuille flow migrated to an equilibrium position at about 60% of the distance to the tube wall from the axis.

The Magnus effect, used by spin bowlers and tennis players, originates from particle rotation. A pressure differential across the particle arises from the rotation, and a lift force is thereby generated. Rubinow and Keller [21] developed an expression for that lift force on a spinning particle in a quiescent fluid

$$F_l \approx \Pi \sigma_f a^3 \underline{\Omega} \times \underline{v} \qquad (2.12)$$

where $\sigma_f$ is the fluid density, $\underline{\Omega}$ and $\underline{v}$ are the angular and linear velocity vectors.

Lift forces arising from inertial effects apply to particles without the need for rotation. The creeping flow equations fail to predict lift on a sphere in shear flow; however, Saffman [22] retained the inertial terms in the Navier-Stokes equations and obtained an expression for the lift force on a sphere in an unbounded shear flow

$$F_l \approx 6.46 \mu_o u a^2 (\sigma_f G / \mu_o)^{1/2} \qquad (2.13)$$

where u is the fluid velocity. Saffman also suggested that unless the angular velocity of the particle is much greater than the shear rate, the lift force due to rotation is at least an order of magnitude less than that due to inertial effects. High angular velocities are unlikely in a simple shear flow: Clift's analysis [23] of work by Jeffrey [24] suggests that $\Omega \approx G / 2$.

None of the above mentioned studies considered the presence of boundaries in the analysis of lateral migration effects. Cox and Brenner [25] first introduced this added difficulty into the calculation of lift forces and velocities. The work was subsequently developed by Vasseur and Cox [26], who calculated the lift velocity of a particle in a shear flow bounded by a solid wall.

An early application of lift forces to account for particle back-transport in membrane filtration was an intuitive work by Green and Belfort [27]. They reported that all the expressions for lift velocity, whether experimental or theoretical, take a similar form

$$v_l \sim u_t \, Re \, (a/r_o)^n \, f(r) \qquad (2.14)$$

where $u_t$ is the mean tube velocity, $r_o$ the tube radius, r the radial position and n is approximately 3. To build up a filtration model, they assumed that the expressions for lift velocity and permeate flux could be added to produce a net particle flux. Cake was deemed to accumulate on the membrane surface until its hydraulic resistance ( calculated by the Carmen-Kozeny equation ) reduced the permeate flux to the same value as the lift velocity. It was claimed that the quadratic relationship between steady state flux and axial tube velocity matched experimental results.

A variation of this approach was examined by Belfort et.al. [28]. They used equation 2.2, the solute mass balance equation, but replaced the convective term $v_w$ by $v_w - v_l$. Substitution of the lift velocity expressions for $v_l$ and solution by the Leveque method gave the result

$$v_w = k_1 \, u_t^{0.33} \ln (C_w/C_b) + k_2 \, u_t^2 \qquad (2.15)$$

Results in the literature for the relationship between $v_w$ and $u_t$ take the form $v_w \sim u_t^n$ , where n lies between 0.3 and 2. It was proposed that the relative importance of the two terms on the right of equation 2.15 could account for the observed range of exponents on tube velocity.

Both of Belfort's previous models [27,28] assumed that the porosity of the membrane wall made little difference to the lift velocity compared to systems with solid walls. Two subsequent works by Altena et.al. [29,30] rigorously adapted the solid wall solution to a porous wall. In [30], the solution illustrated was Poiseuille flow between parallel plates, one of which is porous. The lift velocity was given by

$$v_l = Re_p K^2 u_t f(\beta) \qquad (2.16)$$

where $Re_p$ is the particle Reynolds number based on the tube velocity, K is the ratio of particle radius (a) to channel dimension ($d_f$) and $f(\beta)$ is a particular function of a non-dimensional channel position ( which takes a maximum value of 1.5 at the porous boundary ). It was concluded that the lift and permeate velocities could be added if $v_w / u_t \approx Re_p K^2$. The cases where this is not valid are when the lift or permeate velocities have widely differing values.

The major problem with the application of lift forces to membrane filtration is that, under most circumstances, the predicted lift velocity is very small. Altena et. al. [29] presented the following data, estimating the importance of lift to permeation velocity for various of crossflow systems ( $v_w = 4x10^{-5} m\ s^{-1}$ ).

TABLE 2.1

COMPARISON OF LIFT VELOCITIES

| SYSTEM | $d_f$ (mm) | $u_t$ (m $s^{-1}$) | a (μm) | $v_w$ / $v_l$ |
|---|---|---|---|---|
| Hollow fibre | 0.1 | 0.1 | 0.1 | $4x10^4$ |
| | | | 1 | 40 |
| | | | 10 | 0.04 |
| Flat plate | 1 | 0.5 | 0.1 | $2x10^5$ |
| | | | 1 | 200 |
| | | | 10 | 0.2 |
| Tubular | 10 | 1.5 | 0.1 | $2x10^6$ |
| | | | 1 | $2x10^3$ |
| | | | 10 | 2 |

It is seen that for all ultrafiltration and most microfiltration systems, the lift velocity is negligible compared to permeation velocity. Even if the lift velocities were higher, two theoretical problems remain: the lift analysis has only been evaluated for infinitely dilute suspensions; and at distances from the porous wall of less than 3% of channel dimension, the complex integration technique to find $f(\beta)$ breaks down.

### 2.2.4. Erosion processes

(i) Shear-based erosion

Another possibility for reaching steady state in the filtration of particulate matter is that erosion of filter cake eventually balances convective deposition. Concerned with developing a model of thermal surface fouling, Kern and Seaton [31] proposed that the rate of deposit removal was due to the action of the fluid shearing planes of weakness in the fouling layer. It was assumed that these weak

planes had an even distribution through the layer. These assumptions result in a rate of dirt removal that is proportional to the product of shear stress and deposit thickness.

Schulz and Ripperger [32] applied this erosion process to membrane filtration, equating convective flux with Kern type erosion. Their result is that $v_w \sim u_t^{\,k}$ , where k = 1 for turbulent flow and 0.5 for laminar flow. The turbulent case was supported by data from filtration of oil-water emulsions.

Fane et.al. [33] used a similar concept for the removal of deposited matter. Their "scour model" stipulates that the rate of mass removal is given by the product $K_e$ G, where $K_e$ is an erosion coefficient which depends on solid concentration ( $K_e \sim C_b^{\,n}$ ) and the shear rate G is dependent on crossflow velocity. A mass balance equating the convective flux with the rate of scour gives the steady state permeate flux in the form

$$v_w \sim C_b^{\,k1}\, u_t^{\,k2} \qquad (2.17)$$

An intuitive extension of this idea was proposed by Fane [34], where the effects of Brownian diffusion, lift forces and scouring action are all responsible for back-transport. Fane proposed that these mechanisms may be added thus

$$v_w = k_1 \ln(C_w / C_b) + k_2 v_l + k_3 C_b^{\,k4}\, u_t^{\,k5} \qquad (2.18)$$

(ii) Turbulent bursts

Direct observation of flow in the boundary layer has been made in many studies ( notably Fage and Townsend [35], Kline et.al. [36] and Corino and Brodkey [37] ). These workers have all reported that the flow in the viscous sub-layer is not laminar, but subject to random velocity fluctuations: particles are suddenly ejected back into the turbulent core from very close to the wall. In a series of papers, Cleaver and Yates [38,39,40] modelled the deposition and re-entrainment of particles using this turbulent burst phenomenon. From the data of other studies they scaled the turbulent burst parameters

to be dimensionless as follows

| | | |
|---|---|---|
| lateral spacing | $135\mu/\sigma_f u^*$ | (2.19) |
| axial spacing | $630\mu/\sigma_f u^*$ | (2.20) |
| burst diameter | $20\mu/\sigma_f u^*$ | (2.21) |
| time between bursts | $75\mu/\sigma_f u^{*2}$ | (2.22) |

where $u^*$ is the friction velocity, $(\tau/\sigma_f)^{1/2}$. By arguments assuming a random distribution of bursts, Cleaver and Yates calculated the rate of surface cleaning.

Gutman [41] used the technique of Cleaver and Yates applied to membrane filtration, calculating the steady state flux for reverse osmosis membranes in terms of a mass balance between convection and turbulent burst removal, assuming that all the deposited mass under a burst was re-entrained. Knibbs [42] had some success with this model when applied to ultrafiltration of a ferric hydroxide floc, where the rate of mass re-entrainment was found to be the product of a bursting rate coefficient and deposited mass. The bursting rate coefficient appeared to be an increasing function of crossflow.

The prime assumption of these models is that the turbulent burst, upon reaching the surface of the deposited layer, has enough energy to remove all of the attached matter. Work by Yung et.al. [43] examined the lift force on a particle due to turbulent bursts compared to the axial drag force. By measuring the angle of flight following detachment of a particle from the surface, they found that the burst force was small compared to axial drag. Their conclusion was that turbulent bursts were unlikely to detach particles within the dimensionless size range of $0.5 < d_p^+ < 1.3$ , which was the range directly examined. ( note: the + superscript refers to a variable made dimensionless by scaling with fundamental units comprised of friction velocity, fluid density and viscosity ).

Direct measurement of the lift forces on a particle sited on a surface in a turbulent boundary layer has been carried out by Hall [44]. Relatively large particles were considered in the study, but by suitable dimensionless scaling, Hall claimed that the lift forces on smaller particles could be predicted. The non-dimensional

transformations were

$$F^+ = F\sigma_f/\mu^2 \tag{2.23}$$

$$a^+ = a\sigma_f u^*/\mu \tag{2.24}$$

Measurements were carried out down to $a^+ = 1.8$. The usual limit of the viscous sub-layer is defined to be $y^+ = 5$, therefore the smallest particle occupied 72% of the sub-layer. These particles were considerably larger than those of Yung et.al. [43]. The relationship Hall obtained was

$$F^+ = 20.9\,(a^+)^{2.31} \tag{2.25}$$

The ability of the relationship to fit the data diminished with particle size, and surface roughness was noted to change the force by up to a factor of six. The force was reduced if a particle was positioned between roughness elements or increased if sited on top of a surface peak.

Since Gutman's application of turbulent bursts to crossflow filtration [41], little has been published in that area. One problem in using the approach is that it is likely to be specific to every system, in that it cannot be determined a priori whether the turbulent bursts will have enough energy to detach deposits. The magnitude of interparticle forces determines the energy of removal.

### 2.2.5. Frictional force balances

The balance of the axial drag force compared to the permeate drag force was considered by Ebner [45] to be the parameter responsible for limiting the decline of flux in crossflow filtration. It was proposed that if the ratio of axial drag to permeate drag exceeds a critical value - that of a friction coefficient - no further deposition is possible. Normal forces decrease with time due to the increasing hydrodynamic resistance of filter cake, while axial drag increases due to the diminishing channel dimension. Eventually

these forces balance and steady state filtration is established. Although this idea is similar to the scour approach, the difference is that scour models assume a reversible equilibrium of cake growth and re-entrainment; however in the force model, cake height tends to a limiting value with no assumed removal.

This frictional idea was further developed by Rautenbach and Schock [46] who proposed that a particle reaching the surface of a membrane ( or filter cake ) either sticks at the point of contact or moves tangentially along the surface, according to the force balance

$$C_D\ (\sigma_f u_{av}^2/2)\ (\Pi a^2) \geq k_f\ C_D\ (\sigma_f v_w^2/2)\ (\Pi a^2) \qquad (2.26)$$

where $C_D$ is a drag coefficient for spheres, $u_{av}$ the axial velocity averaged over the particle, $v_w$ the permeate velocity and $k_f$ is a coefficient of friction. The situation is illustrated in figure 2.3.

In the Stokes regime, the drag coefficient is given by

$$C_D = 24/Re_p \qquad (2.27)$$

Substitution of this expression into the condition of sliding ( equation 2.26 ) gives the modified equilibrium of drag forces to be

$$u_{av} \geq k_f v_w \qquad (2.28)$$

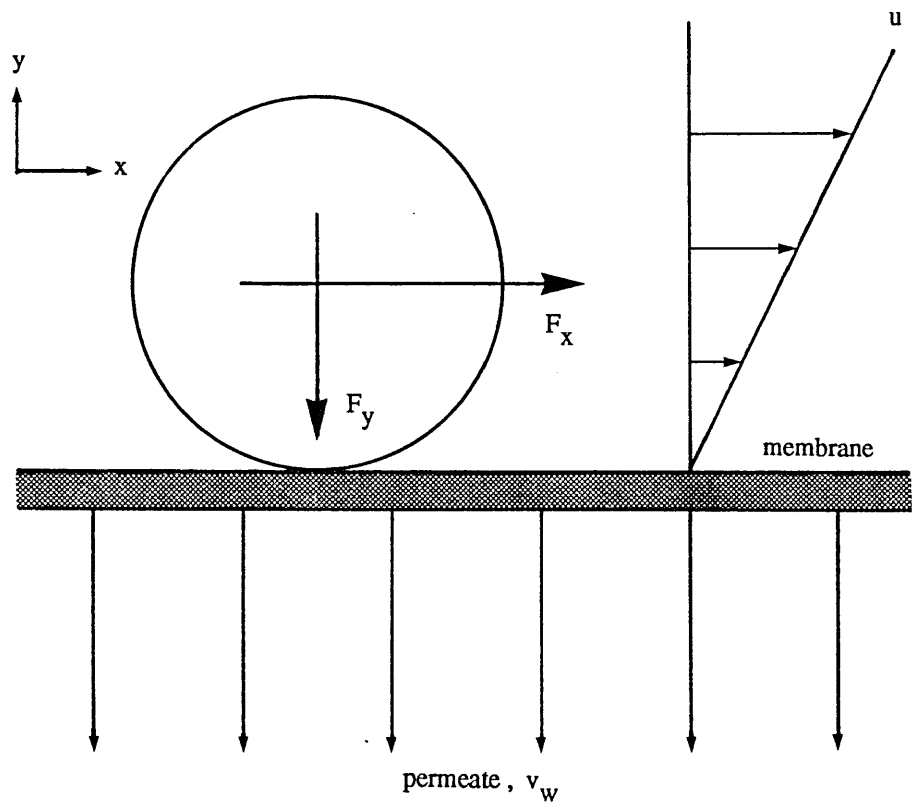
The boundary layer velocity profile gives an expression for $u_{av}$, which is incorporated into equation 2.28, producing the result that

$$v_w \sim Re^{k1}\ (\mu/\sigma_f d_f)(a/d_f)^{k2} \qquad (2.29)$$

where $d_f$ is the channel dimension and the k values are constants depending on the velocity profile assumed for the boundary layer. The right-hand side of equation 2.29 is termed the Rautenbach parameter throughout the rest of this thesis. The best fit to their data presented was obtained by using an assumed boundary layer profile for the buffer layer ( $7 \leq y^+ \leq 35$ ) of

FIGURE 2.3

FRICTIONAL FORCE BALANCE IN SIMPLE GEOMETRY



$$u^+ = 3.0\ y^{+\ 0.44} \qquad (2.30)$$

This profile is normally valid for the buffer, rather than viscous sub-layer. Using equation 2.30 in 2.28 and assuming that the friction factor varies as $Re^{-1/4}$, the exponents of equation 2.29 are $k_1 = 1.26$ and $k_2 = 0.44$. Choice of the buffer layer profile is rather surprising as the particles used were about 2 microns in size, which in most cases would be well inside a viscous sublayer. In membrane tubes of several millimetres diameter subjected to turbulent flow, the viscous sub-layer has a thickness of order $10^{-5}$m. However, Rautenbach and Schock suggested that wall suction reduces the dimensions of the boundary layer and the presence of particles destroys the laminar flow normally assumed to exist in the viscous layer.

Rautenbach and Schock plotted their data in the form of equation 2.29 and obtained a good linear fit. This is rather surprising given their rather simplified treatment of the slipping equilibrium and that the particles used were polydisperse clay or quartz suspensions comprising slab-shaped particles.

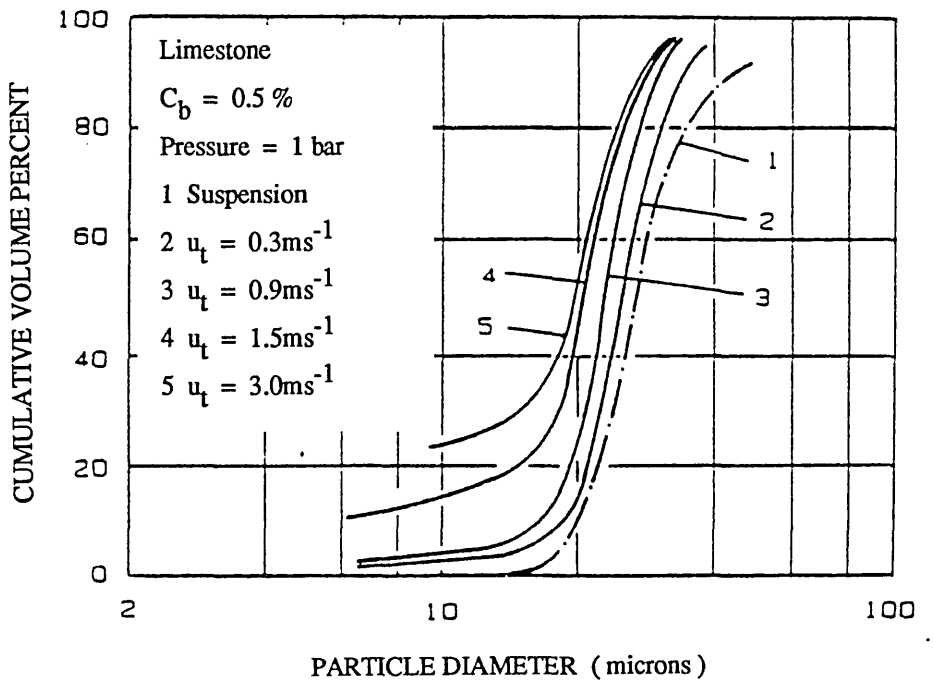
One interesting aspect of this frictional equilibrium approach has been highlighted by Fischer and Raasch [47]. The two hydrodynamic drag forces depend on particle size in different ways: the axial force scales as the radius squared, due to the linear velocity gradient; while the normal force scales as the radius. It was suggested that different crossflows should permit degrees of particle classification from the bulk suspension to the cake. Using a limestone suspension, Fischer and Raasch demonstrated this separation, which is shown in figure 2.4.

An extension of Fischer and Raasch's work has been made by Lu and Ju [48]. Rather than consider a frictional force balance, they modelled the condition for particle deposition by considering the moments of hydrodynamic forces acting on a particle at a rough surface. Expressions for the limiting conditions for deposition of each particle size in a broad distribution were presented and supported by experiments with calcium carbonate particles. Though the

FIGURE 2.4

PARTICLE CLASSIFICATION

Reproduced with permission from ref. 47



work appears to have a subtle difference of approach to other force based models by using a moment balance, it results in a similar form of expression relating permeate flux to crossflow as the theory of Rautenbach and Schock ( equation 2.29 ).

The main weakness in the frictional force models so far described in this section is that no account has been taken of interparticle forces. These forces could play an important part in the frictional equilibrium, and the following studies show their potential effect.

Consideration of the repulsive electrostatic forces between particles has been undertaken by McDonogh et.al. [49]. The diffusive mass balance of equation 2.2 was adapted in terms of a force balance, such that the convective term was replaced by viscous drag, the diffusive term by a Brownian force, and an electrical force term was added from concepts developed by Langmuir [50] and the DLVO theory of electrostatic interaction [51]. McDonogh concluded that this approach only deviates from the original form of equation 2.2 at particle sizes of less than 1 micron.

Cohen and Probstein [52] also considered double layer forces to be important. They found that when operating a reverse osmosis unit, no colloidal fouling with ferric hydroxide occured when the permeate velocity was below $5x10^{-6}m\ s^{-1}$. Wakeman and Tarleton [53] used imposed electrical fields to good effect in preventing deposition of particles on membranes. Work examining the role of electrical forces in the case of solid wall deposition has been reported by Kuo and Matijevic [54], who discovered that particles of iron oxide did not deposit on a steel surface when the electrical charge on the particle and wall were of opposite polarity.

These studies [49,52,53,54] show that interparticle forces, in addition to hydrodynamic forces, are likely to influence the behaviour of particles as they approach a membrane or cake surface in crossflow filtration. The frictional balance of forces in the

original model of Ebner [45] would be more complete if these extra effects were incorporated.

## 2.3. Summary

Early modelling of crossflow filtration stemmed from concepts of concentration polarization in reverse osmosis or ultrafiltration. It was quickly realized that the diffusive arguments for particulate back-transport were invalid. Five main approaches were adopted to model the steady state permeate fluxes obtained in crossflow filtration of particles.

(i) Convective models reject back-transport mechanisms entirely, suggesting that the normal particulate mass flux is matched by axial convection of a flowing cake layer. Physical conditions to explain the limiting flux lack generality and all analyses are based on laminar flow profiles.

(ii) Shear-induced hydrodynamic diffusion theories assume that the convective flux to the membrane is balanced by a diffusion-like process originating from the shear field. Compared to purely convective models, rather more satisfactory conditions specifying the deposition of a permanent filter cake and the process limiting flux decline are proposed. The main problems in applying SIHD to crossflow filtration are that the diffusion phenomenon has only been reported for particles in the size range of 50 microns to 0.1mm, and that no suitable analysis for a turbulent boundary layer has been proposed.

(iii) Inertial lift theories propose that the net velocity of a particle approaching the membrane is equal to the sum of permeate velocity and a lift velocity. Steady state is reached when the two velocities become equal. Strong evidence for this effect is available for cases of large particles in narrow tubes, where the fluid has a laminar flow profile. Lift forces become negligible in large channels. In principle, the effect may be valid in a turbulent boundary layer, but no studies on this application have yet been reported. Another limitation is that the analysis requires the

assumption of infinitely dilute suspensions to be valid.

(iv) Scour and turbulent burst models equate the filter cake growth arising from pressure-driven convection with a re-entrainment of filter cake. This resuspension is due to shearing action of the fluid, or turbulent bursts reaching the cake surface. Modelling is rather empirical in the case of the shear mechanism, and some doubt exists over the ability of turbulent bursts to remove particles from a surface.

(v) Frictional force models suggest that the build-up of filter cake is governed by the balance of axial and normal drag forces acting on a particle at the cake surface. Beyond a certain ratio of these forces, further deposition is fully suppressed. This approach seems physically plausible, but analyses to date have been rather limited, mostly using simplified geometries and taking no account of interparticle forces. The advantage of this form of model is that no assumptions about the fluid flow regime are needed; however, predictions of filtration flux are not possible a priori, as the friction coefficient and boundary layer velocity profile are seldom known accurately.

# CHAPTER 3

# THEORETICAL MODEL OF CAKE DEPOSITION

Extension of the frictional force model of particle deposition onto the surface of a filter cake is outlined in this chapter. The first section deals with the possible mechanisms of mass transfer to the cake, analysing several back-transport mechanisms previously reported in the literature. Both hydrodynamic and surface forces acting on a particle at the cake surface are evaluated. It is proposed that deposition only occurs if the ratio of tangential to normal force does not exceed a critical value. The second section deals with the development of a filter cake to steady state, where tangential and normal forces balance. It is proposed that only a fraction of the particles convected to the tube wall are incorporated into the cake. This fraction depends on the balance of forces acting on each particle at the cake surface.

## 3.1 Equilibrium Conditions

### 3.1.1 Mechanisms of mass transfer

In the previous chapter, the basis of mass transfer mechanisms in particulate systems were outlined. The applicability of these phenomena to crossflow filtration of micron-sized particles must be assessed in order to build a useful model of the filtration process. In crossflow filtration, it is self-evident that the mechanism of mass transport towards the membrane is forced convection. However, different mechanisms of back-transport have been applied to the process, not all of which may be important. It is these back-transport processes which are investigated in this first section.

Each of the back-transport mechanisms described in chapter 2 will be evaluated for a tubular membrane having operational parameters typical of the experimental work described in this thesis.

| | | |
|---|---|---|
| $d_f$ | inner diameter | 6mm |
| $Q_t$ | volumetric flowrate | $3dm^3min^{-1}$ |
| $\tau$ | wall shear stress | $10N\ m^{-2}$ |
| $v_w$ | permeate velocity at wall | $10^{-4}m\ s^{-1}$ |
| $d_p$ | particle diameter | 1 micron |
| $C_b$ | bulk concentration | 1% solids |
| $\sigma$ | suspension density | $1000kg\ m^{-3}$ |
| $\mu$ | suspension viscosity | $10^{-3}N\ s\ m^{-2}$ |

Some of the following expressions taken from the literature have been derived using a laminar velocity profile, however the Reynolds number given by the above conditions is 10600. This anomaly is not critical for a first approximation to judge the importance of each back-transport mechanism: all the phenomena examined are increasing functions of tube velocity, therefore their importance is slightly overestimated.

(i) Magnus effect

It can be postulated that the Magnus force acting on a particle rotating due to a shear field may give sufficient lift to overcome the permeation drag towards a membrane. Rubinow and Keller [21] developed an expression for the Magnus lift velocity of a particle in a shear field. This has the following form in cylindrical co-ordinates

$$v_l = \frac{1}{9} u_t Re (a/r_o)^4 (r/r_o) \qquad (3.1)$$

where $u_t$ and Re are the average tube velocity and Reynolds number, a is the particle radius, r is the radial position in the tube, and $r_o$ is the channel radius. When this expression is evaluated at the example conditions, the lift velocity away from the solid interface is $O(10^{-12})m\ s^{-1}$. This is negligible compared to the wall permeate velocity, therefore the Magnus effect can be neglected in particle transport.

(ii) Saffman's lift force

This expression for the lift on a particle in a shear field is

calculated by retaining inertial terms in the Navier-Stokes equations [22]. No particle rotation is assumed, though Saffman's equation has an identical form to equation 3.1, with the constant 1/9 replaced by 0.86. Consequently, the lift velocity is $O(10^{-11})$m $s^{-1}$ at the solid surface. Saffman indicated that the analysis breaks down near the wall, but the velocity is so low that further investigation is not necessary to discount the importance of this lift phenomenon.

(iii) Lateral migration due to inertial effects

Work developing the solution of the Navier-Stokes equations for a particle has continued since Saffman's study. The solid wall case has been considered in many studies [e.g.25,26,55], but over a number of years, Belfort and co-workers [27,28,29,30] have developed the mathematical treatment to apply to the porous walls of membrane filtration. The last of these papers [30] outlines the solution for the lift velocity of a particle in a channel with one porous and one solid wall. This has the the form

$$v_l = Re_p K^2 u_t f(\beta) \qquad (3.2)$$

where $Re_p$ is the particle Reynolds number based on average axial velocity, K is the ratio of particle radius to channel height, and $\beta$ is a non-dimensional position in the channel. The function $f(\beta)$ has a maximum value of 1.5 at the porous boundary. Substitution of the example conditions into equation 3.2 gives a lift velocity of $O(10^{-7})$m $s^{-1}$. Once again, this form of particle transport can be neglected in the example system.

(iv) Shear-induced hydrodynamic diffusion (S.I.D.H.)

It is rather more difficult to evaluate directly the importance of this effect. The argument of Davis and Leighton [18] is that equilibrium is reached when the convective transport to the cake surface is balanced by hydrodynamic diffusion, i.e.

$$v_w \Phi_w = D\,(d\Phi/dy)_w \qquad (3.3)$$

where $v_w$ is the permeate velocity, $\Phi_w$ is the volume fraction of solids at the wall, and D is the hydrodynamic diffusion coefficient. Development of their theory produces an expression for the maximum height of the concentration boundary layer in terms of filtration operating parameters as follows

$$y_m = 0.083\, a^2 \tau / v_w \mu_o \qquad (3.4)$$

where $\tau$ is the wall shear stress and $\mu_o$ is the permeate viscosity. The value of $y_m$ for the example system is $2 \times 10^{-6}$m, which is only two particle diameters. It must therefore be concluded that the whole basis of SIHD is invalid in this system, as a concentration boundary layer of such small scale is meaningless.

### 3.1.2 Particle force model

As an alternative to the previous approaches to describe equilibrium, where the convective flux to the cake is balanced by a back-transport mechanism, a model derived only from convection is now proposed. It is based on the balance of hydrodynamic and interparticle forces acting on a particle at the cake surface. Deposition is possible if the ratio of net tangential force to net normal force is less than the coefficient of friction for the particulate material. Figure 3.1 illustrates the forces acting on a particle resting on a planar surface, where the governing equation is

$$F_x \geq k_f F_y \qquad (3.5)$$

where $k_f$ is the coefficient of friction. However, when applied in planar geometry ( figure 3.1 ), this model cannot fully describe the forces acting on a particle at the surface of a filter cake, where the surface has roughness of the same order as particle size. All the forces acting on a particle in a more realistic geometry are dependent on the exact position of that body in relation to the other deposited particles. In addition to the hydrodynamic effects, Van der Waals and electrostatic forces contribute to $F_x$ and $F_y$ in equation 3.5.

FIGURE 3.1

FRICTIONAL FORCE BALANCE IN SIMPLE GEOMETRY

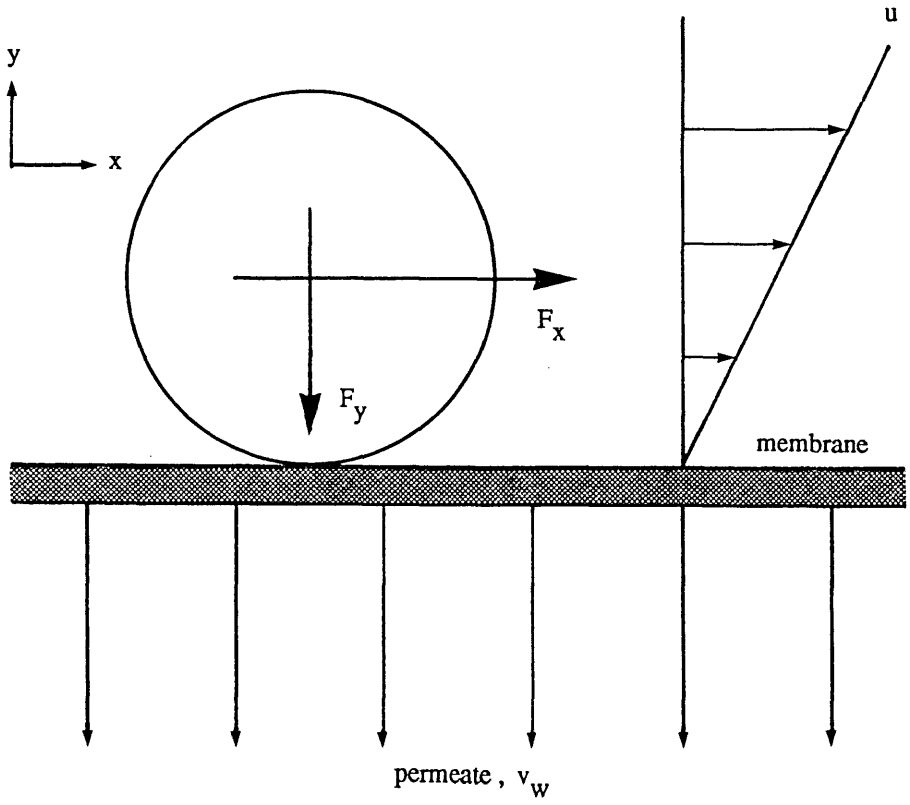
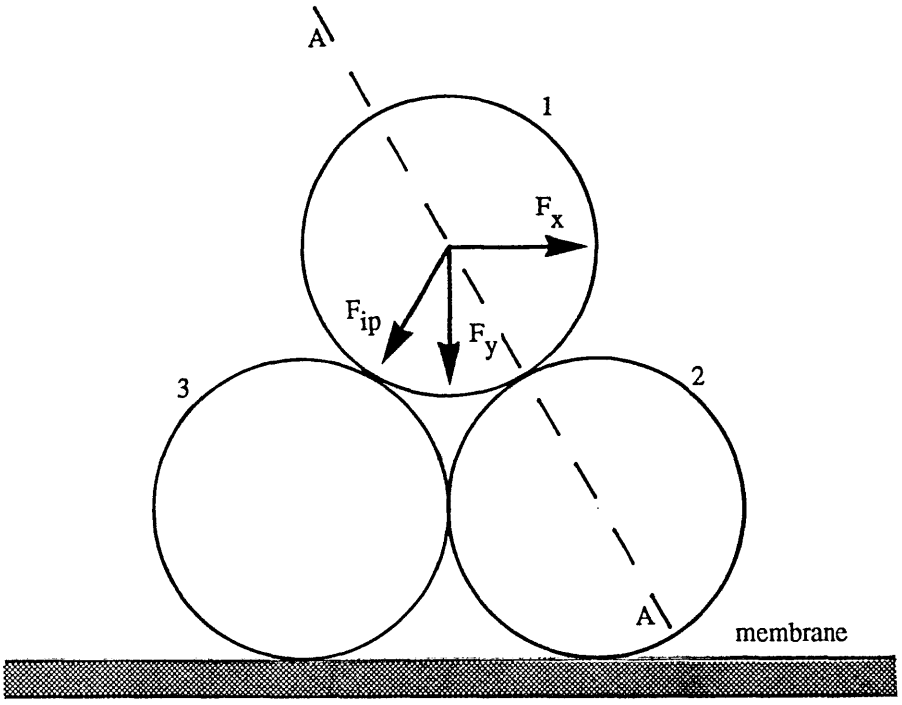


Figure 3.2 shows one possible arrangement of a particle at the surface of a filter cake and the action of these additional forces.

FIGURE 3.2

FRICTIONAL FORCE BALANCE IN COMPLEX GEOMETRY




$F_{ip}$ acts in an indeterminate direction

In order to describe the equilibrium condition in terms of operating parameters in a filtration system, each of the forces shown in figure 3.2 must be quantified. The next three sub-sections describe the basis of each force, while the fourth incorporates these forces into the expression for frictional equilibrium.

(i) Axial shear force

The force acting on a sphere resting on a plane in a uniform velocity gradient has been evaluated by O'Neill [56], with the assumption that the inertial terms in the Navier-Stokes equations are neglected:

$$F_x = 1.7\ (6\Pi\mu_o a u_{av}) \qquad (3.6)$$

where $u_{av}$ is the velocity at the mid-point of the sphere. While this expression may be applicable to a planar system, the situation shown in figure 3.2 cannot be truly represented by equation 3.6. For a sphere half-submerged in the cake, the expression for axial force must take the same form as equation 3.6, but the pre-multiplier will have a value of rather less than 1.7. Additionally, the presence of other particles near the cake surface will collide with the particle under consideration and disturb the velocity field from the assumed linear profile.

In the development of this frictional model, it is assumed that the axial force is given by an expression of the same form as equation 3.6, but that the pre-multiplier has a smaller value. Using the example values of section 3.1.1, equation 3.6 produces an axial force of $8x10^{-11}$N.

(ii) Normal force

A starting point to evaluate the normal force acting on a particle at the cake surface is Stokes equation, which could be expressed

$$F_y = 6\Pi\mu_o a v_w \qquad (3.7)$$

where $v_w$ is the permeate velocity at the wall. As with the axial force equation, the conditions of filtration violate the assumptions of its derivation. The author is not aware of any analysis evaluating the normal force acting on a half-submerged sphere, but several studies have been carried out to determine the force on a sphere in a

packed bed. These works indicate the deviation from Stokes law as particle crowding increases. The simplest approach is based on the Carmen-Kozeny equation, dividing the total force per unit area on a bed by the number of particles thus obtaining the average drag per particle. This gives a multiplier to the Stokes equation of

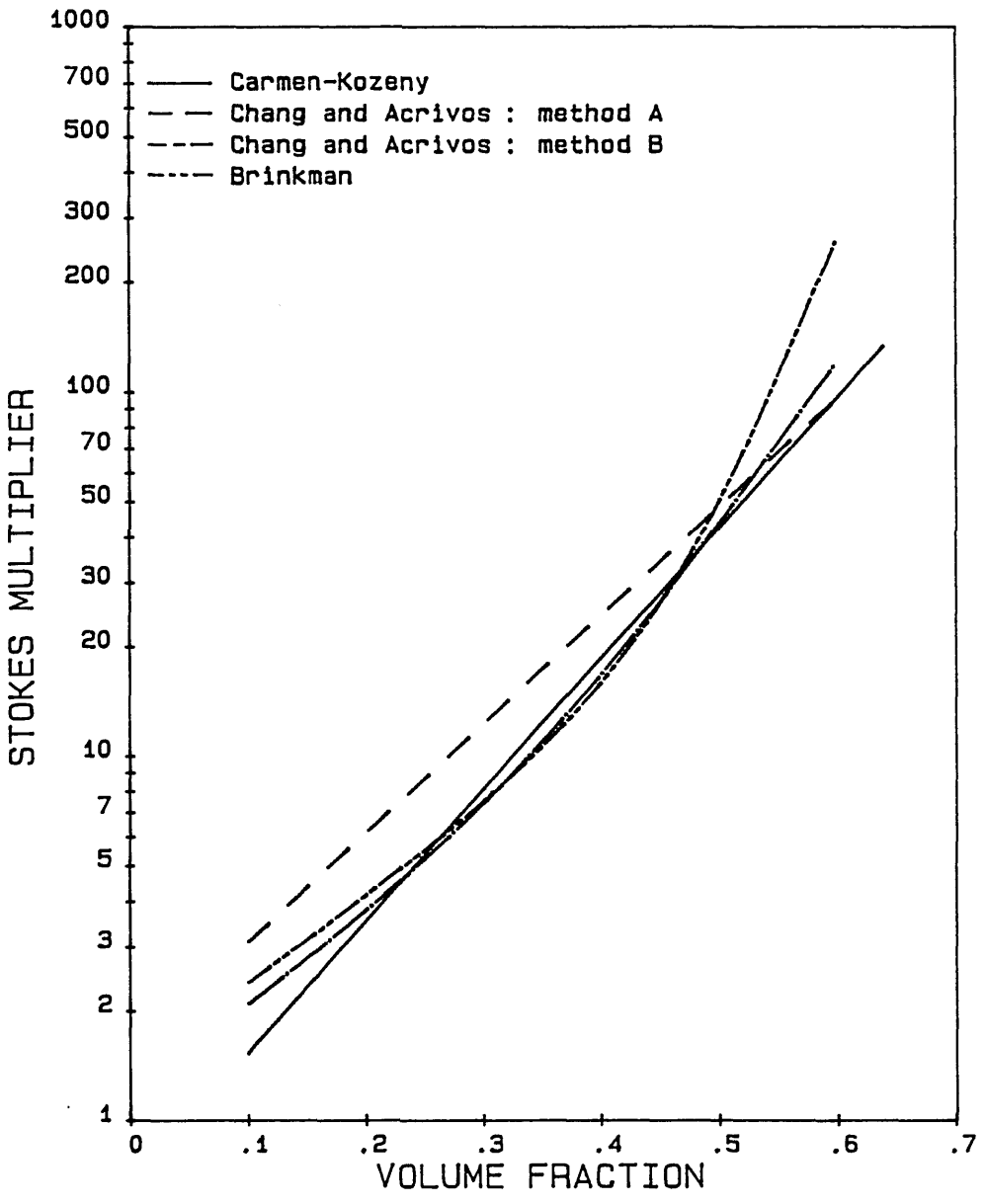
$$F_y = \frac{10\,\Phi}{(1-\Phi)^3}\,F_{ST} \qquad (3.8)$$

where $F_{ST}$ is the right-hand side of equation 3.7. Chang and Acrivos [57] compare this method with two techniques of their own and a theory by Brinkman [58]. The results of these studies are shown in figure 3.3 which plots the Stokes multiplier against volume fraction. As can be seen none of these methods produces a radically different result from the Carmen-Kozeny approach.

In this study, the assumptions made about the magnitude of the normal force for a half-submerged particle are that the form of the Stokes equation applies and its magnitude is bounded by a multiplier of 137 ( $\Phi = 0.64$ ) using the Carmen-Kozeny approach. This volume fraction is the value for random packing of spheres, first suggested by Scott [59]. Therefore, normal force on a particle subject to the example conditions of section 3.1.1 is less than $10^{-10}$N.

FIGURE 3.3

FORCES ON A PARTICLE IN A PACKED BED



(iii) Van der Waals and electrostatic forces

These two forces begin to apply to particulate systems when the separation distance between particles becomes very small. Typically, electrical effects operate at a range of less than $10^{-7}$m, while Van der Waals (VdW) forces begin to be important at $10^{-8}$m. Both forces will therefore be influential in considerations of particle attachment to a filter cake. Born repulsion, which has its origin in the overlap of electron clouds, is only important at distances of less than $5x10^{-10}$m and is not considered here.

Van der Waals force

Schenkel and Kitchener [60] recommended equations for the VdW potential between two equal sized spheres, which upon differentiation give the following expressions for attractive force

for $s > 9.1x10^{-9}$m

$$F_a = -A_{131}\, a \left[\frac{1.30x10^{-9}}{s^3} - \frac{9.15x10^{-18}}{s^4} + \frac{2.26x10^{-26}}{s^5}\right] \qquad (3.9)$$

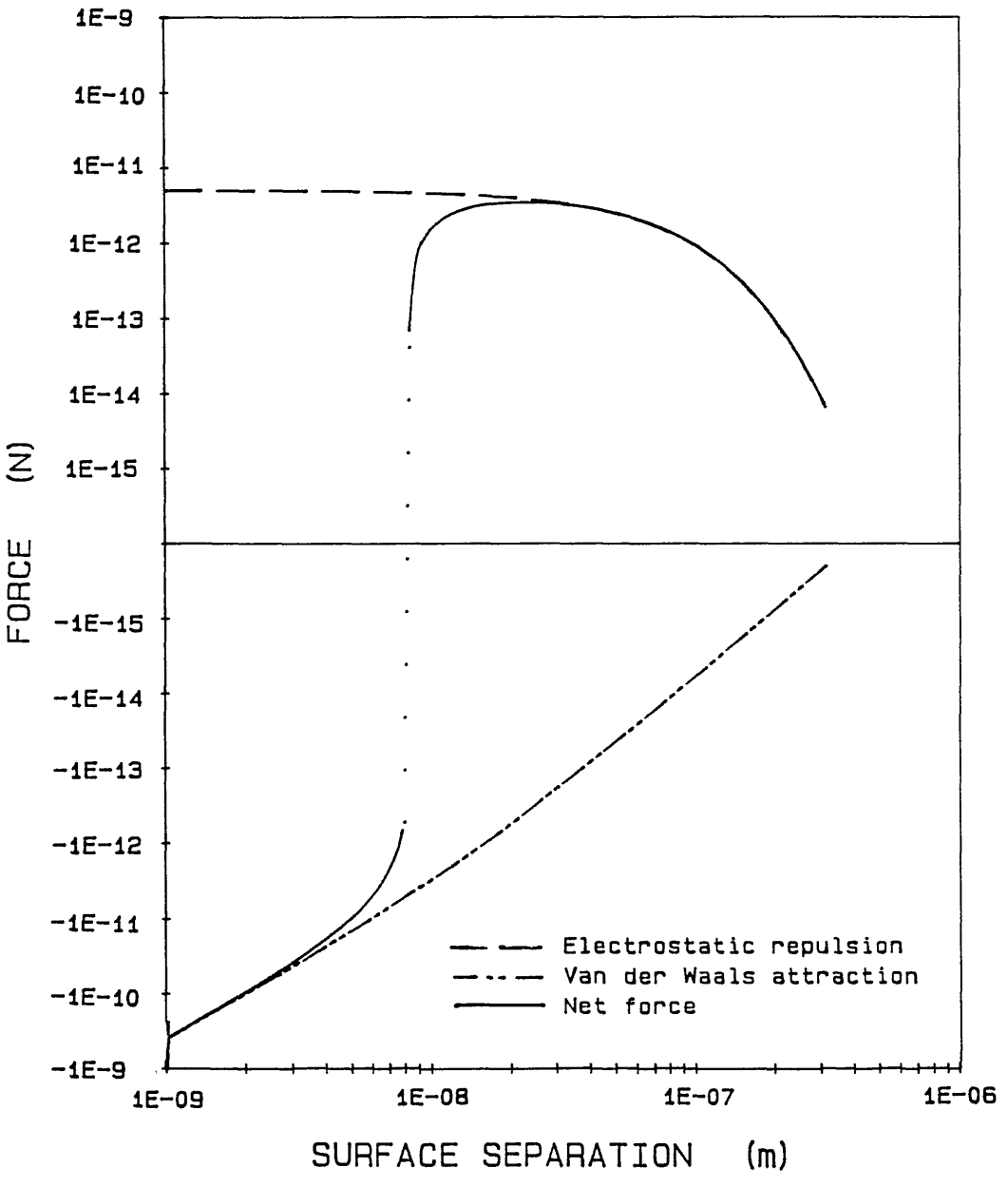
for $s \leq 9.1x10^{-9}$m

$$F_a = -\frac{A_{131}\, a}{12}\left[\frac{(1 + 2.22x10^{8}\, s)}{s^2 (1 + 1.11x10^{8}\, s)^2}\right] \qquad (3.10)$$

where $A_{131}$ is the Hamaker constant and s is the separation distance between particle surfaces. The two equations are necessary to account for retardation effects at larger separations. Prieve and Russel [61] found the Hamaker constant for the polystyrene - water - polystyrene system to be $1.37x10^{-20}$J, while Israelachvili [62] suggested that the value may lie between $0.95x10^{-20}$ and $1.4x10^{-20}$J. For a particle diameter of 1 micron and a Hamaker constant of $10^{-20}$J the attractive VdW force is plotted in figure 3.4.

FIGURE 3.4

INTERPARTICLE FORCES



Electrostatic force

Surface charge on colloidal particles gives rise to a repulsive potential, which upon differentiation has the following form for repulsive force [63]

$$F_r = \frac{\Sigma \Sigma_0 V_z^2 a K_D \exp(-K_D s)}{2(1 + \exp(-K_D s))} \qquad (3.11)$$

where $1 / K_D$ is the Debye length, given by

$$K_D = \left[ \frac{2 e^2 z^2 N_{av} C}{\Sigma \Sigma_0 k_B T} \right]^{1/2} \qquad (3.12)$$

$V_z$ is the surface ( or zeta ) potential and C is the ionic strength of the suspending fluid ( for other symbols see the nomenclature ). For a zeta potential of 50mV and ionic concentration of 0.05M ( a typical buffer concentration ), the plot of repulsive force as a function of separation distance is shown on figure 3.4, together with the summation of Van der Waals and electrostatic forces.

(iv) Model development

An order of magnitude estimate of particle separation distance between two latex spheres in a filter cake can be made from some knowledge of latex structure. Long polymer chains form outwards from the surface of a sphere limiting the approach of two particles. Atomic distances are between $10^{-10}$ and $10^{-9}$m, therefore it might be estimated that the closest separation distance between two latex spheres is of order $10^{-8}$m. Figure 3.4 shows that the net interparticle force does not drop below $10^{-12}$N at separations less than $10^{-7}$m ( except for the transition from attraction to repulsion ). At $10^{-8}$m, the net interparticle force is of similar magnitude to the hydrodynamic forces.

To express the condition of slip for a particle in the position illustrated by figure 3.2, a force balance using equation 3.5 is taken, where all forces are resolved into their components parallel and normal to plane AA. Upon re-arrangement, the form of the slip equilibrium in the direction perpendicular to AA is

$$F_y = k_1 F_x + k_2 F_{ip} \qquad (3.13)$$

where $F_{ip}$ is a vector resolved in the direction perpendicular to AA, representing the net effect of interparticle forces; and the k coefficients are constants depending on fluid viscosity, system geometry and friction coefficient. The resultant interparticle force vector is shown in figure 3.2 acting along the line of centres of spheres 1 and 3; however this is an arbitrarily chosen direction as other particles just above the cake surface, together with adjacent spheres in the cake, will influence its direction and magnitude.

In order to obtain the force balance in terms of filtration operating conditions, the expressions for all forces must be simplified. If a linear velocity profile near the cake surface is assumed, equation 3.6 can be expressed

$$F_x \sim a^2 \tau \qquad (3.14)$$

The equation for the normal force on a sphere ( 3.8 ) can be reduced to

$$F_y \sim a v_w \qquad (3.15)$$

and for a fixed value of separation distance between particles, the interparticle force equations (3.9 and 3.11 ) simplify to

$$F_{ip} \sim a \qquad (3.16)$$

Substitution of these force expressions into equation 3.13 gives the criterion for steady state filtration as

$$v_w = k_1 a \tau + k_0 \qquad (3.17)$$

This model has several limitations which must be explained. Firstly, there are assumptions concerning the hydrodynamic forces acting on a particle at the surface: only viscous drag forces are considered in the viscous sub-layer and a linear velocity profile close to the wall is assumed, despite the presence of porous walls

and particulate matter. Dodds [64] discovered turbulent eddies penetrating the viscous sub-layer to a distance of $y^+ = 2$, but the effect of these has been neglected in the force equations. A second difficulty is that the coefficients in equation 3.17 are complex functions of the geometry of particle contact, friction coefficient and magnitude of hydrodynamic and interparticle forces; therefore their values cannot be predicted a priori. Even if these coefficients could be evaluated exactly for every possible particle approach to the filter cake, they would have to be averaged over all configurations. Despite these arguments, the advantage of the model is that due to its simple mathematical form, the constants in equation 3.17 can be determined from a small number of tests. Once evaluated, performance predictions for filtration at all other operating conditions can be made.

## 3.2 Dynamic Performance

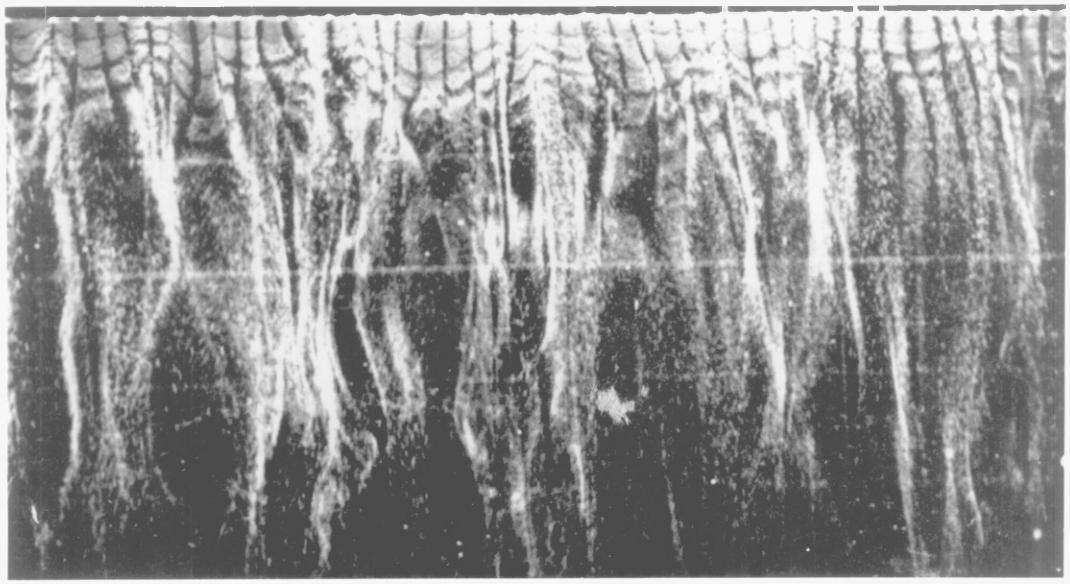
In section 3.1.1, explicit mechanisms of back-transport were shown to be of limited importance in tubular crossflow filtration. Therefore, the only phenomenon reponsible for the net mass transfer of particles is convection. In a well-mixed filtration system, the mass flux towards the filter cake is given by the product of permeate flowrate and bulk concentration. This well-mixed assumption is supported by plates 3.1 and 3.2, which show turbulent flow patterns in a boundary layer. Turbulence is observed well inside the viscous sub-layer at $y^+ = 2.7$. The system photgraphed did not have the added complications of wall suction ( which reduces the thickness of the boundary layer [65] ) or particulate matter ( which disrupts the viscous sub-layer ).

PLATE 3.1

VELOCITY STREAMLINES AND TIMELINES IN A BOUNDARY LAYER

Reprinted with permission from ref. 36

$y^+ = 2.7$



$y^+ = 4.5$

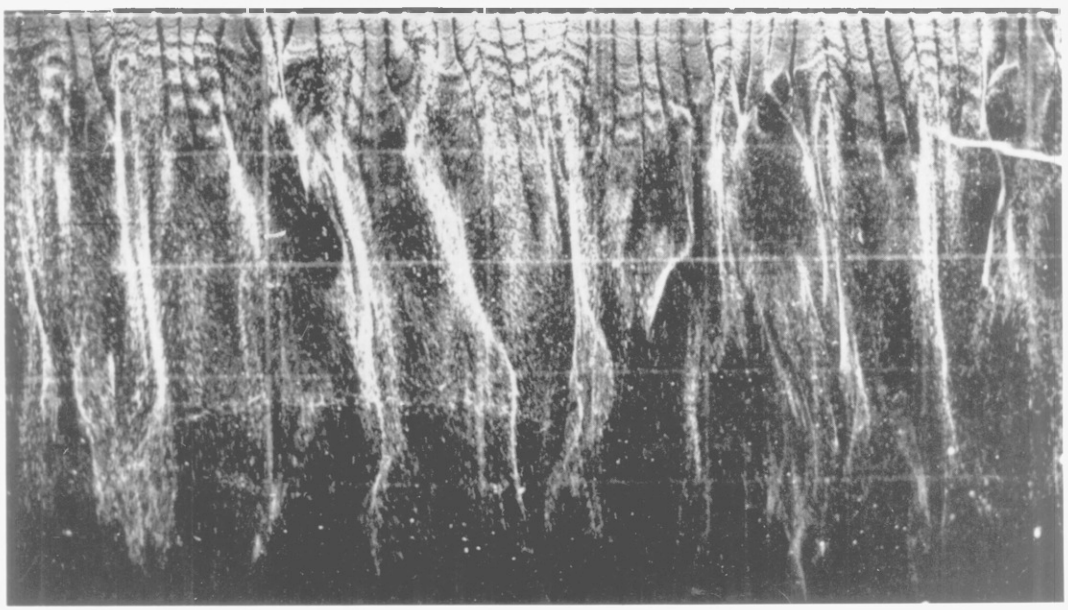
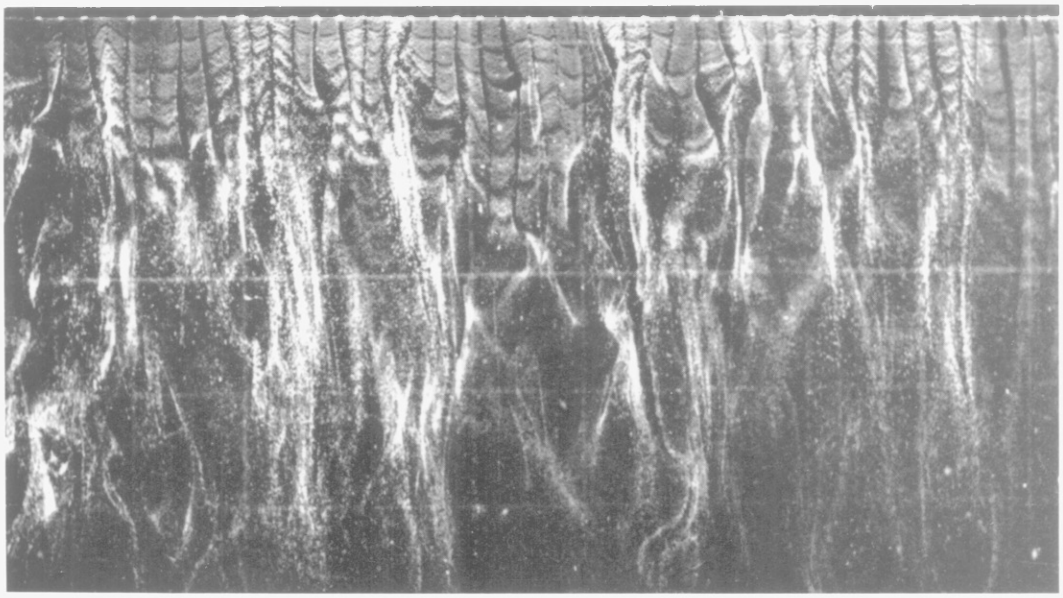


PLATE 3.2

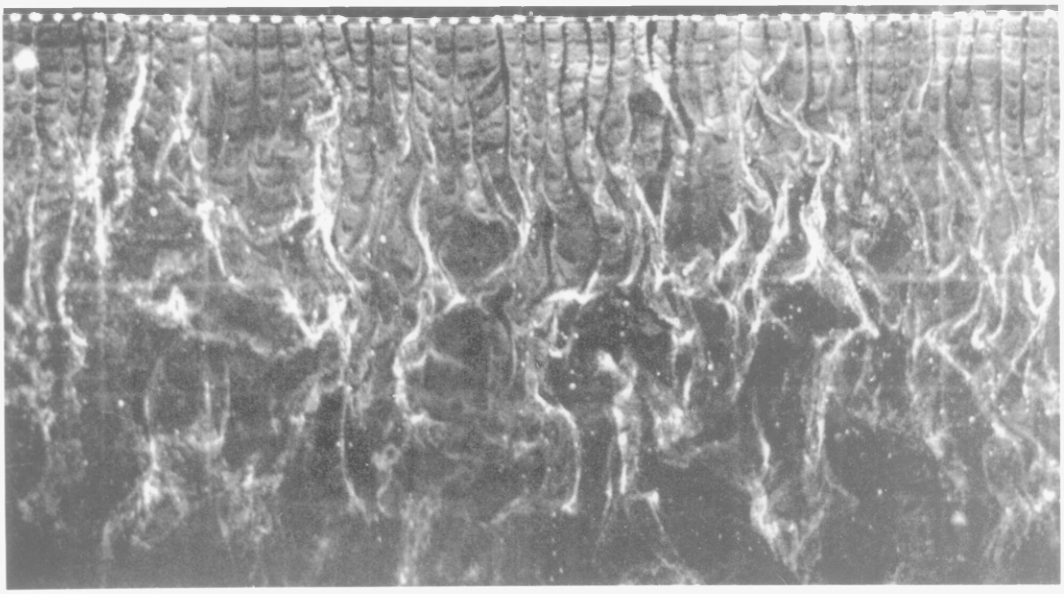
VELOCITY STREAMLINES AND TIMELINES IN A BOUNDARY LAYER

Reprinted with permission from ref. 36

$y^+ = 9.6$



$y^+ = 38$



In filtration tests, it is clear that the rate of cake growth is not equal to the mass rate approaching the membrane, for after a certain period cake growth rate declines to zero while convection continues. In the light of the frictional model for equilibrium, it is now proposed that cake growth rate continues to fall below the convective flux because conditions for particulate sticking to the cake surface become less favourable: the axial shear force increases, while the permeate drag force decreases. The cake growth rate may then be expressed

$$\frac{dm}{dt} = \alpha Q_p C_b \qquad (3.18)$$

where $Q_p$ is the permeate volumetric flowrate through a known membrane length, $C_b$ is the bulk solid concentration and $\alpha$ is a sticking factor which is defined as the fraction of convected matter incorporated into the cake. It is proposed that the sticking factor is a function of the forces acting on a particle at the solid surface. For a particular approach path of one particle to the cake, $\alpha$ must be either 0 or 1, though intermediate values arise when the entire cake surface is considered, due to its variety of favourable and unfavourable sticking positions.

A model for the approach of a filtration process to equilibrium expressed in terms of cake mass is not very useful, because cake mass as a function of time cannot usually be measured directly. The following analysis, in cylindrical geometry, transforms the basis of the dynamic model from cake mass to permeate flowrate. Variation of the sticking factor can then be calculated from the decline of permeate flowrate.

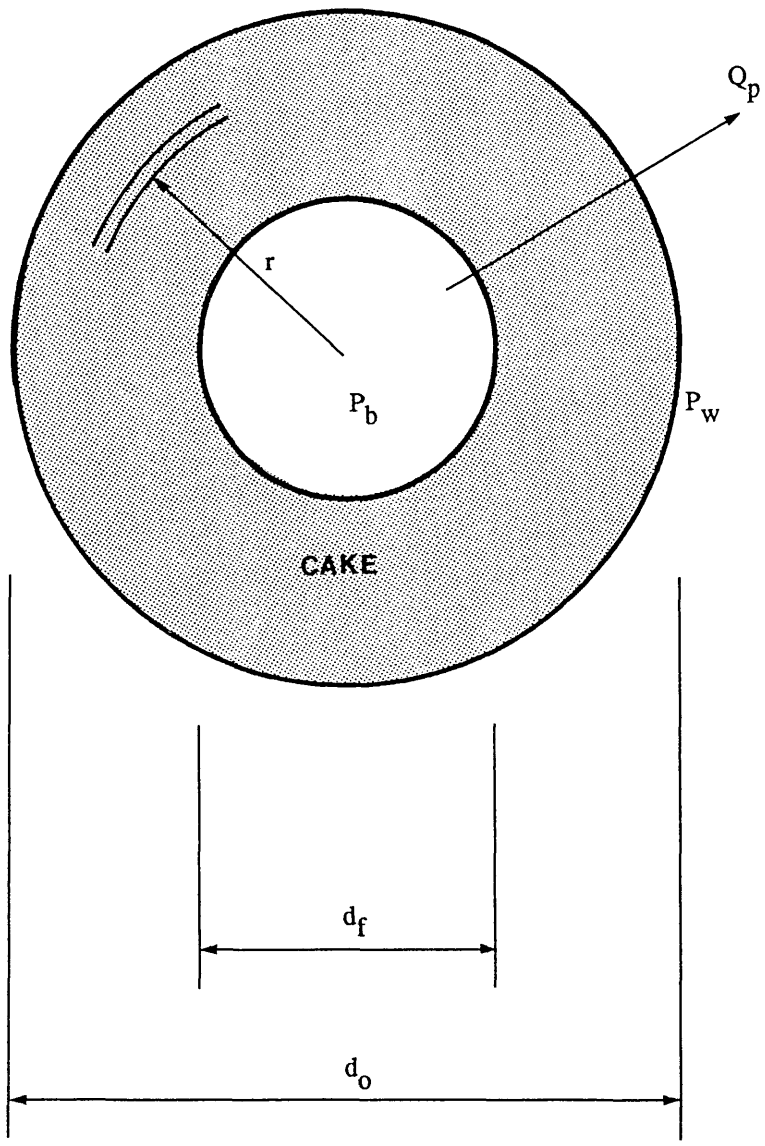
Figure 3.5 illustrates a cross-section of membrane tube and defines the dimension symbols. For a certain length of membrane ( L ) the cake mass is given by

$$m = \frac{\Pi}{4} \sigma_p (1-e)(d_o^2 - d_f^2) L \qquad (3.19)$$

where $\sigma_p$ is the particle density and e the cake voidage. The permeate flowrate through the membrane is expressed by

FIGURE 3.5

CROSS-SECTION OF A MEMBRANE TUBE



$$Q_p = \frac{\Pi d_o L(P_w - P_p)}{\mu_o R_m} \qquad (3.20)$$

where $P_w$ is the pressure at the membrane wall and $R_m$ is the hydraulic resistance of the membrane. Flow through the cake is represented by Darcy's porous media equation, which for this geometry can be integrated between the limits of the suspension/cake interface and the membrane wall thus

$$P_b - P_w = \frac{Q_p \mu_o r_c}{2\Pi L} \ln(d_o/d_f) \qquad (3.21)$$

where $r_c$ is the specific hydraulic resistance of the cake, which can either be measured or estimated from the Carmen-Kozeny equation. Eliminating $d_f$ and $P_w$ from equations 3.19, 3.20 and 3.21 allows the cake mass to be expressed in terms of permeate flowrate, cake properties and operating parameters

$$m = \sigma_p(1-e)\frac{\Pi}{4} d_o^2 L \left\{1 - \exp\left[\frac{4}{r_c}\left\{\frac{R_m}{d_o} - \frac{\Pi L P_b}{Q_p \mu_o}\right\}\right]\right\} \qquad (3.22)$$

This equation can now be coupled with equation 3.18, thus expressing cake growth rate in terms of permeate flowrate. The assumptions are that the values of specific resistance and voidage are constant throughout the cake. A more restrictive condition is that particles do not completely block large numbers of pores, so that the effective membrane resistance remains unchanged. This is rather difficult to ensure in practice, except for cases when the particle diameter is much larger than the nominal pore size. In that situation, the contact area between the membrane and particle is small compared to the membrane area covered by a particle.

In summary, the concept of a frictional force equilibrium has been applied to filtration systems not at steady state. It is suggested that the average value of particle sticking factor varies with the ratio of forces acting on a particle at the surface of a filter cake. The variation in sticking factor can be estimated from the decline of permeate flowrate.

# CHAPTER 4

# EXPERIMENTAL

In this chapter, all details concerning the experimental equipment and tests are presented. Section 4.1 outlines the strategy used to satisfy the aims of the project, while the following three sections describe the membranes, experimental rig, and particulate suspensions used. Section 4.5 presents the operational details of an experiment and also the necessary steps to convert raw data into parameters used for evaluation. The uncertainties in experimental technique are also discussed. Finally, section 4.6 lists the variables which were investigated.

## 4.1 Experimental Requirements

To investigate the validity of the friction force approach to cake growth in crossflow filtration the main requirements were to operate at a wide range of crossflows and pressures using different membranes. As one of the important variables, shear stress, is a derived parameter, it was essential that flow and pressure measurements were made accurately. Previous works on friction models have used non-ideal test suspensions such as clay or silica; it was therefore important that spherical, monodisperse suspensions with well-defined properties were used in this study. In this way, greater confidence can be given to the results of this work compared to previous studies.

## 4.2 Membranes

Three types of tubular ceramic membranes were used. Their characteristics and dimensions are listed in the table overleaf. Plate 4.1 shows the top surface and cross-section of the Ceraver 0.2 micron membrane.

TABLE 4.1

COMPARISON OF MEMBRANE CHARACTERISTICS

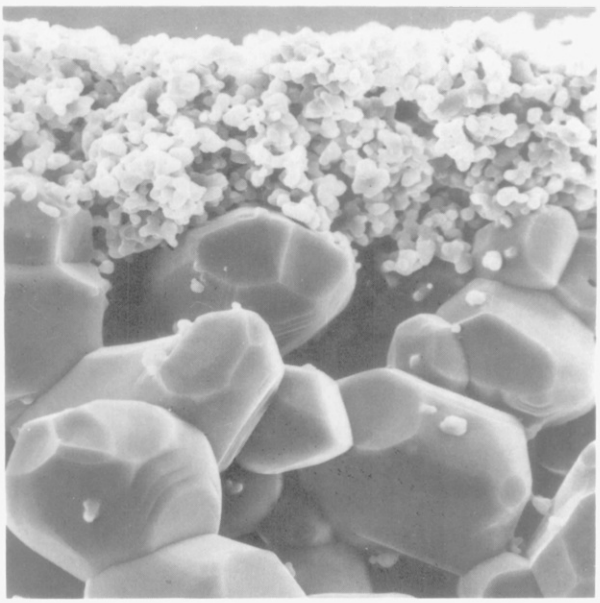
| | Membrane Type | | |
|---|---|---|---|
| | Carbosep M4 | Ceraver 0.1µm | Ceraver 0.2µm |
| Material | Zirconia on carbon | Gamma alumina on alpha alumina | Alpha alumina |
| Configuration | Single tube | Single tube | Single tube |
| Pore size | 20 000 Daltons | 0.1µm | 0.2µm |
| Outer diameter | 10mm | 10mm | 10mm |
| Nominal inner diameter | 6mm | 7mm | 7mm |
| Actual inner diameter | ~6.0mm | ~6.7mm | ~6.7mm |
| Length used | 0.535m | 0.75m | 0.75m |
| Typical hydraulic resistance | $4x10^{12}m^{-1}$ | $2x10^{11}m^{-1}$ | $10^{11}m^{-1}$ |

PLATE 4.1

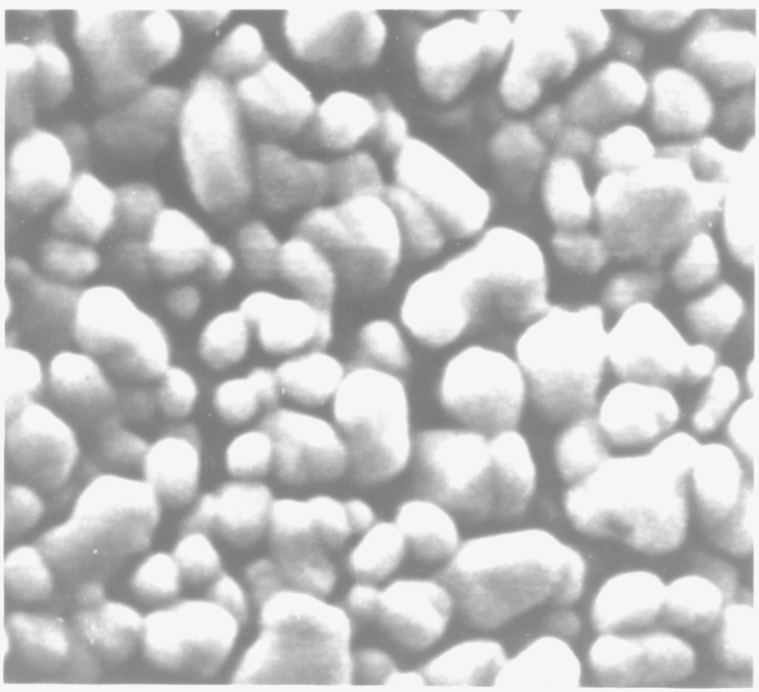
ELECTRON MICROGRAPH OF CERAVER 0.2 micron MEMBRANE

Reprinted with permission from Societe des Ceramiques Techniques

Cross-section Scale 1cm ≈ 50μm



Surface view 2μm



## 4.3 Experimental Rig

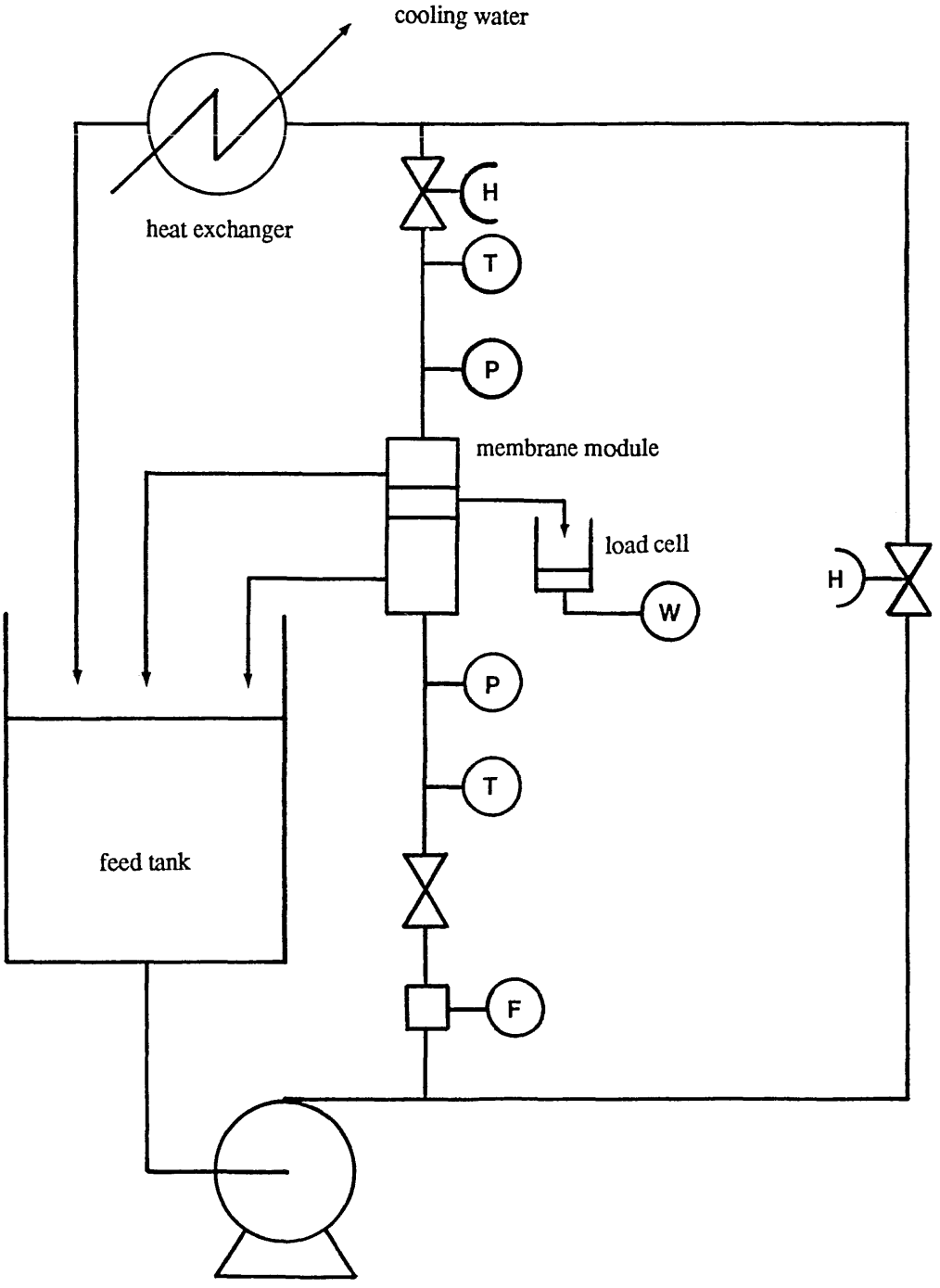
A flowsheet of the experimental apparatus used is shown in figure 4.1.

Feed suspension was recirculated through the vertically-mounted membrane test section using a centrifugal pump. Volumetric flowrate of the suspension was measured by a magnetic flowmeter placed before the test section, while a load cell recorded the permeate flowrate from one section of the membrane. When the permeate collection vessel became full, the contents were returned to the feed tank. A negligible change in feed concentration occurred during permeate collection because the ratio of permeate volume to rig holdup was less than 2% . Temperature and pressure measurements, using type T thermocouples and pressure transducers, were recorded before and after the test section. The main operating variables of test section flowrate and pressure were controlled by a combination of valves on the bypass loop and test section exit, together with a frequency controller on the pump. Rig temperature was kept constant by a variable flow of process cooling water through the shell side of the heat exchanger. A full description of all rig components is given in appendix A.

During a run the parameters described above were sequentially logged via an analogue to digital converter to a microcomputer, which recorded the data to a disk file. The output of each instrument was logged several times over the course of a chosen time cycle. For all instruments except the load cell, these readings were then averaged and the mean value was written to disk. Measurement of permeate flowrate was performed by fitting a linear regression line to the load cell output - time readings obtained over the logging cycle. The slope of this line was the permeate flowrate. This regression method was considerably more accurate than taking a difference in permeate mass over the logging cycle. A listing of the logging program is given in appendix B.

FIGURE 4.1

RIG FLOW DIAGRAM



Suitable design of the membrane housing was an important feature of the rig. Schematic details of the construction are shown in figure 4.2. Measurement of permeate flowrate was not taken from the whole membrane length, as the first section of tube enabled the axial flow to become fully developed. Permeate from this section was returned directly to the feed tank. The length of tube from which permeate flow measurements were taken was different for Carbosep and Ceraver membranes. This was due to the large differences in their hydraulic resistance, which meant that the permeate collection vessel filled at different rates. To obtain accurate permeate flow measurements the collection vessel should not fill too quickly or too slowly.

## 4.4 Feed Suspension

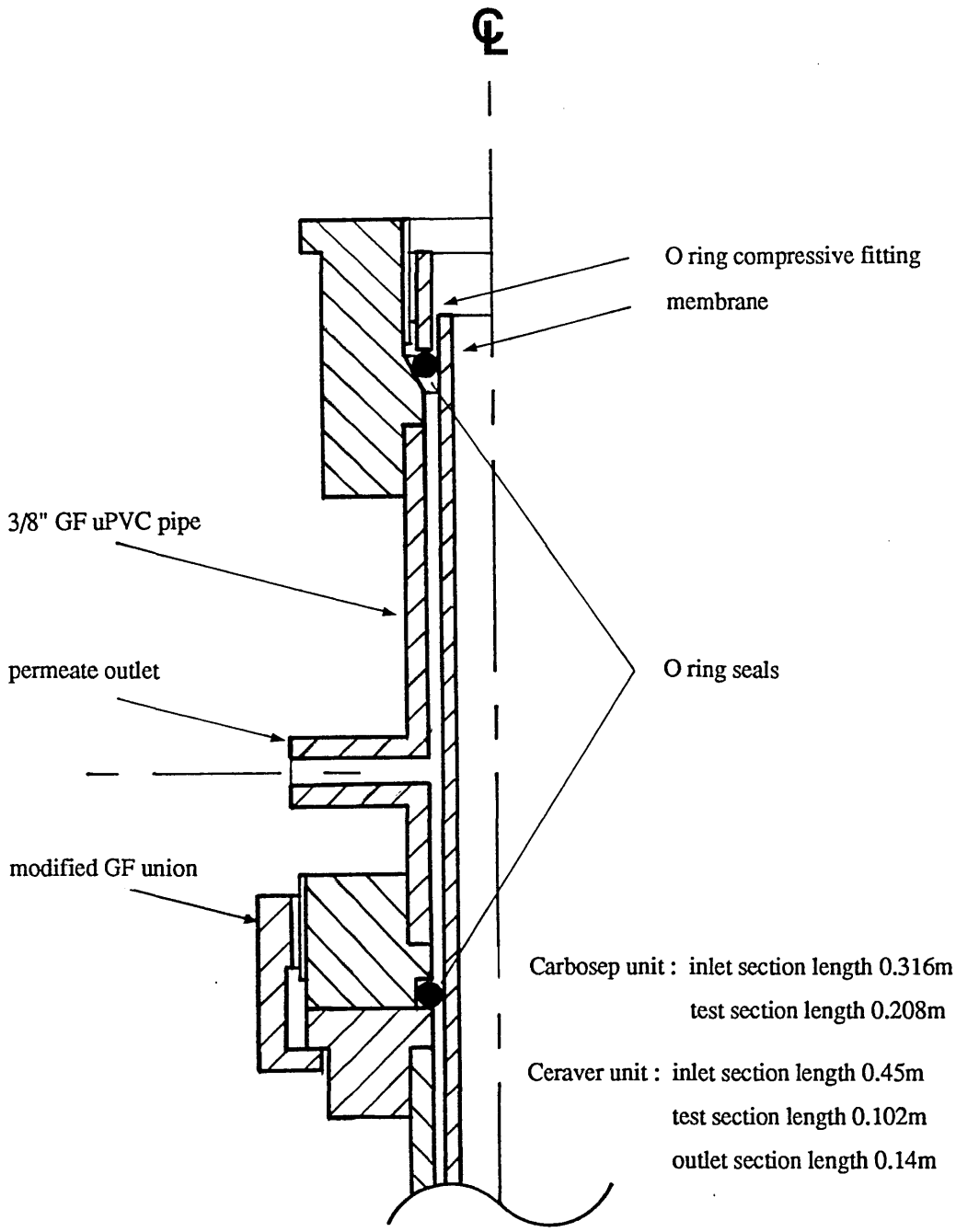
### 4.4.1 Manufacture

Polystyrene latex particles of either 0.55 or 1.8 microns in diameter were suspended in demineralized, ultrafiltered water at a concentration of 0.5wt% . The water was prepared from the laboratory demineralized pipeline in two stages: firstly using a 0.1 micron Millipore microfilter, then a Sartorius Pyrogen Removal Filter, which removed species down to 10 000 Daltons. The feed suspension also contained 0.05% biocide ( BDH Phylatol ) to inhibit bacterial, yeast and fungal growths. Suspension pH was maintained by addition of buffer mixtures. Two pH values were used in experiments: pH 7.0 was obtained by adding BDH AnalaR sodium hydroxide and potassium dihydrogen phosphate to concentrations of 0.029M and 0.050M, while pH 4.0 required BDH AnalaR potassium hydrogen phthalate at 0.050M.

The monodisperse polystyrene latices were made by the following emulsion polymerization method, fully described by Goodwin et. al. [66]. BDH General Purpose Reagent grade styrene was distilled under vacuum at 40$^{o}$C to remove inhibitor, polymer and peroxides. 500 cm$^{3}$ of this styrene, 4.4dm$^{3}$ of water and 4.10g BDH AnalaR sodium chloride were put in a 5dm$^{3}$ three-necked round-bottomed flask. The flask was placed in a water bath at a preset temperature: 70$^{o}$C for 1.8 micron

FIGURE 4.2

DETAIL OF MEMBRANE HOUSING



or 90°C for 0.55 micron particles. The contents of the flask were stirred through the central neck, while a condenser and a nitrogen purge were connected to the other necks. When the contents of the flask had reached the set temperature, 100cm$^3$ of water containing 3.73g BDH AnalaR potassium persulphate was added to initiate the polymerization. After 24 hours, the latex was removed from the flask and filtered through glass wool. 0.5cm$^3$ of Phylatol was added, and the latex was then dialyzed in boiled Visking tubing against several changes of demineralized water. Dialysis was continued until the electrical conductivity of the latex had fallen below 30μS cm$^{-1}$. Another 0.5cm$^3$ of Phylatol was then added, and the latex was stored in polypropylene containers until required. The concentration of latex in this form was about 8wt% .

### 4.4.2 Physical properties

#### (i) Particle diameter

Two methods were used to estimate the particle diameter. Scanning electron micrographs of air-dried latices suggested particle diameters of 1.8 and 0.55 microns for the suspensions made at 70 and 90°C respectively. A very narrow size distribution is indicated. The micrographs are shown in plate 4.2.

A Malvern Mastersizer indicated Sauter mean diameters of 1.48 and 0.44 microns for the two latices. Volume distributions are shown in figure 4.3. Comparison with the electron micrographs suggests that the small fraction of particles seen by the Mastersizer between 0.7 and 1.2 microns is spurious.

#### (ii) Particle density

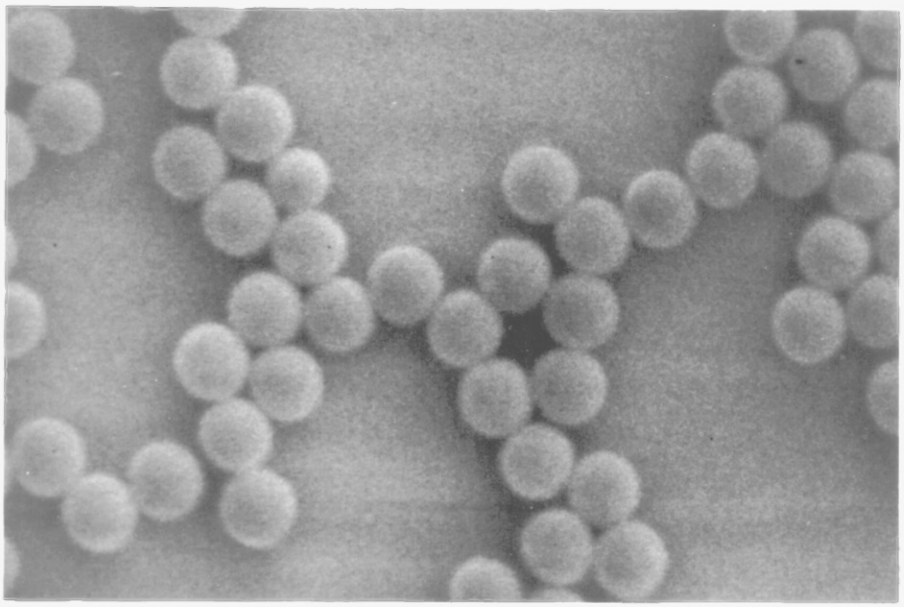
The particle density in water was estimated by weighing exactly 50cm$^3$ of stock latex suspension. A knowledge of the density of water, ambient temperature and latex concentration enables calculation of the particle density. For both the large and small particles, the value obtained was 1060 ±20kg m$^{-3}$.

PLATE 4.2

ELECTRON MICROGRAPHS OF LATEX PARTICLES

Small particles

2μm



Large particles

2μm

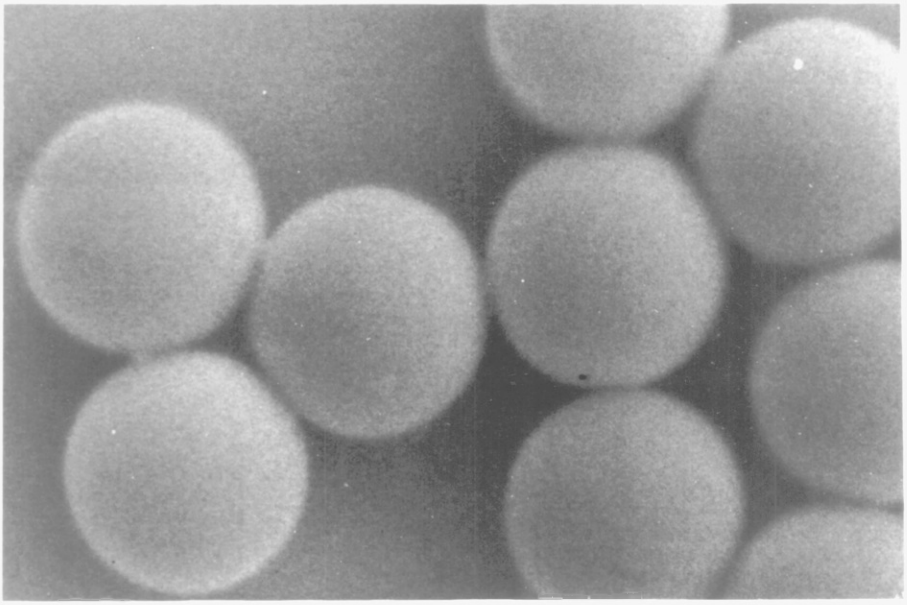
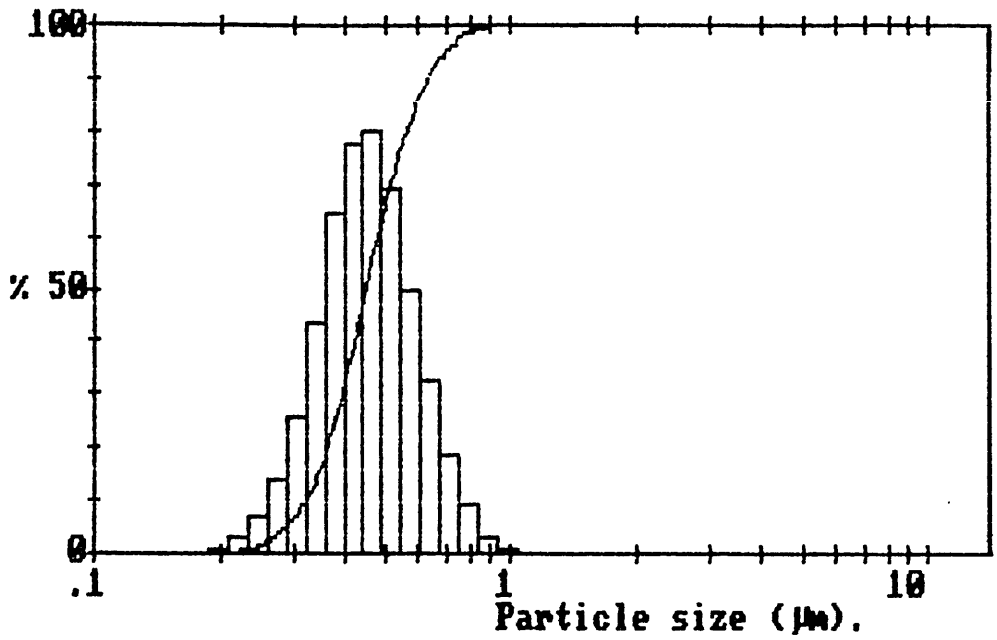


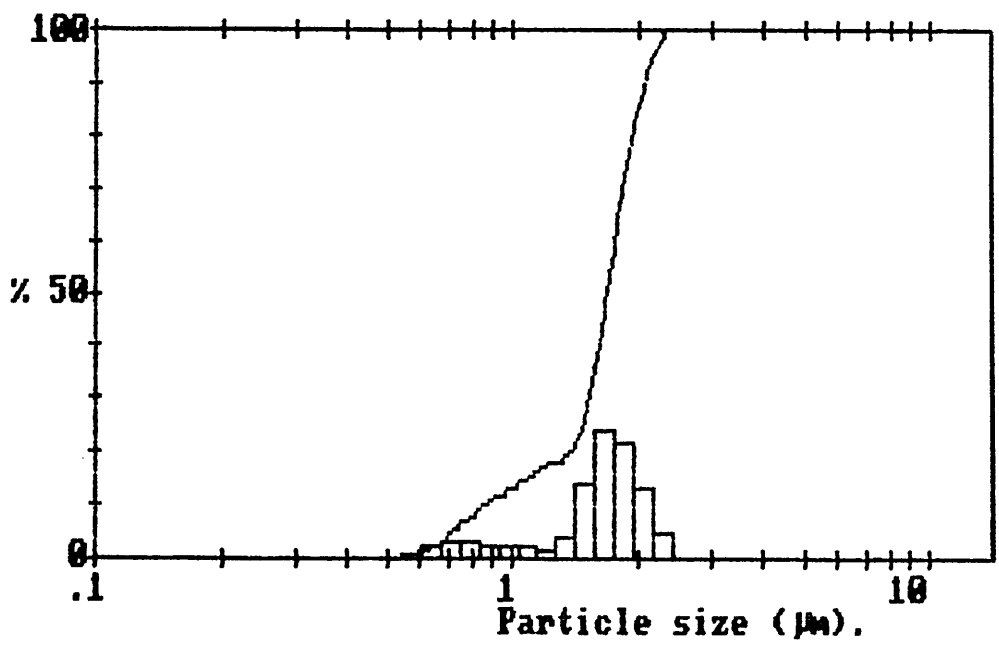
FIGURE 4.3

MASTERSIZER PARTICLE DIAMETER DISTRIBUTIONS

Small particles




Large particles



(iii) Suspension viscosity

Measurements of suspension viscosity at 25°C as a function of latex concentration were made using a Contraves Rheometer. The highest concentration measured was 58wt% solids. At all concentrations the suspensions were Newtonian. A plot of relative suspension viscosity ( to water ) against concentration is shown in figure 4.4 . Krieger [67] developed the following equation to express relative viscosity for suspensions of spheres

$$\mu_r = (1 - k_{cr}\Phi)^{-[\mu]/k_{cr}} \qquad (4.1)$$

where $\mu_r$ is the relative viscosity, $[\mu]$ is the intrinsic viscosity ( 2.5 for non-interacting spheres ), $\Phi$ is the volume fraction of particles, and $k_{cr}$ is a crowding factor ( the inverse of the maximum volume fraction of particles ). The form of the equation 4.1 is also plotted on figure 4.4, using the theoretical values of 2.5 for intrinsic viscosity and 1.56 for the crowding factor. This choice of crowding factor derives from a maximum packing fraction of 64%, which is the well-known value for random packing of spheres, first suggested by Scott [59].

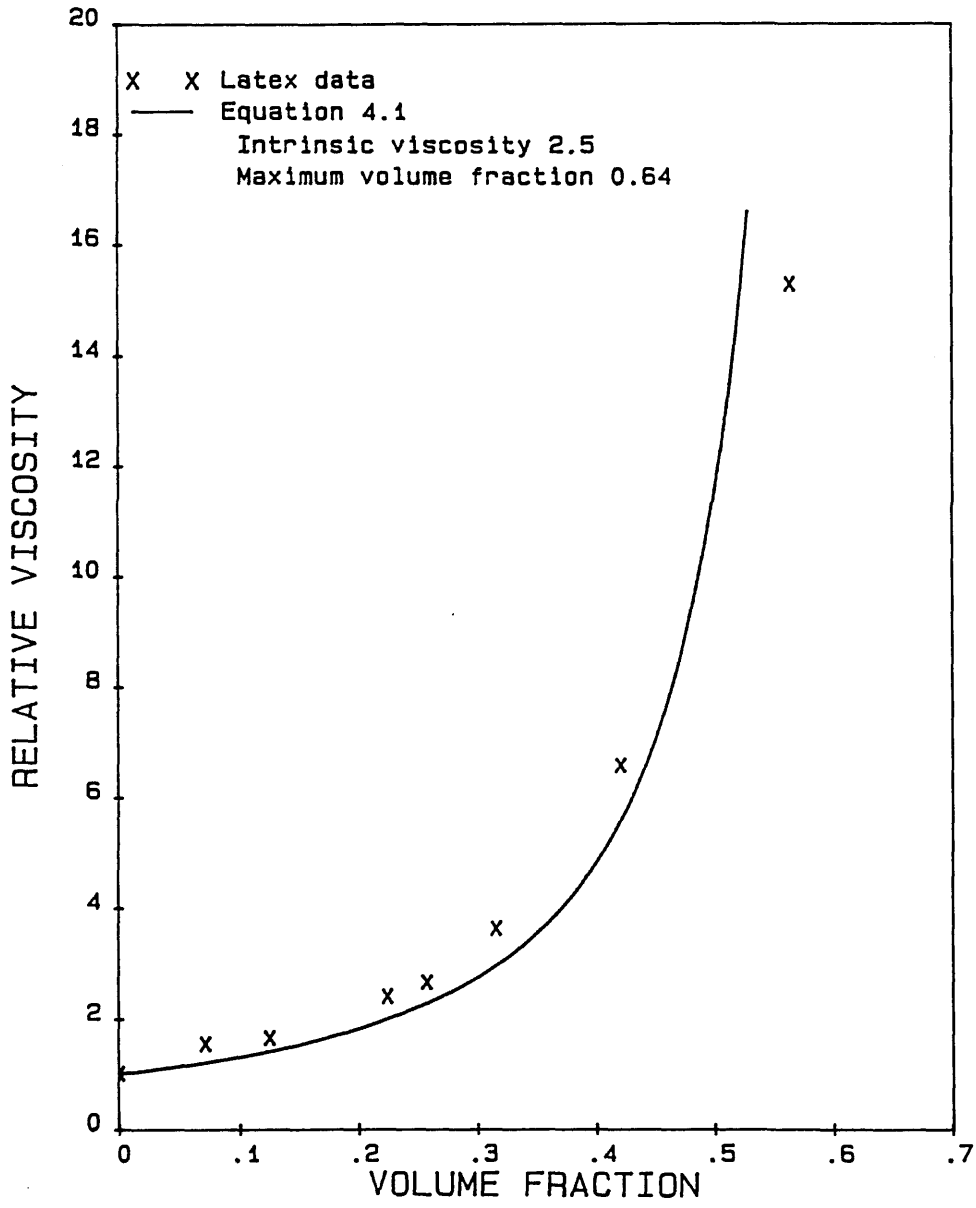
(iv) Zeta potential

Measurement of zeta potential for each particle suspended in buffer solution was performed on a Malvern Zetasizer. The values were as follows:

| | | |
|---|---|---|
| 1.8 microns diameter, | pH 7 | -56mV |
| | pH 4 | -38mV |
| 0.55 microns diameter, | pH 7 | -55mV |
| | pH 4 | -34mV |

FIGURE 4.4

RELATIVE VISCOSITY OF LATEX AS A FUNCTION OF CONCENTRATION



(v) Filter cake properties

Batch filter tests on the smaller latex particles were carried out using an Amicon cell with a PM30 polysulphone membrane. The object was to determine if a latex filter cake was compressible. From the dead-end filtration equation ( Coulson and Richardson [68] ), the specific resistance of the filter cake can be calculated. Specific cake resistance ( dimensions of m $kg^{-1}$ ), evaluated at pressures of 1.7, 3.5 and 5.2 bar, yielded values of $3.8x10^{13}$, $4.0x10^{13}$ and $4.3x10^{13}$m $kg^{-1}$. These values indicate that latex filter cakes have low compressibility.

## 4.5 Rig Operations and Experimental Interpretation

### 4.5.1 Run procedures

Initially, the membrane was characterized by measuring its inner diameter and hydraulic resistance. The inner diameter was estimated by weighing the volume of water needed to fill the cylindrical membrane tube of known length. Hydraulic resistance was obtained from the first few permeate flow readings ( if flow did not decline rapidly ) or by extrapolating the first two values of permeate flow back to zero time.

At the beginning of an experiment, $30dm^3$ of latex suspension at 0.5wt% was recirculated around the rig at $20^oC$. For a desired combination of flowrate and pressure, the valves and pump were pre-set using a dummy test section. This was removed and the membrane introduced to the rig while recirculation continued through the bypass loop. The two valves at the test section ends were opened and computer logging was initiated. Logging cycles were set between 30 and 120 seconds. Experiments were generally continued until a steady permeate flowrate was achieved. Pump delivery pressure was constant during a run but, due to the build-up of filter cake, the tube flowrate tended to decline. The valve at the test section exit was gradually opened to maintain the correct flowrate.

At the end of a run, the free channel diameter was estimated by the water volume technique described above. Backwashing was used to remove filter cake, which was dried and weighed.

### 4.5.2 Data evaluation

Directly-logged parameters were not particularly useful for evaluating filtration perfomance and had to be transformed into other variables. The parameters used for comparison were channel diameter, cake mass, cake voidage, specific cake resistance ( dimensions of $m^{-2}$ ), permeate velocity, shear stress at the cake/suspension interface and cake growth rate.

Two methods were used to estimate the tube diameter. The direct water method was only used at the end of a run, although during an experiment, axial pressure drop measurements gave an estimate of channel diameter using the following equation:

$$d_f = (k Q_t^2 / P_D)^{1/5} \qquad (4.2)$$

where k is an experimentally-determined constant for each membrane type, $Q_t$ is the volumetric tube flow, and $P_D$ is the frictional pressure drop down the length of the membrane tube.

Cake mass was determined by drying and weighing the backwashed latex, and cake voidage obtained from a re-arranged version of equation 3.19. Specific resistance of the cake was evaluated by combining equations 3.20 and 3.21, eliminating $P_w$. Measurement of bulk latex concentration was done by drying a known quantity of feed and weighing the residue.

Permeate velocity at the cake surface is given by

$$v_w = Q_p / \Pi d_f L \qquad (4.3)$$

where $v_w$ is the permeate velocity, $Q_p$ is the volumetric permeate flowrate and L is the length of the membrane segment used. Shear

stress at the cake/suspension interface is expressed by

$$\tau = P_D d_f / 4 L_t \qquad (4.4)$$

where $L_t$ is the total length of membrane tube used. In the case of laminar flow, with small tube pressure drops, shear stress was estimated from the Poiseuille equation.

The parameter evaluated with least accuracy was cake growth rate. Filter cake mass was determined by using the permeate flowrate data in equation 3.22. Cake mass was plotted against time, from which the gradient dm/dt was obtained graphically. The inaccuracy of this method to evaluate dm/dt was not the graphical technique, but the implicit assumption that no decrease in permeate flow was due to increasing blockage of membrane pores by particles. This blocking problem is discussed in 5.1.3 .

### 4.5.3 Experimental uncertainties

Most of the problems associated with accurate parameter determination originated from fluid-mechanical effects in the membrane tube and adjoining pipework.

#### (i) Pressure loss effects

In all experiments, the channel diameter of the membrane tube was always less than 7mm, while the tappings for pressure gauges were positioned in the 1/2" pipe attached to the membrane module. This change of dimension meant that at tube flowrates in excess of $2dm^3min^{-1}$, the Bernouilli effect became significant, which resulted in the test section operating pressure being lower than the average of pressure gauge readings. Frictional losses due to the contraction and expansion at the test section couplings become larger with increasing crossflow. Knowing the tube flowrate, inlet and outlet pressures, and test section geometry, it is possible to compensate for these effects. Formulae to predict friction losses can be found in Massey [69]. Using Massey's method it was determined that for

Carbosep geometry, 72% of the gauge pressure drop was due to friction loss on the walls of the membrane ( or filter cake ), while for Ceraver tubes the value was 80% . Both constants are approximately valid over a range of channel diameters. Combining expressions for friction loss, Bernouilli effect and gravity head loss enables the pressure at any point of the membrane test segment to be evaluated. The effective transmembrane pressure is then approximated by the following equation:

$$P_m = k_1 P_i + k_2 P_o - k_3 Q_t^2 / d_f^4 + k_4 \qquad (4.5)$$

where $P_i$ and $P_o$ are the measured inlet and outlet pressures, and the k values are constants for each membrane type. While pressure drop is usually a function of $d_f^{-5}$, it may be approximated as $d_f^{-4}$ by manipulating the constant $k_3$. This makes equation 4.5 rather less complicated, as both friction losses and Bernouilli factors are incorporated into the third term.

The standard rule for entry lengths in turbulent flow is 50 pipe diameters [69], therefore any problems arising from the development of the tube flow were overcome by using the first 0.3m for Carbosep and 0.45m for Ceraver membranes as entry length sections. No permeate flow measurements were taken from these lengths. During the course of experiments it was noted that the cake at the test section entrance was thinner than at the outlet, but only by around 10% . This was attributed to the increased turbulence and thinner boundary layers at the module entrance.

(ii) Porous walls

The effect of flow through a porous wall on the axial boundary layer is not clearly understood. There is obviously a slip velocity at the wall/fluid interface, but this has largely been neglected in membrane studies. Singh [70] reported that the slip velocity at a permeable boundary may be expressed by

$$u_s = \Theta (du/dy)_w \qquad (4.6)$$

where $\Theta$ is a slip coefficient taking values of order $10^{-1}$m. This treatment is not appropriate for the system under investigation here because, even at moderate tube flows, equation 4.6 suggests a slip velocity of the order of 100m $s^{-1}$ at a shear rate of $1000s^{-1}$. Beavers and Joseph [71] proposed a rather more complex expression for the slip velocity, but this relies heavily on material parameters which are not easily evaluated. In a study to investigate the boundary layer velocity profile over a flat-sheet ultrafiltration membrane, Dodds [64] found no deviation from the usual wall log-law profile for solid walls. However, he used high resistance membranes with a low permeate velocity.

Belfort [72] indicates that the relationship between the friction factor of porous walls with and without applied suction is of the form

$$f_s / f_{ns} = 1.2 - 40\,(Re_w / Re^{3/4}) \qquad (4.7)$$

where the Reynolds numbers are based on radial wall velocity and mean tube velocity respectively. This appears a rather strange expression, because when $Re_w$ approaches zero, the friction factor ratio tends to 1.2 . In this thesis, it was noted that the tube pressure drop did not depend on permeate velocity for either membrane tube. Therefore, in all analysis, the boundary layer was assumed to be of the same form as for a solid wall.

(iii) Transition to turbulence

One last fluid-mechanical uncertainty in this work was the Reynolds number at which the transition to turbulence occurred. There is some dispute in the literature over this, with Porter [9] and Beavers et. al. [73] suggesting the transition occurs at a Reynolds number rather less than 2000, while Schlichting [65] indicates that suction stabilizes a laminar velocity profile, so that the transition occurs at a higher Reynolds number.

The approach to these uncertainties in this study has been to assume a no-slip boundary condition ( while acknowledging that there

is an unquantifiable slip velocity ) and that the turbulent transition occurs at Re = 2000.

An error analysis is presented in appendix E for all experimental and derived parameters used in this work.

## 4.6 Experimental Campaigns

The work programmes fall into three broad sections: the steady state filtration condition, characterizing the mechanism of filter cake resuspension, and the dynamic approach to steady state from an initially clean membrane and from a previous equilibrium state.

### 4.6.1 Steady state behaviour

The main comparison used to quantify the equilibrium filtration condition was the relationship between permeate velocity and interfacial shear stress when permeate velocity had stabilized. Variables used to investigate steady state behaviour were:

(i) tube flowrates between 0.5 and 8.5$dm^3min^{-1}$
(ii) operating pressures from 0.8 to 3.0 bar
(iii) suspension pH of 7.0 and 4.0
(iv) all three membrane types
(v) suspensions of monodisperse particles of both sizes
(vi) a mixed suspension of 50wt% of both particles

### 4.6.2 Resuspension effects

This programme of work was carried out to determine if any back-transport of particles took place from the filter cake. A cake of known dimensions was allowed to develop on the membrane and was then subjected to a change of crossflow conditions. Average channel diameters ( estimated by the pressure drop method of equation 4.2 )

and permeate flowrate were monitored to determine if resuspension had taken place. The main parameters investigated were:

(i) membrane type - Carbosep M4 and Ceraver 0.1 micron
(ii) tube flowrates to 12$dm^3min^{-1}$
(iii) operating pressures from 0.1 to 2 bar
(iv) particle diameters of 0.55 and 1.8 microns

### 4.6.3 Dynamic behaviour

The main aim of this work was to quantify the particle sticking factor as a function of cake development in support of the proposed friction force model. A secondary aim was to examine the time taken to reach ( and return to ) equilibrium and thus understand the role of diffusive mass transport in the system. Variables investigated were:

(i) tube flowrates from 0.5 to 3.0$dm^3min^{-1}$
(ii) membrane type - Carbosep M4 and Ceraver 0.1 micron
(iii) particle diameters of 0.55 and 1.8 microns

# CHAPTER 5

## RESULTS AND DISCUSSIONS

This chapter is comprised of three main sections. In the first, the results of experiments to validate the frictional force model for steady state filtration are presented. These results are discussed with respect to other filtration models. Work to determine mechanisms of cake erosion is described in the next section; while the final major section outlines dynamic filtration experiments, which are discussed with respect to the frictional force balance. A short summary concludes the chapter.

### 5.1 Steady State Filtration

#### 5.1.1 Monomodal particle distribution

The scope of this experimental programme was described in the previous chapter. For each of the parameters under investigation, the rig was run until permeate flow had stabilized. At that point, the variables of free channel diameter; cake mass, voidage and specific resistance; permeate velocity at the cake surface and shear stress were evaluated. A complete example calculation is given in appendix D, while all experimental data is tabulated in appendix C.

(i) Characteristics of the filter cake

It is seen from the data in appendix C, that in most runs the estimated voidage agrees well with the value of 0.36 found for random packing of spherical particles [59]. In the cases where voidage was not evaluated, a value of 0.36 has been assumed. Using this value of voidage in the Carmen-Kozeny equation together with the particle diameters of 0.55 and 1.8 microns, the theoretical values of specific resistance are $5.2 \times 10^{15} m^{-2}$ and $4.9 \times 10^{14} m^{-2}$. Comparison of these predictions with data ( appendix C ) shows that the experimental values are in approximate agreement with the Carmen-Kozeny equation. Exact correspondence between experiment and theory is unlikely as specific resistance is very sensitive to voidage: from the Carmen-

Kozeny equation, a 1% inaccuracy in estimating voidage produces about a 4% error in specific resistance over the range $0.3 < e < 0.4$. Also, the Carmen-Kozeny equation assumes a truly random arrangement of particles, therefore any structuring of cake will almost certainly produce a different specific resistance to that expected.

Unlike many other studies of membrane filtration, operation with latex particles produced filter cakes of up to 2mm thickness. The experimental values of channel diameter are plotted in figures 5.1, 5.2, and 5.3 for each of the membrane types. The frictional model suggests that particles continue to deposit until the axial shear force exceeds the normal force. This theory is supported by the data because at higher crossflows the equilibrium cake thickness was reduced.

(ii) Permeate velocity - shear stress relationship

In order to validate the frictional model for crossflow equilibrium, a plot of permeate velocity versus shear stress should be linear ( cf. equation 3.17 ). The data from all experimental runs are plotted using axes of permeate velocity vs. shear stress in figure 5.4 and permeate velocity vs. the product of particle diameter and shear stress in figure 5.5. A large range of experimental conditions were tested to demonstrate the validity of the model: shear stress varied from 1 to 58N $m^{-2}$, while permeate velocity took values between $2x10^{-5}$ to $26x10^{-5}$m $s^{-1}$.

These graphs show that the relationship of permeate velocity and shear stress is indeed linear, in agreement with the frictional force balance model. The slope of the permeate velocity - shear stress equilibrium lines appears to be an increasing function of particle diameter, also predicted by the model. The friction theory suggests that the permeate velocity - shear stress slope depends on particle diameter to the first power. This is because a linear axial velocity profile near the cake surface has been assumed. However, from figure 5.4 the values of the slopes ( using both Carbosep and Ceraver data ) are $2.6x10^{-5}$ and $2.8x10^{-6}N^{-1}m^{3}s^{-1}$ for the large and small particles respectively. This is a ratio of 9:1, while the

FIGURE 5.1

CHANNEL DIAMETER vs. CROSSFLOW ( CARBOSEP MEMBRANE )

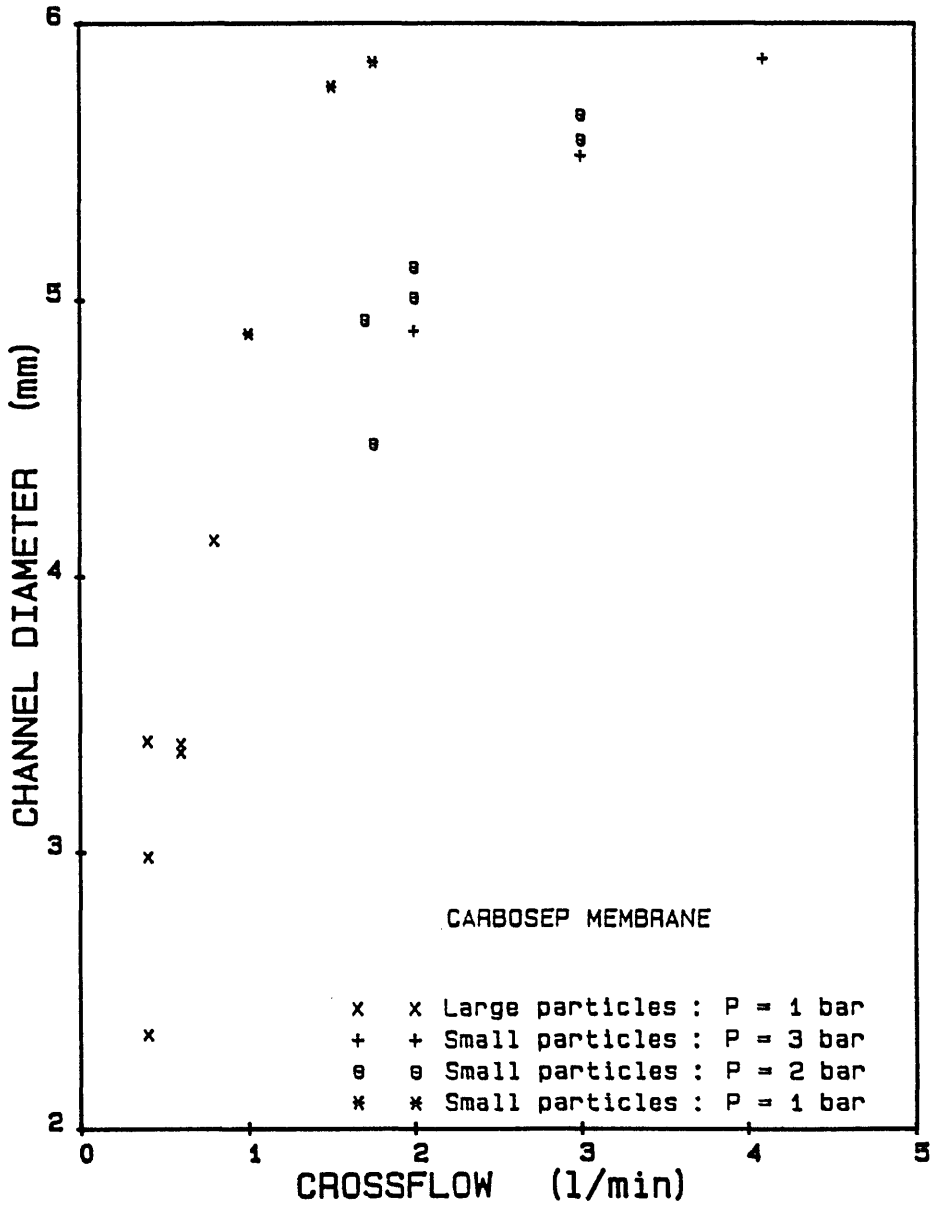


FIGURE 5.2

CHANNEL DIAMETER vs. CROSSFLOW ( CERAVER 0.1 micron MEMBRANE )

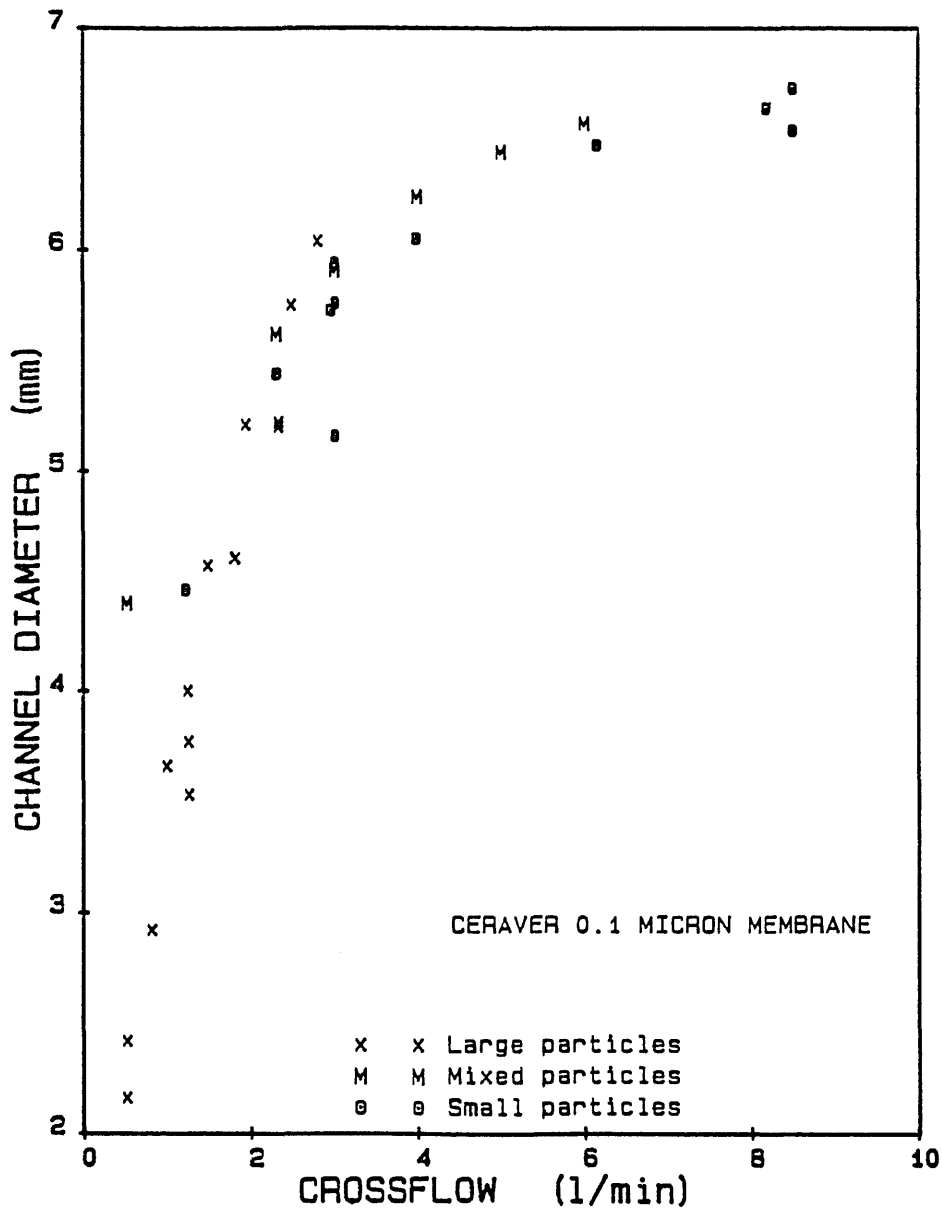


FIGURE 5.3

CHANNEL DIAMETER vs. CROSSFLOW ( CERAVER 0.2 micron MEMBRANE )

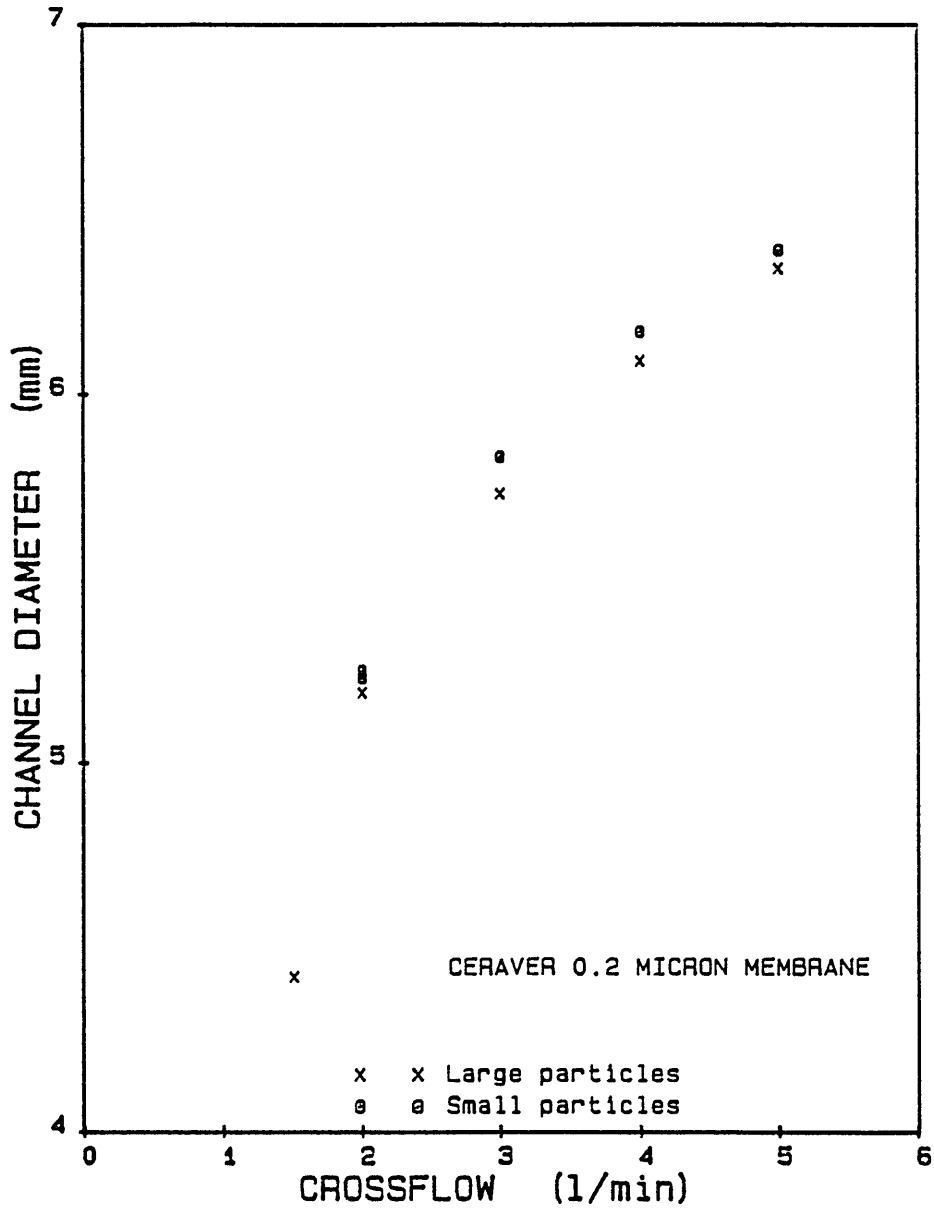


FIGURE 5.4

PERMEATE VELOCITY vs. SHEAR STRESS

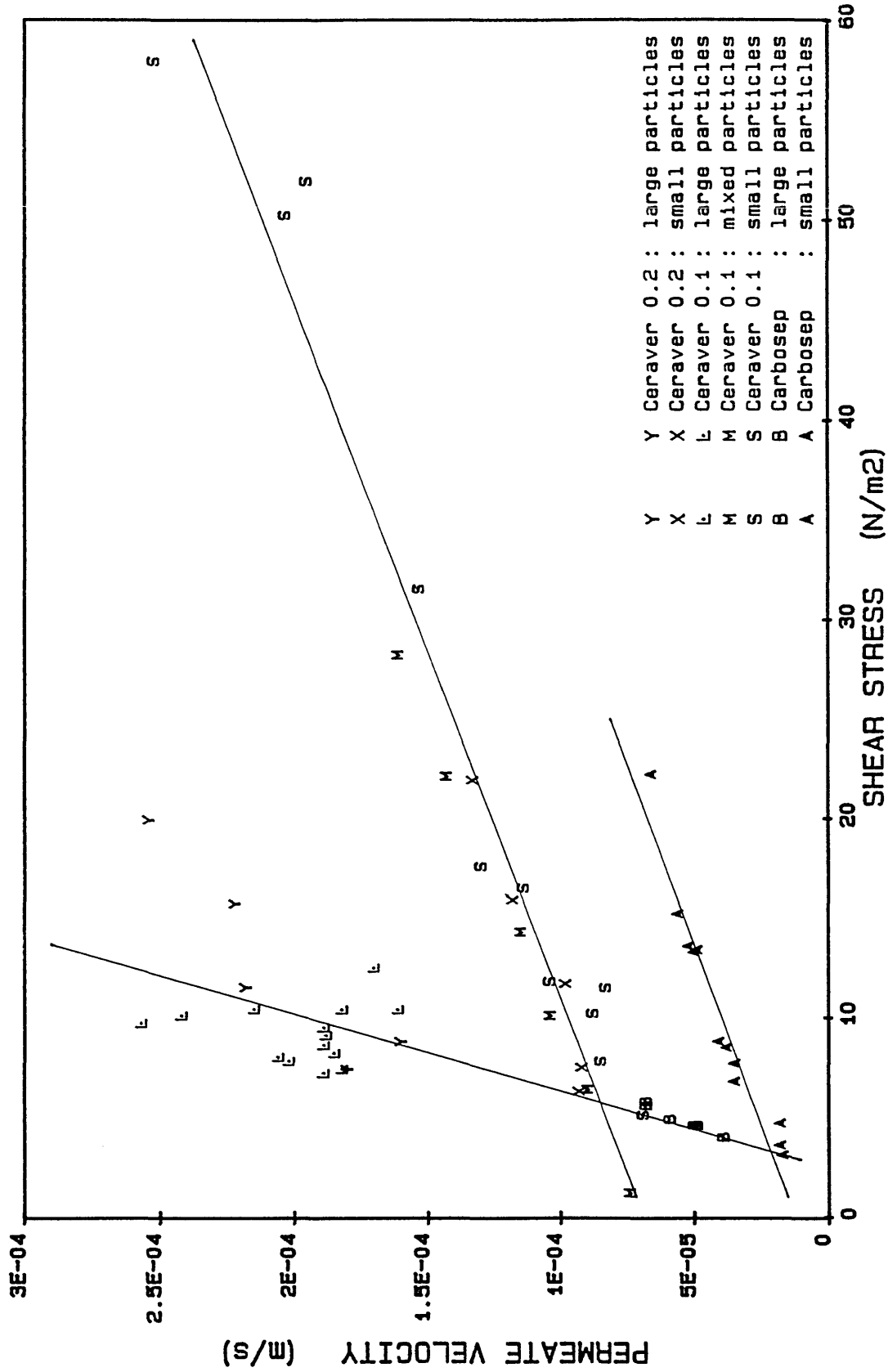
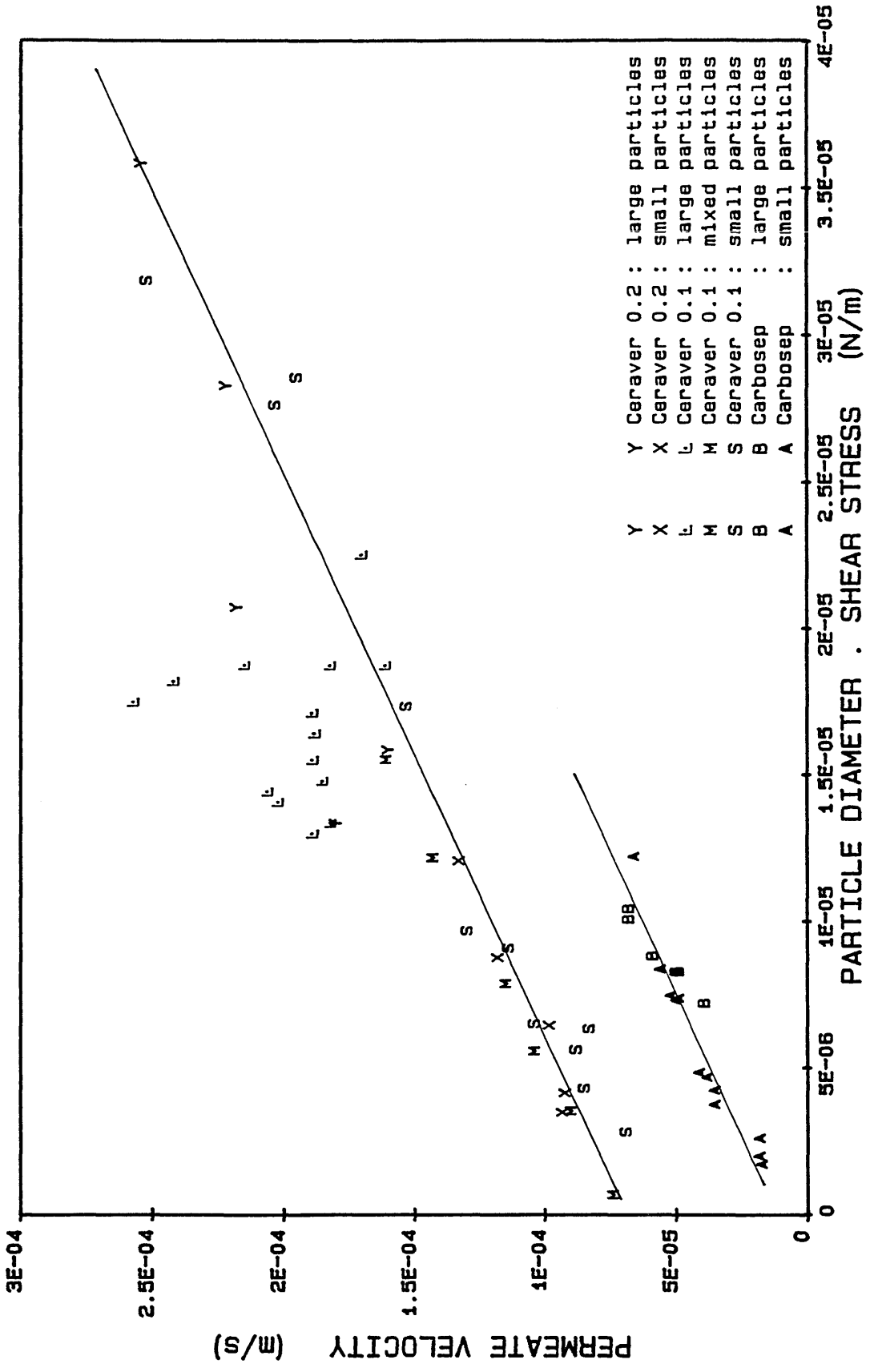


FIGURE 5.5

PERMEATE VELOCITY vs. PRODUCT OF PARTICLE DIAMETER AND SHEAR STRESS



particle diameters are in the ratio of 3.3:1. When the data for the set of experiments using only Carbosep membranes are considered, the slopes of the equilibrium lines for the two particles are in the ratio 6:1. This second comparison of equilibrium line slopes is probably more reliable due to the scatter of points from experiments using large particles with Ceraver membranes.

Due to crowding effects of particles and turbulence in the boundary layer, it is possible that the assumption of a linear velocity profile is not strictly valid. A higher-order relationship for the viscous sub-layer axial velocity profile would yield a higher-order dependence for the permeate velocity - shear stress slope with respect to particle size. This might be expressed

$$v_w \sim d_p^{\,n} \tau \qquad (5.1)$$

In order to yield a ratio of equilibrium line slopes of 6:1, the value of n must be about 1.5.

The most striking feature of figures 5.4 and 5.5 is the intercept of the permeate velocity - shear stress loci for experiments using small particles with both Ceraver membranes. This is seen most clearly in figure 5.5. Extension of the frictional force model to incorporate interparticle forces with hydrodynamic forces takes the form of a linear relation between permeate velocity and shear stress, with the intercept determined only by the interparticle force contribution. It has been demonstrated earlier that for the latex particles used, both Van der Waals and electrostatic forces may be of similar magnitude to the hydrodynamic forces acting on a particle at the filter cake surface. The intercepts of figures 5.4 and 5.5 suggest the importance of interparticle forces. The fact that only one category of experiments shows this behaviour is rather unexpected. Although the experiments using Carbosep membranes with both particles and Ceraver membranes with large particles seem to exhibit small intercepts, these intercepts are not significant due to experimental error ( an error analysis for all variables is given in appendix E ). It should be noted that in crossflow experiments, the equilibrium loci can never reach the axes as permeate velocity and

shear stress must remain finite.

As intercepts in permeate velocity - shear stress loci were found, and with the frictional force model suggesting that this is due to the effect of interparticle forces, experiments attempting to clarify the role of these forces were performed. By operating at pH 4 rather than pH 7, the electrostatic contribution to the particle interactions was altered. The measured change in zeta potential of the smaller latex particles is from -55mV at pH 7 to -34mV at pH 4, which if all other parameters remain equal, reduces the electrostatic repulsion between spheres to 38% of the original value at pH 7 ( cf equation 3.11 ). Some of the experiments using small particles with Carbosep membranes and all of the experiments with small particles and 0.2 micron Ceraver membranes were carried out at pH 4. Figures 5.4 and 5.5 show that the data for 0.1 and 0.2 micron Ceraver membranes are coincident. An expanded section of figure 5.5 is presented in figure 5.6, showing the Carbosep data with distinction between points at different pH. Despite such a reduction in electrical repulsion force it must be concluded that, under these experimental conditions, electrostatic interactions do not substantially influence the filtration equilibrium.

Comparison of the cake voidage from experiments using Carbosep and 0.1 micron Ceraver membranes with small particles yields

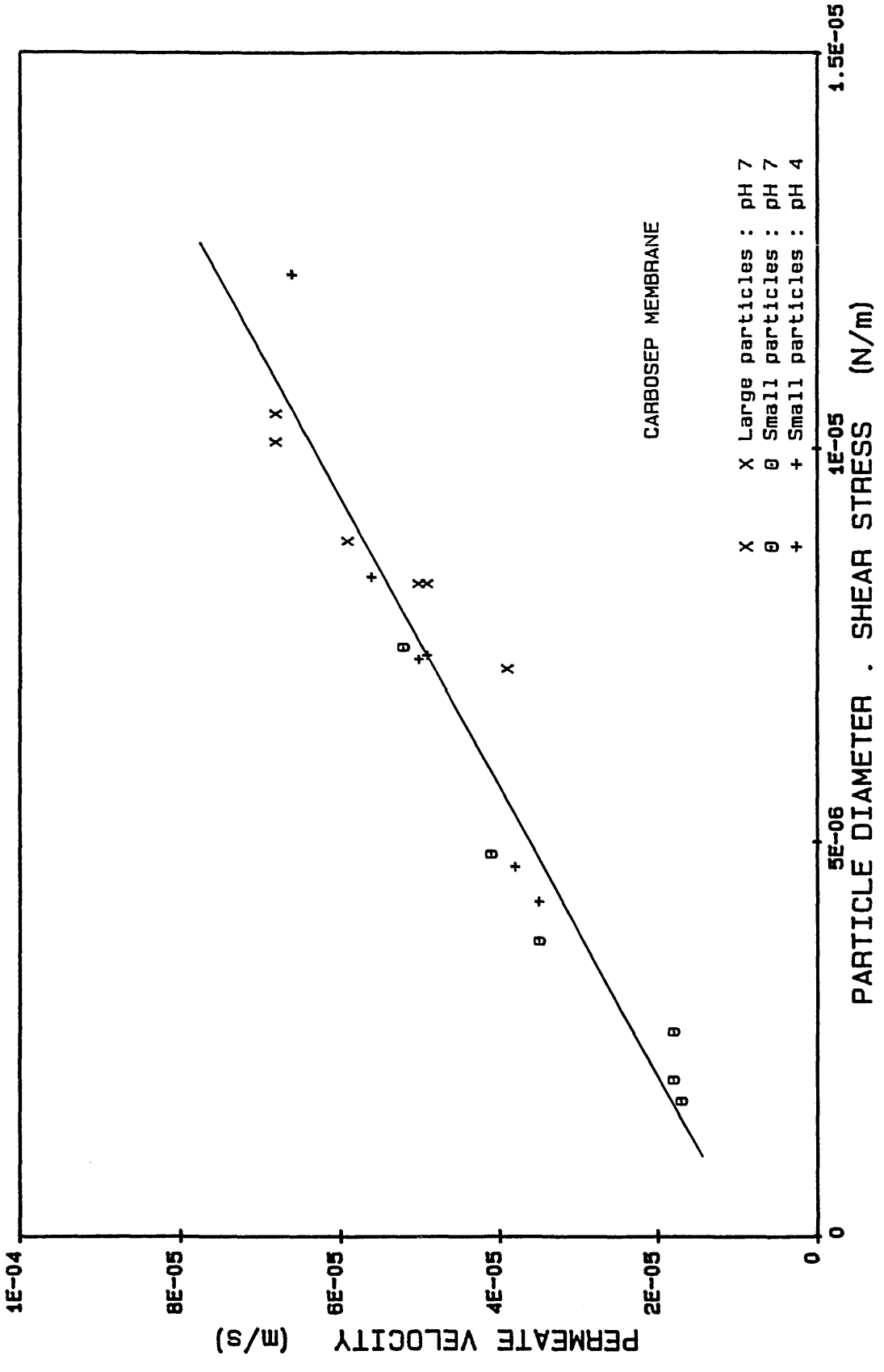
TABLE 5.1 CAKE VOIDAGE FOR SMALL PARTICLE EXPERIMENTS

| SYSTEM | No. of expts. | Mean Voidage | Std. Deviation |
|---|---|---|---|
| Carbosep | 4 | 0.396 | 0.023 |
| 0.1 Ceraver | 5 | 0.356 | 0.007 |

When the student's t test is applied to these two data sets, the test statistic is 154 with 3 degrees of freedom. The significance of this

FIGURE 5.6

PERMEATE VELOCITY vs. PRODUCT OF PARTICLE DIAMETER AND SHEAR STRESS



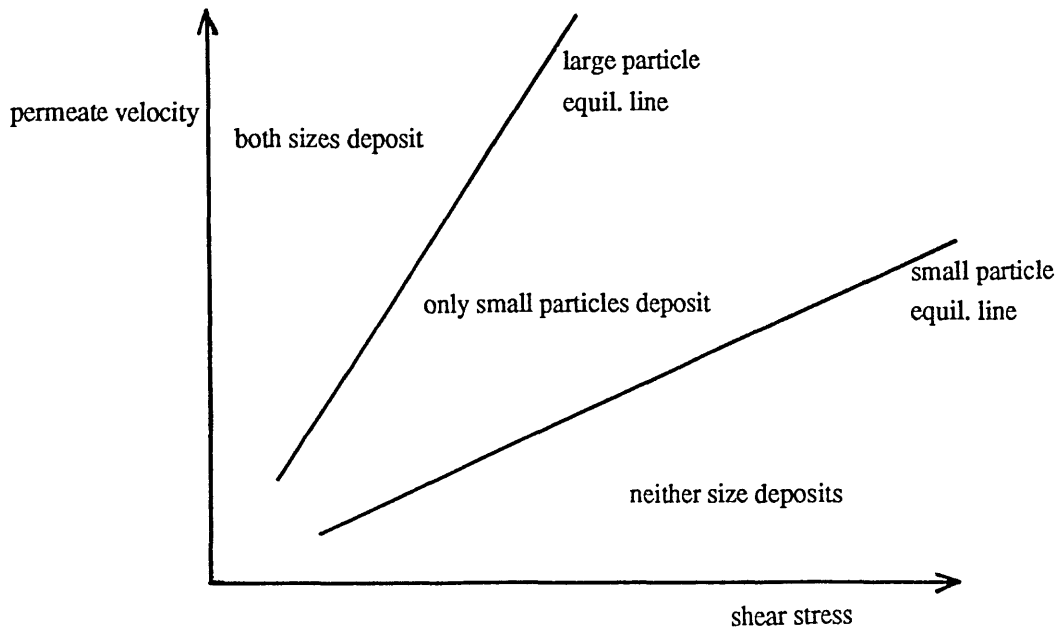
is in excess of 99.9% , which means that the difference in the two mean voidages is almost certainly not due to random error. This discrepancy in voidage indicates a different cake structure or a

change of interparticle separation in the cake between tests using Carbosep and Ceraver membranes. At closer separation distances, both electrostatic and Van der Waals forces become more important. This could be the cause of the observed intercept in the Ceraver membrane / small particle data. In addition to the observed differences in cake voidage, there is a higher permeate velocity in experiments using Ceraver membranes. Due to this enhanced mass flux, there will be more interactions between a depositing particle and those approaching the cake surface. This situation may also produce an intercept in the permeate velocity - shear stress relationship. While these proposed explanations for the intercept only occurring in the Ceraver data are physically sound, evidence to test them directly would be very difficult to produce.

### 5.1.2 Bimodal particle distribution

A simplification of figure 5.4 is shown in figure 5.7 below

FIGURE 5.7 SCHEMATIC CONDITIONS FOR FILTRATION EQUILIBRIUM



With a knowledge of membrane hydraulic resistance and the hydrodynamic operating parameters of the membrane module, initial values of permeate velocity and shear stress can be fixed. The regimes of deposition for a specific particle size are defined by the lines shown on figure 5.7 : if initial operation is in the region above the equilibrium line then deposition occurs. While each equilibrium line has been verified for that particle size in a monodisperse suspension, the friction force model should still be valid for a dilute suspension containing a mixture of particle sizes. Of particular interest in figure 5.7 is the region between the two equilibrium lines, where only one particle size should deposit from a bimodal mixture.

This behaviour was investigated using a Ceraver 0.1 micron tube with a particle mixture containing 56wt% of the 0.55 micron particles with the balance of 1.8 micron particles. A variety of flowrates were used at an operating pressure of 1 bar. Experiments were performed until filtration equilibrium was reached, taking note of the permeate velocity, shear stress and channel diameter at the beginning and end of each run. Filter cake was backwashed and the particles were redispersed in water by stirring and application of ultrasound. Measurement of the particle size distributions were performed on a Malvern Mastersizer.

Figure 5.8 shows the mass fraction of smaller particles in the filter cake with respect to the axial flowrate used. Above $5dm^3min^{-1}$ the percentage of smaller particles was constant at about 95% . Upon lowering the crossflow, some larger particles began to be incorporated into the cake, until at the lowest flow, the cake was of the same composition as the feed. This result is put into the context of the particle equilibrium lines in figure 5.9. The initial and final co-ordinates for each experiment are plotted on permeate velocity - shear stress axes and are joined by a line. The numbers shown on these lines are the mass percentages of small particles in the final filter cake. Figure 5.9 shows that the deposition of particles from a mixture is governed by the individual equilibrium lines for each particle, obtained from monomodal experiments. Very little deposition of large particles is observed when the initial

FIGURE 5.8

INFLUENCE OF CROSSFLOW ON THE SIZE DISTRIBUTION OF DEPOSITED PARTICLES

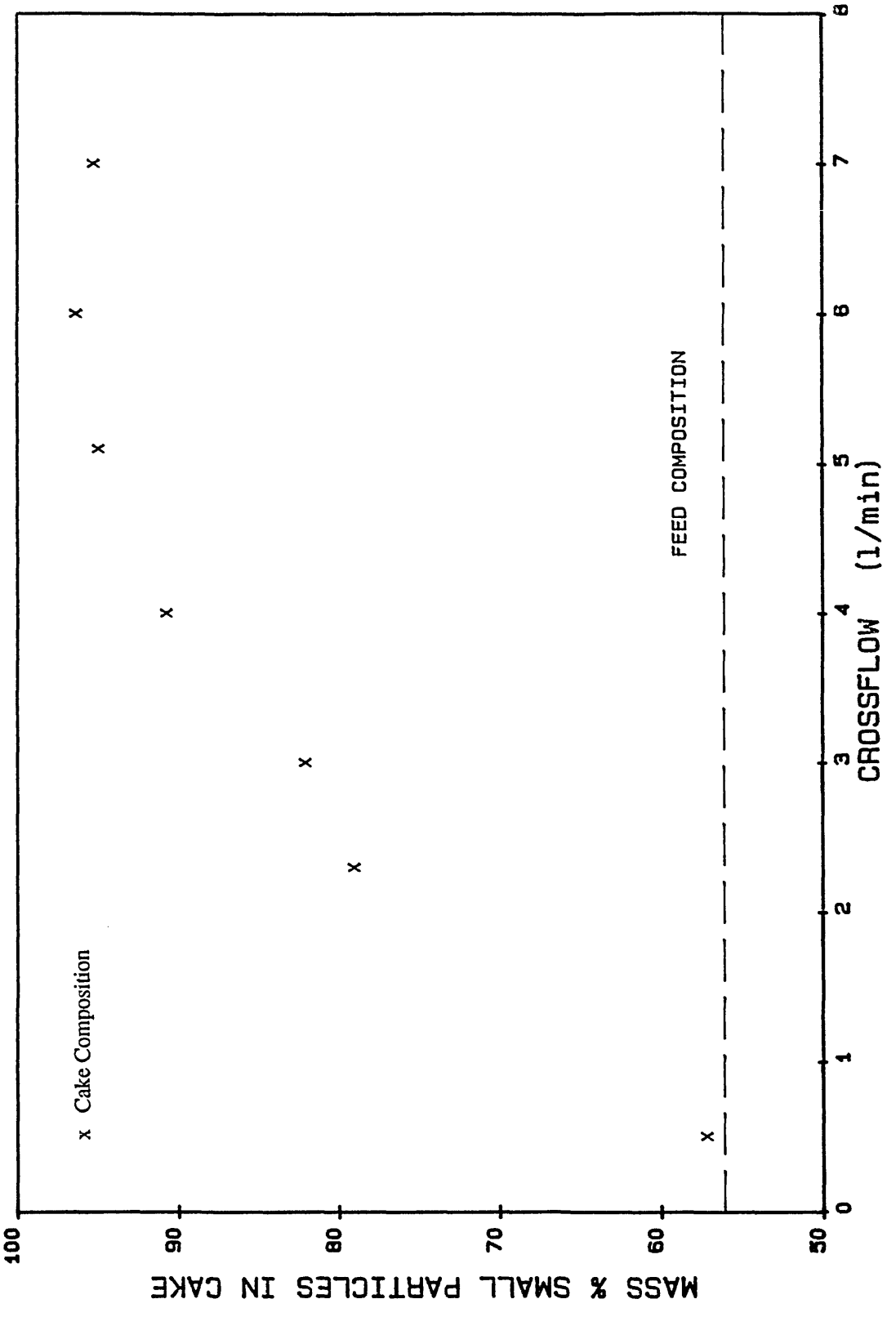
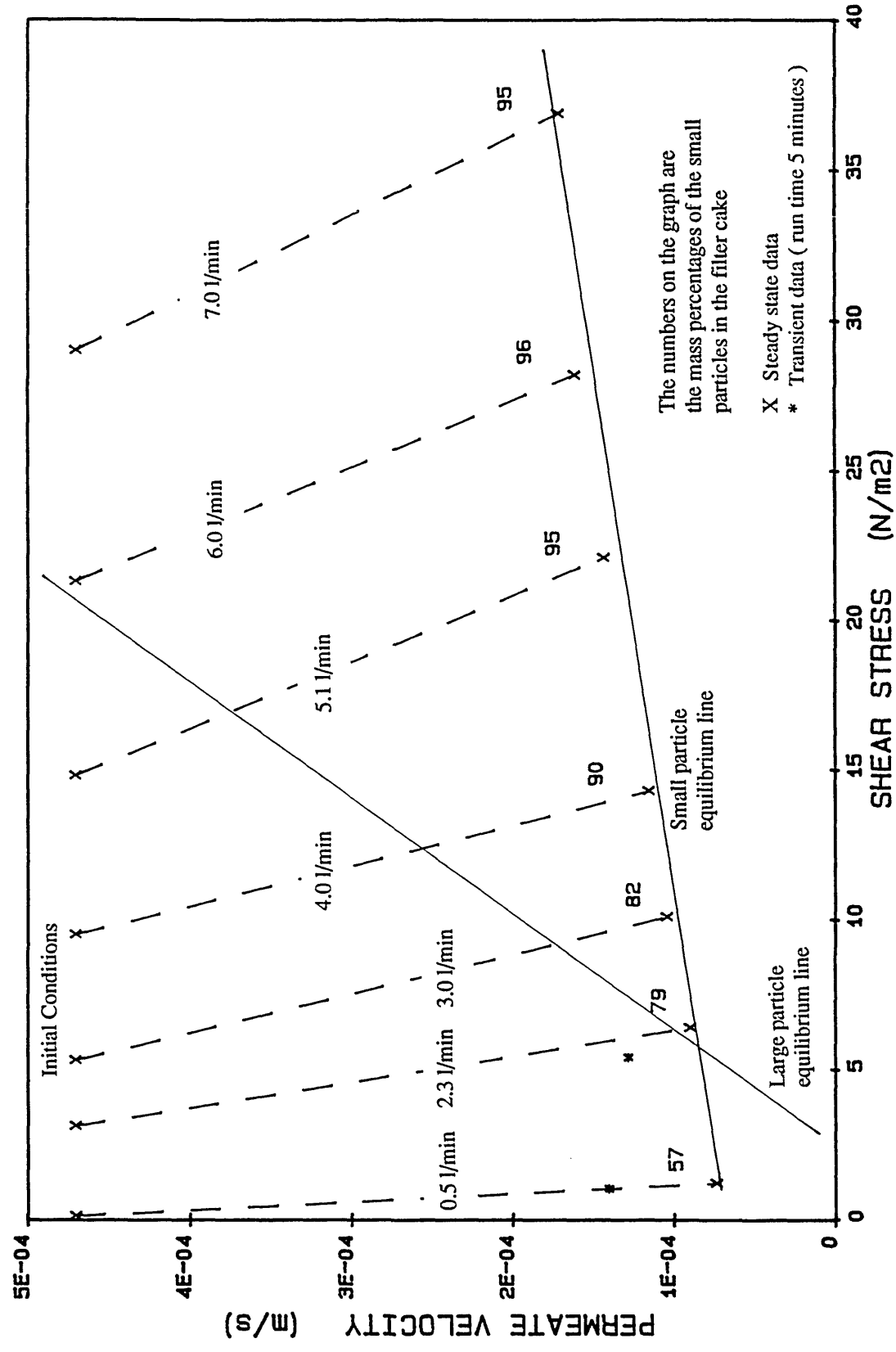


FIGURE 5.9

INFLUENCE OF EQUILIBRIUM LINES ON DEPOSITING PARTICLES



values of ( $\tau$, $v_w$ ) are below the large particle equilibrium line, while increasing deposition is seen as the initial co-ordinate moves further into the depositing region.

In addition to these steady state investigations, experiments were carried out at the lowest two crossflows in which filtration was halted after five minutes and the particle size distribution of the cake was measured. The particle distributions in these cases were the same as the bulk. These transient data are marked on figure 5.9 and fall in the depositing region for both particles. This evidence confirms that, for a mixture of particles in the bulk, each particle species continues to deposit until its equilibrium line is reached: beyond that point, only smaller particles can be incorporated in the cake.

Similar classification of a particle mixture was reported by Fischer & Raasch [47] and Lu & Ju [48], who confirmed that increased crossflow hinders the deposition of larger particles. Figure 2.4 (re-printed from [47] ) illustrates the particle distributions of feed and filter cake at different crossflows.

The ability to predict particle classification is not unique to the friction force model: the inertial lift velocity and shear-induced hydrodynamic diffusion coefficient are functions of particle size. However, the controlling influence of the equilibrium line, as demonstrated by figure 5.9, gives good support to the frictional model. The transient experiments, halted after five minutes, give particular weight to the friction theory: both lift and SIHD arguments predict a continous decline in the fraction of large particles deposited with time. This is due to the gradual increase of back-transport with increasing shear rate. The abrupt change in deposited particle size distributions ( figures 5.8 and 5.9 ) can only be explained by a frictional force model.

### 5.1.3 Difficulties in defining the filter cake

In previous sections it has been assumed that the total

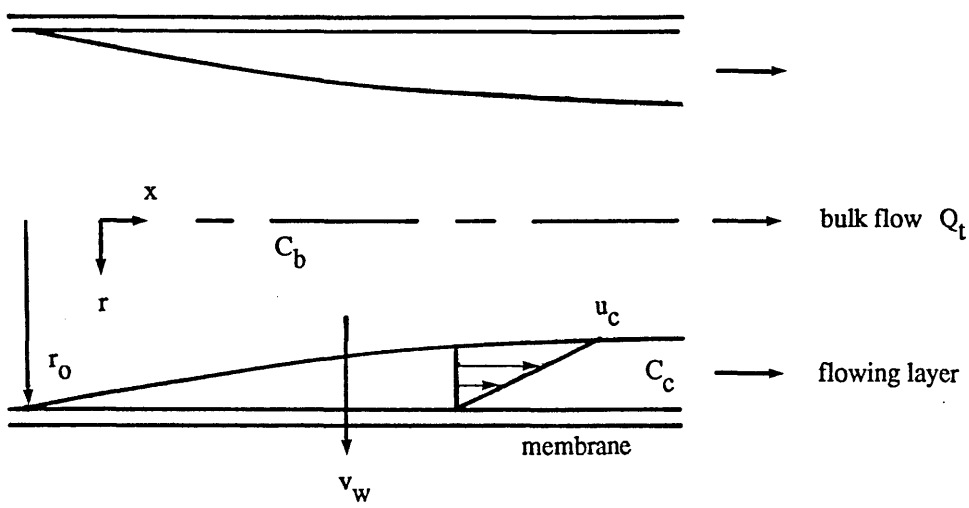
hydraulic resistance is due to the combined resistance of the membrane and static filter cake. The problem with this assumption is that the two interfaces of the fixed cake, with the suspension and the membrane, may also generate additional hydraulic resistances. These extra resistances arise from the presence of a flowing cake over the static layer and by pore blocking.

(i) Flowing filter cake

The convection models of Leonard [11] or Davis [13] require a balance between axial convection of a flowing concentrated layer along the membrane, with the forced convective flux towards the wall. The decline in filtration performance is attributed to the resistance of this layer. Under some circumstances these convective models also allow for a static filter cake.

While it is possible that turbulence in the boundary layer will destroy a flowing cake, no direct evidence of destruction has been established in this work. It is therefore assumed that a flowing cake may exist. Its hypothetical hydraulic resistance must be estimated to assess its influence on filtration. Typical dimensions of such a cake are evaluated in this section. Figure 5.10 shows the geometry of a flowing cake.

FIGURE 5.10 DEVELOPMENT OF A FLOWING PARTICULATE LAYER



The flowing cake layer is assumed to have a linear velocity profile, a solids content of 60% ( the volume fraction of a static cake is 64% ) and a relative viscosity of 20 ( cf figure 4.4 ). Other assumed parameters, typically found in this work, are a shear stress of 10N $m^{-2}$, channel diameter of 6mm, bulk solid content of 0.5wt% and a Ceraver membrane with a permeate velocity of $10^{-4}$m $s^{-1}$. Over the entire membrane length the mass transport rate approaching the cake is given by

$$\frac{dm}{dt} = v_w A_m C_b \qquad (5.2)$$

where $A_m$ is the surface area of the cake and $C_b$ is the bulk concentration. For the conditions above, the mass transport rate over the whole tube length is approximately $6.6 \times 10^{-6}$kg $s^{-1}$.

Calculation of the volumetric flowrate due to axial convection is done by integrating the velocity profile of the concentrated layer at the tube outlet between the limits of the wall and its surface. The usual log law of the wall is assumed to apply ( $u^+ = y^+$ ), so that the velocity profile is of the form

$$u(r) = (r_o - r)\tau/\mu_c \qquad (5.3)$$

where $r_o$ is the channel radius and $\mu_c$ the viscosity of the flowing layer. Upon the appropriate integration of equation 5.3 and multiplication of the resulting volumetric flowrate of cake by the concentration of the flowing layer, the axial mass transfer rate is expressed

$$\frac{dm}{dt} = \frac{2\Pi C_c \tau}{\mu_c}\left[\frac{r_o^3}{6} - \frac{r_o r^2}{2} + \frac{r^3}{3}\right] \qquad (5.4)$$

where $C_c$ is the concentration of the flowing layer. Equating the mass transport rates given by equations 5.2 and 5.4 allows iterative solution for the height of the layer at the tube exit. In this example, the height is approximately 0.02mm. Application of the Carmen-Kozeny equation suggests that the specific resistance of a cake composed of 60% solids is about 2/3 of the value for a cake of 64% solids. The conclusion to be drawn is that even if a concentrated

particle layer were to be formed above the static cake surface, its height and specific resistance would be much smaller than those values for the fixed cake. In this work, any hydraulic resistance of the flowing cake can therefore be neglected.

(ii) Pore blocking

If particles to be filtered are smaller or of comparable size to the membrane pores, then some pore blocking is inevitable. In the experiments described in this work, no such difficulties were experienced when using Carbosep membranes due to the very small pore size; however, it can be perceived that operating a 0.1 or 0.2 micron membrane with 0.55 and 1.8 micron particles could result in significant pore blocking. Plate 4.1 shows the scale of the alumina particles comprising the top surface of a 0.2 micron Ceraver membrane - these appear to be of similar size to the latex particles used.

Pore blocking effects were experimentally observed when using both varieties of particle with Ceraver membranes, particularly at high crossflow. At low crossflows ( perhaps 2-3$dm^3min^{-1}$ ) cake built up to a thickness of 1-2mm at steady state. If filtration was continued, no further flux decline was observed in periods of up to 3 hours. However, at higher crossflows ( 6-8$dm^3min^{-1}$ ) a steady permeate flow was not reached for many hours, after which time the cake thickness was often less than 0.05mm. The permeate flow from these latter experiments was lower than that recorded at low crossflow. This defies the assumption that all loss of filtration performance is due to the growth of filter cake. The data in appendix C shows that the specific cake resistance when using Ceraver membranes appears to be an increasing function of crossflow. The small variation in voidage between runs cannot account for this effect.

These observations can be explained by the proposal that in the first stages of filter cake growth, pore blocking develops with time due to the relative freedom of movement of particles on the membrane surface. Upon further deposition of particles, the cake becomes more

rigid and particles adjacent to the membrane become immobile, thus preventing any further pore obstruction. At high crossflows where thick cakes are unable to develop, the particles at the membrane surface remain mobile, therefore pore blocking is not arrested until many pores have been fully covered. The result of this argument is that total hydraulic resistance is now composed of three terms: the original membrane resistance, an extra membrane resistance due to pore blocking and the cake resistance. From experimentation, there is no direct way of distinguishing between these factors: thin filter cakes with a low actual hydraulic resistance appear to have a much higher resistance due to the dominance of the pore blocking term. This explains the apparent drop in specific resistance of the thicker filter cakes obtained at low crossflow.

The genuine independence of specific cake resistance with crossflow can be demonstrated by considering a series of experimental runs with respect to the porous media defining equations ( 3.20 and 3.21 ). $P_w$ is eliminated from the two equations which are then re-arranged in terms of specific cake resistance ( $r_c$ ) and membrane resistance ( $R_m$ ) thus

$$r_c = k_0 + k_1 R_m \tag{5.5}$$

where

$$k_0 = \frac{2 \Pi L P_b}{Q_p \mu_o \ln (d_o / d_f)} \tag{5.6}$$

$$k_1 = \frac{-2}{d_o \ln (d_o / d_f)} \tag{5.7}$$

L is the membrane length over which permeate flowrate measurements ( $Q_p$ ) were taken, $d_o$ and $d_f$ are the original and final channel diameters. Equation 5.5 is perfectly general as it only represents the definition of hydraulic membrane resistance (3.20) and Darcy's equation (3.21). The object of this approach is to let $R_m$ become the sum of hydraulic membrane resistance and the resistance due to pore blocking. It is reasonable to assume that the pore blocking resistance term takes a constant but unknown value, determined only by the cake packing arrangement. For each run, the k values can be

evaluated from experimental data and $r_c$ plotted against a range of $R_m$. If these lines of equation 5.5 intersect at one point, then the true independence of specific cake resistance with crossflow is demonstrated. At the point of intersection, the value of $R_m$ is the sum of the clean membrane resistance and the pore blocking contribution.

The data used for this comparison were from the sequence of runs using large particles with a 0.2 micron Ceraver membrane operating at 1 bar ( L = 0.102m and $d_o$ = 6.75mm ). In each case, the membrane had an original resistance of $1.2 \times 10^{11} m^{-1}$ and the cake voidage was about 0.36. Using the experimental data, the following values were determined

TABLE 5.2 PORE BLOCKING CORRECTION

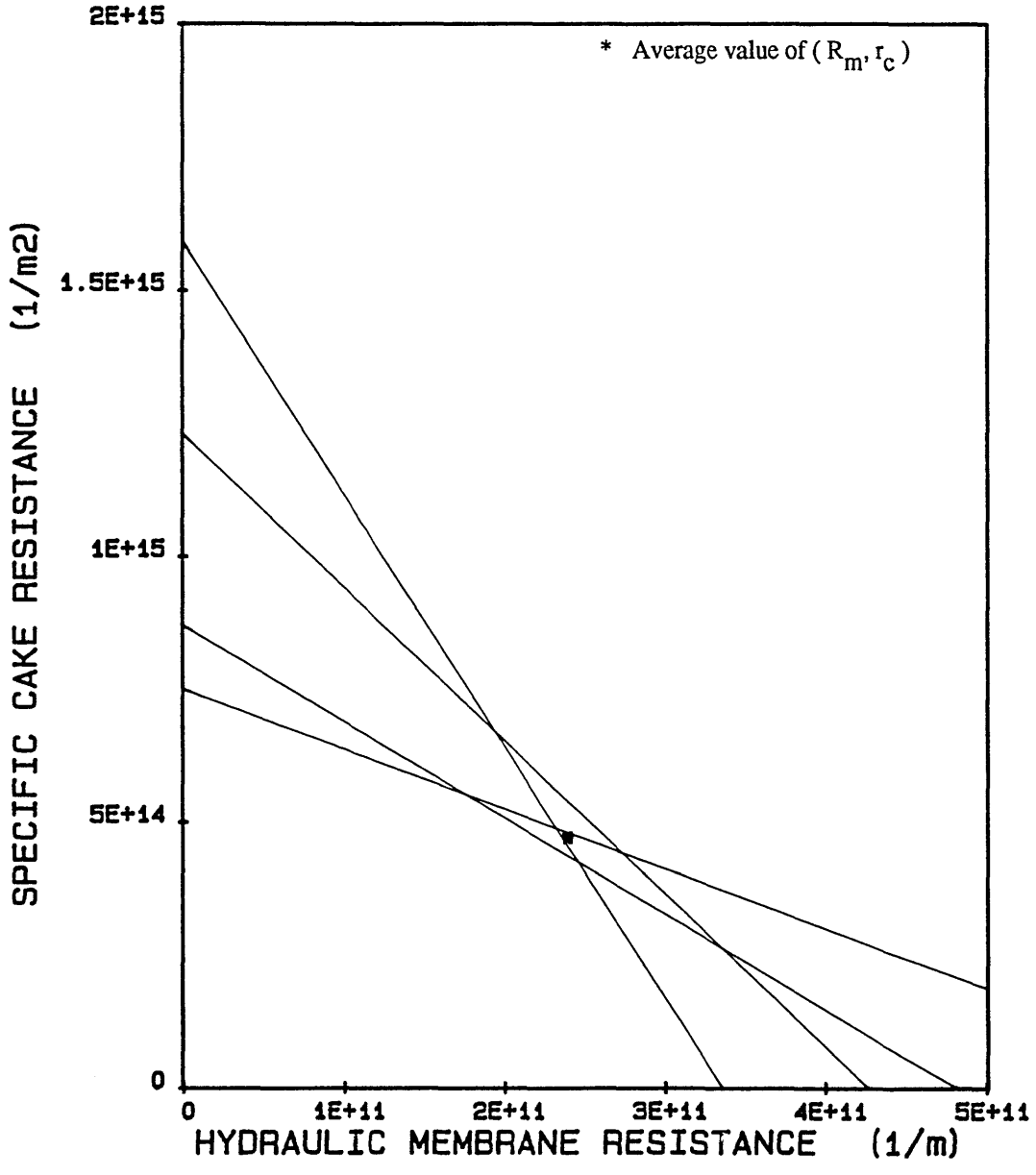
| RUN | $Q_t$ ( $dm^3 min^{-1}$ ) | $r_c$ ( $m^{-2}$ ) | $k_0$ ( $m^{-2}$ ) | $k_1$ ( $m^{-1}$ ) |
|---|---|---|---|---|
| 52 | 2 | $6.1 \times 10^{14}$ | $7.50 \times 10^{14}$ | -1130 |
| 51 | 3 | $6.6 \times 10^{14}$ | $8.70 \times 10^{14}$ | -1810 |
| 50 | 4 | $8.9 \times 10^{15}$ | $1.23 \times 10^{15}$ | -2880 |
| 49 | 5 | $1.0 \times 10^{15}$ | $1.59 \times 10^{15}$ | -4730 |

Using the k values derived for each run, specific cake resistance is plotted against membrane resistance in figure 5.11 ( cf. equation 5.5 ). The four lines cross in one region of the graph suggesting that the effective membrane resistance is $2.4 \times 10^{11} m^{-1}$ ( including the pore blocking term ) and the specific cake resistance is $4.7 \times 10^{14} m^{-2}$. Comparing this specific cake resistance with the Carmen-Kozeny value of $4.9 \times 10^{14} m^{-2}$ ( e = 0.36 ) demonstrates that specific resistance is independent of crossflow.

Pore blocking considerations do not influence the steady state $v_w$ - $\tau$ data provided that blocking has ceased before particulate

FIGURE 5.11

CORRECTION FOR PORE BLOCKING



deposition, although one minor effect is that the specific cake resistance will always be an overestimate of its true value. It must be stressed that the equilibrium data presented and discussed in section 5.1.1 were not affected by pore blocking factors, as the results from experiments with filter cakes of less than about 0.05mm thickness were discarded.

### 5.1.4 Data comparison with other theories

In the previous sub-sections, the steady state filtration performance, cake properties and dimensions were discussed with respect to the frictional force model proposed in chapter 3. The application of this model explained many of the features found by experiment. To conclude discussion of steady state filtration equilibrium, the experimental data will now be reviewed with respect to the alternative models of crossflow filtration described in chapter 2. Direct comparison with data from other studies is difficult as full experimental details are rarely published.

#### (i) Axial convection

Loss of filtration performance by a flowing cake layer over the membrane or static cake has been demonstrated to be negligible in the previous sub-section. The only useful applications of axial convection models are: when a substantial cake does not form, the membrane is of sufficiently high permeability such that flux reduction by thin flowing cake layers is measurable, and pore blocking does not occur due to large differences in particle and pore sizes. In this study the first and second conditions were never met.

#### (ii) Shear-induced hydrodynamic diffusion

In the paper by Davis and Leighton [18], the expression developed for the relationship between permeate velocity and wall shear stress at steady state is of the form

$$v_w = \left[\frac{10^{-4}}{\Phi_b \mu_o x}\right]^{1/3} a^{4/3} \tau \qquad (5.8)$$

where a is the particle radius, $\Phi_b$ is the volume fraction of solids in the bulk and x is the distance along the membrane. Although derived from an entirely different physical mechanism, this expression is of similar form to the frictional equilibrium of equation 3.17. The exponent on particle radius from the SIHD model ( 4/3 ) is higher than the theoretical value of unity from the friction model. Experimentally, the exponent appears to be about 1.5 . By substituting experimental parameters into equation 5.8 ( particle volume fraction 0.005, the distance along the membrane at which permeate flow measurements were taken of 0.5m and a viscosity of $10^{-3}$N s $m^{-2}$ ) the following forms of equation 5.8 for each particle size are

$$v_w = 3.0\times10^{-6}\,\tau \;:\; d_p = 1.8\,\mu m \qquad (5.9)$$

$$v_w = 6.1\times10^{-7}\,\tau \;:\; d_p = 0.55\,\mu m \qquad (5.10)$$

These $v_w$ - $\tau$ slopes are only 12% and 22% of the corresponding experimental values of $26\times10^{-6}$ and $2.8\times10^{-6}$ $N^{-1}m^3s^{-1}$ ( cf. section 5.1.1 ).

Equation 2.11 gives the expression for the height of the concentration boundary layer developed by Davis and Leighton [18]. For typical permeate velocity - shear stress data ( figure 5.4 ) this can be evaluated as a ratio with particle diameter for the four main experimental campaigns using I = 0.083 ( this is the maximum dimensionless height of the concentration boundary layer, see figure 2.2 ). Table 5.3 shows this ratio.

TABLE 5.3 HEIGHT OF CONCENTRATION BOUNDARY LAYER

| Membrane type | ratio of concentration boundary layer height to particle diameter | |
|---|---|---|
| | Small particles | Large particles |
| Carbosep membrane | 3 | 3 |
| Ceraver membranes | 2 | 2 |

As the height of the concentration boundary layer is very small with respect to the particle size in all cases, the validity of applying the shear-induced hydrodynamic diffusion theory to the data presented in this thesis must be questioned. A concentration gradient extending over three particle diameters is physically implausible.

One final difficulty in comparing the experimental results to the SIHD theory is that the diffusive model must assume a reversible equilibrium at the cake surface: at steady state, convected mass transport is balanced by diffusion from the surface. A change of operating conditions such as crossflow or pressure should result in a corresponding change in cake dimensions until equilibrium is restored. In practice, the cake was permanent when established, therefore any reversible equilibrium model cannot be valid for this study.

(iii) Inertial lift theories

In chapters 2 and 3, it was indicated that lift forces due to inertial effects have very limited applicability in tubular crossflow filtration. All the lift theories [27-30] were developed for laminar flow profiles; no extension of the concept has been proposed for a turbulent boundary layer, although there is no reason in principle why the effect may not occur. Hall [44] measured the lift force on a

particle in a boundary layer, though not for particles situated deep in the viscous sub-layer. His results suggest that lift forces can act in a turbulent boundary layer; however, they might not result from inertial effects.

Despite lift force theory having only been applied to the laminar flow regime, if it is assumed that these forces also operate in the viscous region of a turbulent boundary layer, lift theory can be tested against the experimental data of this work. In order to make a comparison, the expression for lift velocity is assumed to be of the same form in both laminar and turbulent flow. When equation 2.16 is written explicitly, it takes the form

$$v_l \sim a^3 u_t^2 / d_f^2 \qquad (5.11)$$

In turbulent flow, the relationship between shear stress and average axial velocity is

$$\tau \sim u_t^2 \qquad (5.12)$$

Substituting 5.12 into 5.11 and equating lift velocity to permeate velocity at equilibrium produces the following result

$$v_w \sim a^3 \tau / d_f^2 \qquad (5.13)$$

Comparison of this relationship with the data of figure 5.4 shows no evidence of agreement. The exponent on particle radius is too high, and additionally, no dependence on the free channel diameter was seen in any of the experimental campaigns. While this comparison is not a rigorous assessment of the lift theory ( which only strictly applies to laminar flow ) it does suggest that lift forces are unlikely to control the filtration process.

(iv) Erosion

Similar arguments apply to the erosion and turbulent burst models as those used against shear-induced hydrodynamic diffusion. Both types of erosion ( shearing and bursting ) require a reversible

equilibrium to be established between deposition and resuspension. This was not observed, so erosion models cannot apply to the data presented in this work.

(v) Alternative frictional models

The most substantial published work using the friction force concept is that of Rautenbach and Schock [46]. However, they did not consider interparticle forces, but only hydrodynamic terms in their model. The best fit to their data was obtained by the expression

$$v_w \sim Re^{k1} (\mu/\sigma_f d_f)(a/d_f)^{k2} \qquad (5.14)$$

where the exponents were given values of k1 = 1.26 and k2 = 0.44. If a particle is contained in the viscous sub-layer and the usual velocity profile for the sub-layer ( $u^+ = y^+$ ) and a constant friction factor are assumed, then the exponents should be k1 = 2 and k2 = 1. By adopting these revised values, equation 5.14 becomes analogous to equation 3.17, but excluding interparticle force terms.

Using the two sets of exponents given above, the experimental data are presented in figures 5.12 and 5.13 in the form of equation 5.14. It is clear that the two plots are remarkably similar in shape despite the different sets of exponents used. The reason for this lies in the actual shape of any assumed velocity profile in the viscous sub-layer. In this work, the profile has been assumed to be linear, while Rautenbach and Schock assumed that the velocity profile was of the form $u^+ \sim y^{+\,0.44}$ and that the friction factor varied as $Re^{-1/4}$. In reality, the profile may have some indeterminate shape due to the presence of particles and wall suction. It is equally possible that it is not the average velocity around a particle which determines the axial force, but fluctuations about that mean. In either case, the exact value for the exponent k1 cannot be determined. In the absence of reliable information, it is most sensible to adopt a linear velocity profile.

FIGURE 5.12

RAUTENBACH ANALYSIS : LAMINAR SUB-LAYER VELOCITY PROFILE

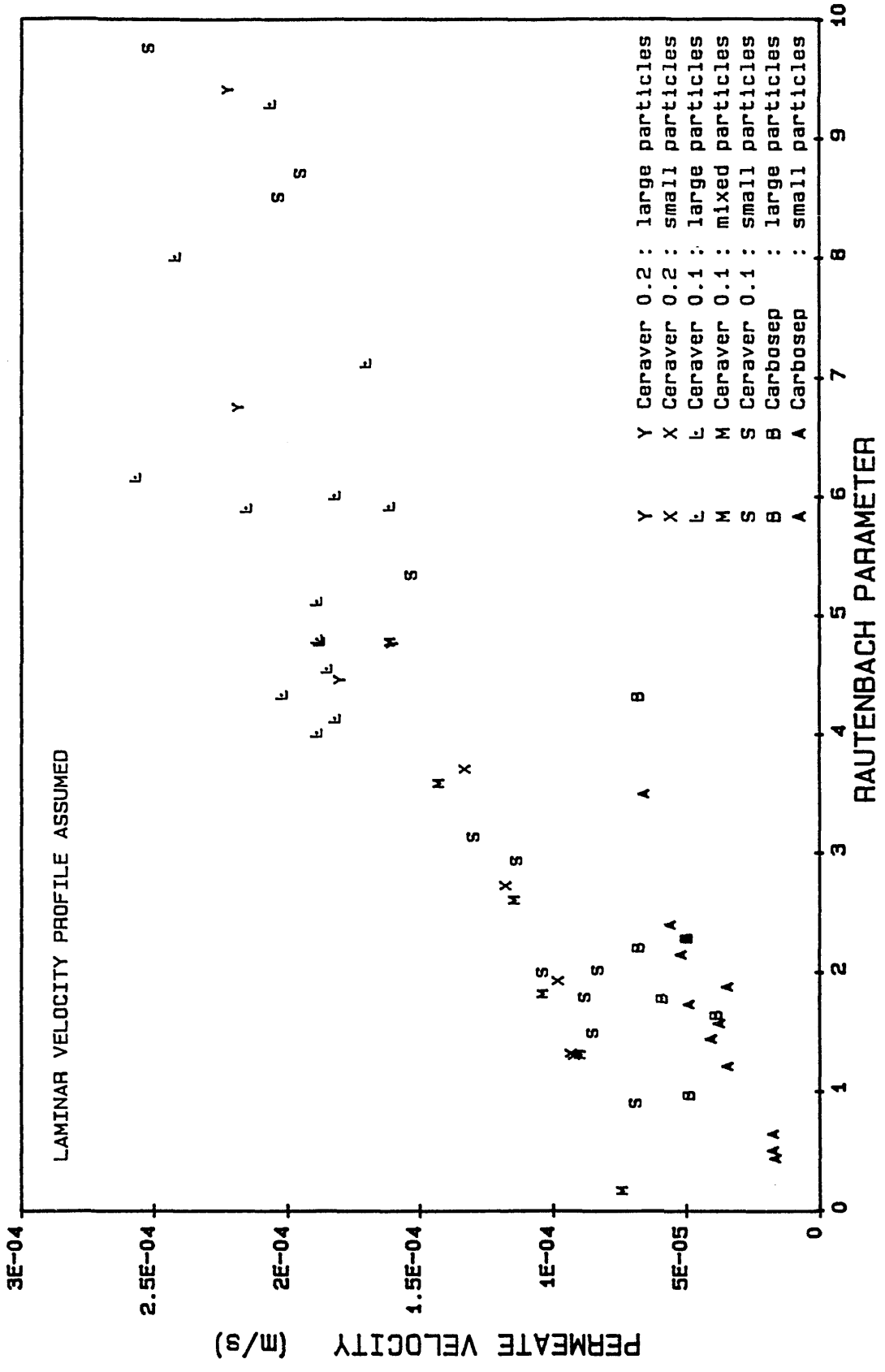
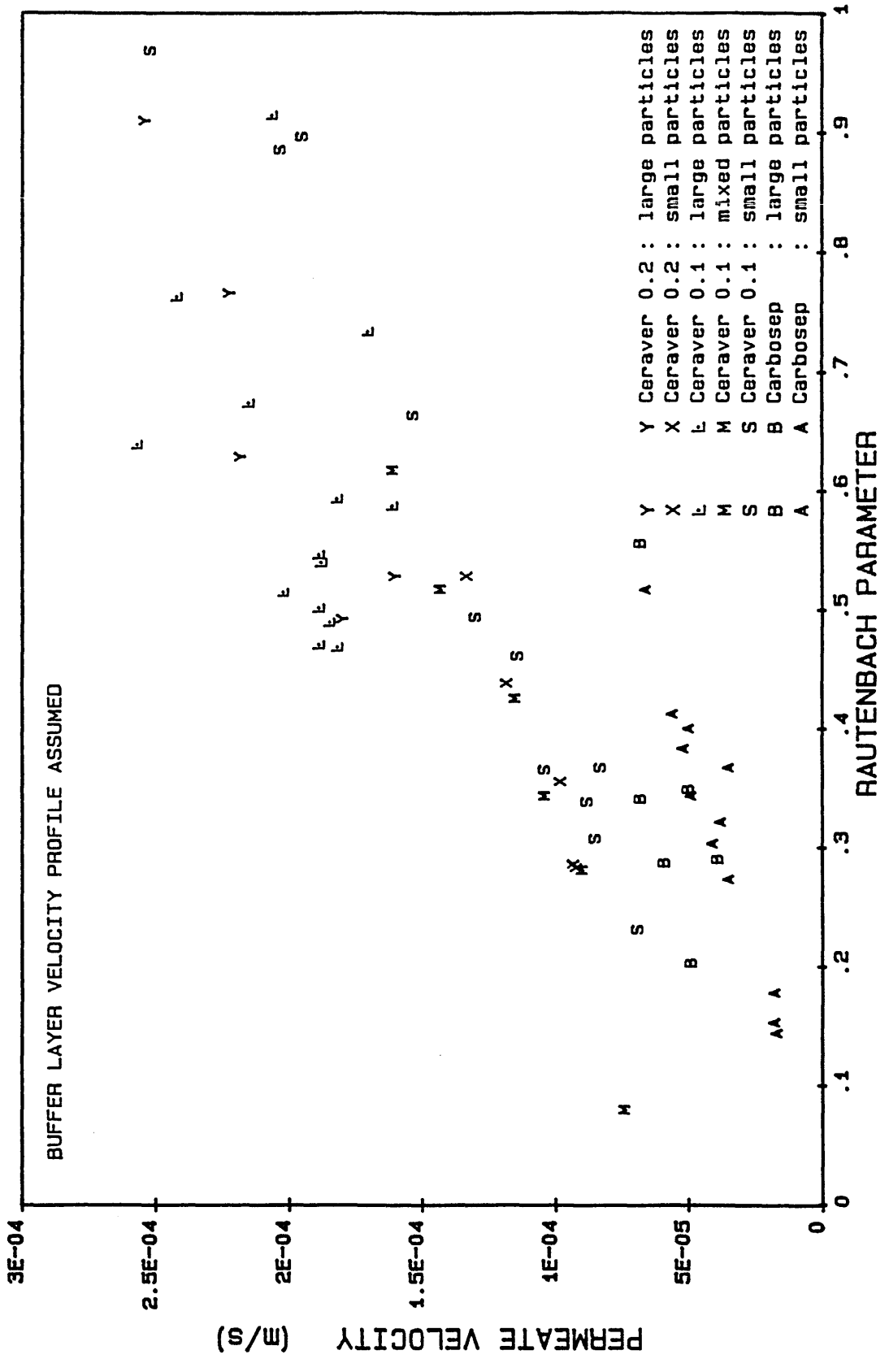


FIGURE 5.13

RAUTENBACH ANALYSIS : BUFFER LAYER VELOCITY PROFILE



A rather more serious problem with the analysis of Rautenbach and Schock is that their form of equation 5.14 suggests dependence of permeate velocity on particle radius as $a^{0.44}$. The equilibrium line slopes of figure 5.4 imply that this exponent should be considerably greater than 1.

In conclusion, Rautenbach and Schock's formulation of the frictional model reduces to a simplified version of that proposed in chapter 3 upon a more straightforward treatment of the velocity profile in the viscous sub-layer. Without considering both hydrodynamic and interparticle forces, no explanation for the intercept on figure 5.4 can be given.

## 5.2 Resuspension Effects

In section 5.1, it was noted that the steady state equilibria were not reversible: once filter cake was established, raising the crossflow or reducing the pressure did not bring a corresponding decrease in the cake thickness. However, the changes of operating conditions used were not generally large. To investigate the apparent irreversibility of cake deposition further, a series of experiments was carried out with the aim of increasing the crossflow until filter cake was resuspended.

### 5.2.1 Technique

Cake was allowed to build on the membrane at a crossflow of $0.4 dm^3 min^{-1}$ and a pressure of 2 bar for Carbosep membranes and 1 bar for Ceraver membranes, for a time of about one hour. This resulted in a thickness of perhaps 1-2mm. At that point, the crossflow was gradually raised to a new value. Channel diameter was estimated from pressure drop measurements, and wall shear stress obtained from pressure drop and channel diameter. At constant crossflow, resuspension was deemed to occur when the diameter began to increase and shear stress to decrease. If no resuspension occurred, the crossflow was raised. At the end of a run, the membrane tube was removed to examine the remaining filter cake.

These experiments were intended to give a qualitative insight into resuspension rather than rigorously define the conditions under which it occurred. Quantitative results were not considered reliable because the pressure drop method of estimating channel diameter is only applicable to cylindrical geometry. Examination of the cake after an experiment suggested that tapering was slight, although without breaking the membrane tube measurements of the cake thickness were only possible at the tube ends. It was not certain whether the cake had a gradually tapering profile down its length, as no direct in situ thickness measurements were possible.

### 5.2.2 Observations

Section 4.6.2 lists the four main parameters investigated with respect to resuspension. The results are now presented under those headings.

#### (i) Membrane type

Two membranes were used in resuspension tests: Carbosep and Ceraver 0.1 micron. Only the Carbosep membrane allowed resuspension of the filter cake. Using Ceraver membranes, crossflows to $12dm^3min^{-1}$ ( equivalent to a shear stress in excess of $400Nm^{-2}$ ) and pressures as low as 0.1 bar were used in an attempt to obtain re-entrainment. Tests using the Ceraver membrane often maintained high permeate velocities which could be held responsible for keeping the cake attached - the pressure was therefore dropped to 0.1 bar to reduce this velocity. A rather more plausible explanation is that the higher normal forces during cake building were responsible for pushing the particles to a closer equilibrium distance ( thus enhancing the attractive Van der Waals forces ) or a more stable packing arrangement. If this were so, resuspension would require more extreme crossflow conditions for higher permeability membranes.

#### (ii) Crossflow

Using a Carbosep membrane, with a channel diameter of about 5mm, little or no resuspension was observed at crossflows of less than $9dm^3min^{-1}$. At a diameter of 4mm, some resuspension occurred at $6dm^3min^{-1}$. This result suggests that shear stress is the determining factor for resuspension. In all experiments, the shear stress necessary for resuspension appeared to be in the range $150-200Nm^{-2}$. Given the approximate nature of shear stress measurement, due to uncertainties in cake geometry, more accurate specification of shear stress was not possible. Figures 5.14 and 5.15 show shear stress and channel diameter as a function of time while crossflow was increased and then held at $9dm^3min^{-1}$. From figure 5.14 it is seen that shear stress approached a value of rather less than $200Nm^{-2}$, which suggests the gradual establishment of a new equilibrium.

FIGURE 5.14

RESUSPENSION : SHEAR STRESS vs. TIME

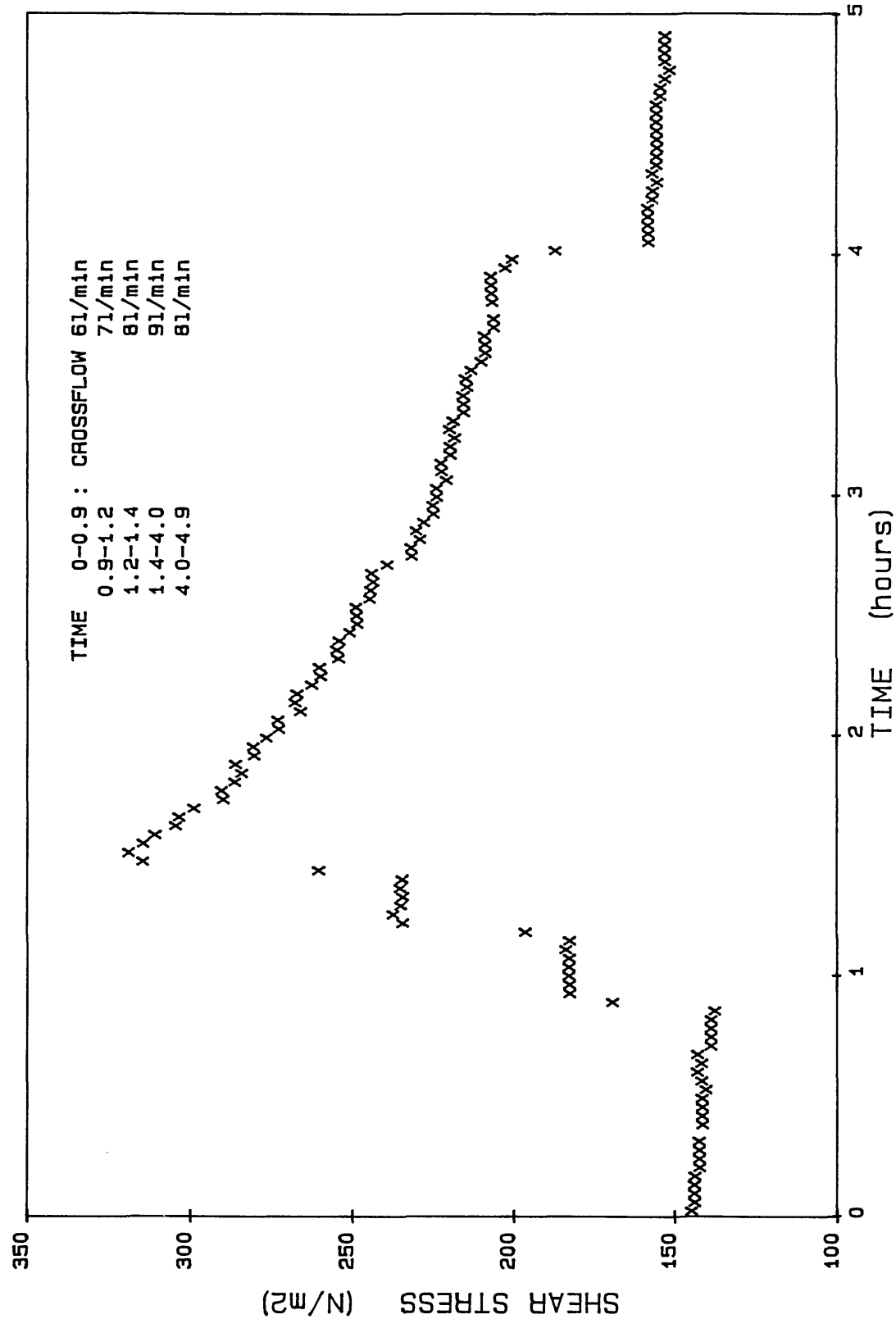
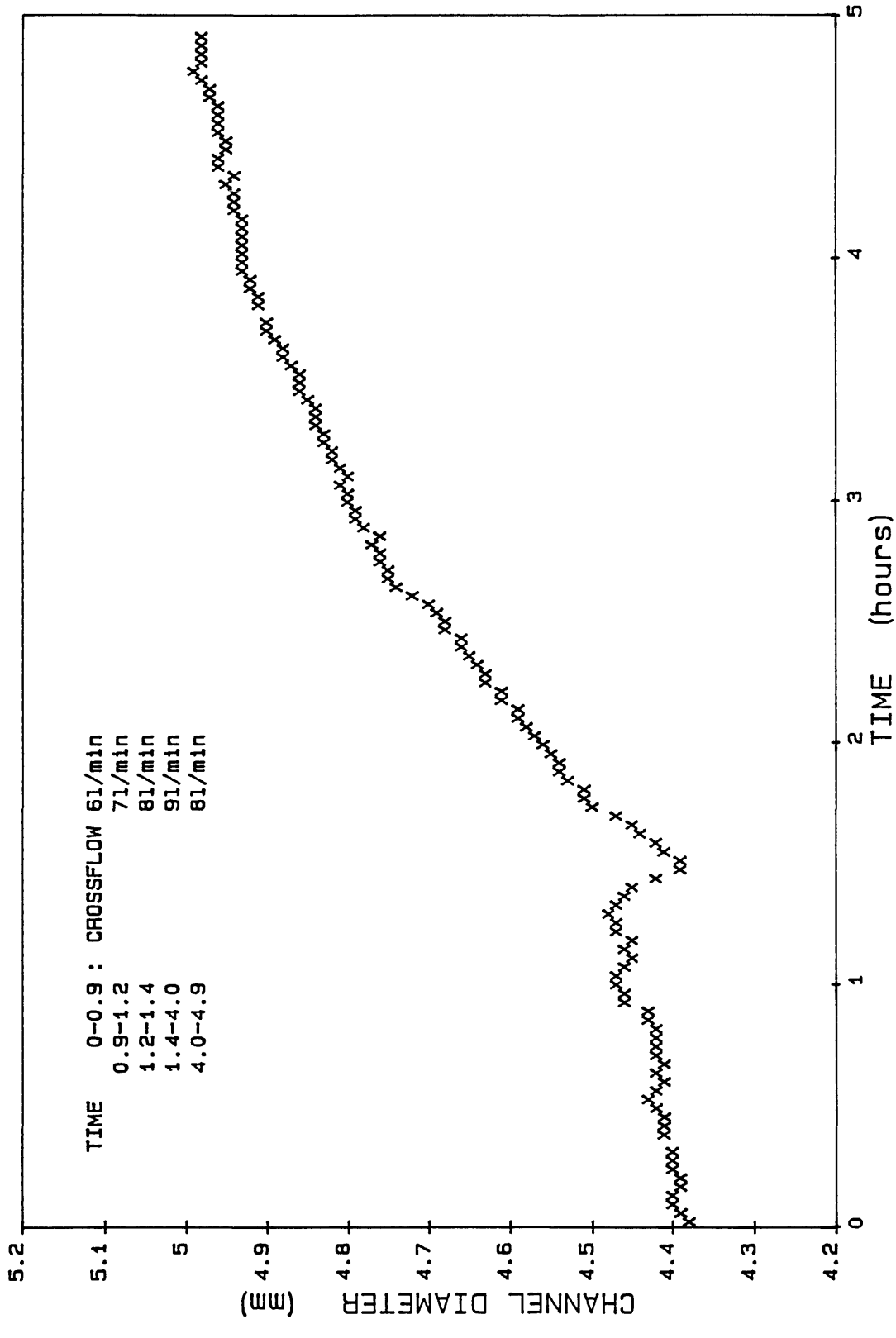


FIGURE 5.15

RESUSPENSION : CHANNEL DIAMETER vs. TIME



Examination of the membrane after removal from the rig showed that erosion of the cake was fairly uniform, although near the end of the tube some patches of the cake were completely removed. The estimated diameter from pressure drop measurements was in agreement with direct measurement at the tube ends.

The existence of a yield stress may suggest that the cake has Bingham plastic properties, however if that were true, a gradual erosion of the cake would not be found. Bingham-type behaviour requires the point of yield to be at the wall where the shear stress is greatest, so that after yielding the whole cake would move along the membrane wall. This was not observed.

During some experiments ( though not all ) there appeared to be a reduction of channel diameter just before resuspension began. Figure 5.15 illustrates the scale of this effect. This may indicate a re-fluidizing of the cake, where interparticle distances become larger and the attractive interparticle forces smaller. Romero and Davis [19] suggested this re-fluidizing mechanism in their shear-induced hydrodynamic diffusion theory, but did not consider the possibility of a threshold stress at which it occurs. In porous media, such as these filter cakes, there is an axial velocity gradient between the limits of bulk velocity deep in the cake ( determined by the hydraulic cake resistance and axial pressure gradient ) and the slip velocity at the cake/suspension interface. Raising the shear stress ( from increased crossflow ) enhances the slip velocity [70], thus magnifying the lift and drag forces on particles near the cake surface. Beyond a critical crossflow it could be proposed that the cake expands so that axial drag forces overcome the interparticle forces holding the cake together. This would result in an erosion-type resuspension until a new equilibrium was reached.

(iii) Pressure

This parameter did not seem to affect resuspension in the same way as crossflow, despite its controlling influence on permeate velocity. At conditions of pressure and crossflow such that

resuspension occurred, reduction of the operating pressure caused no significant increase in the resuspension rate. This feature is shown by figure 5.16. Upon reduction to extremely low pressures, a sudden change in channel diameter was observed. Subsequent visual inspection revealed that large sections of the cake had been removed from the end section of the tube.

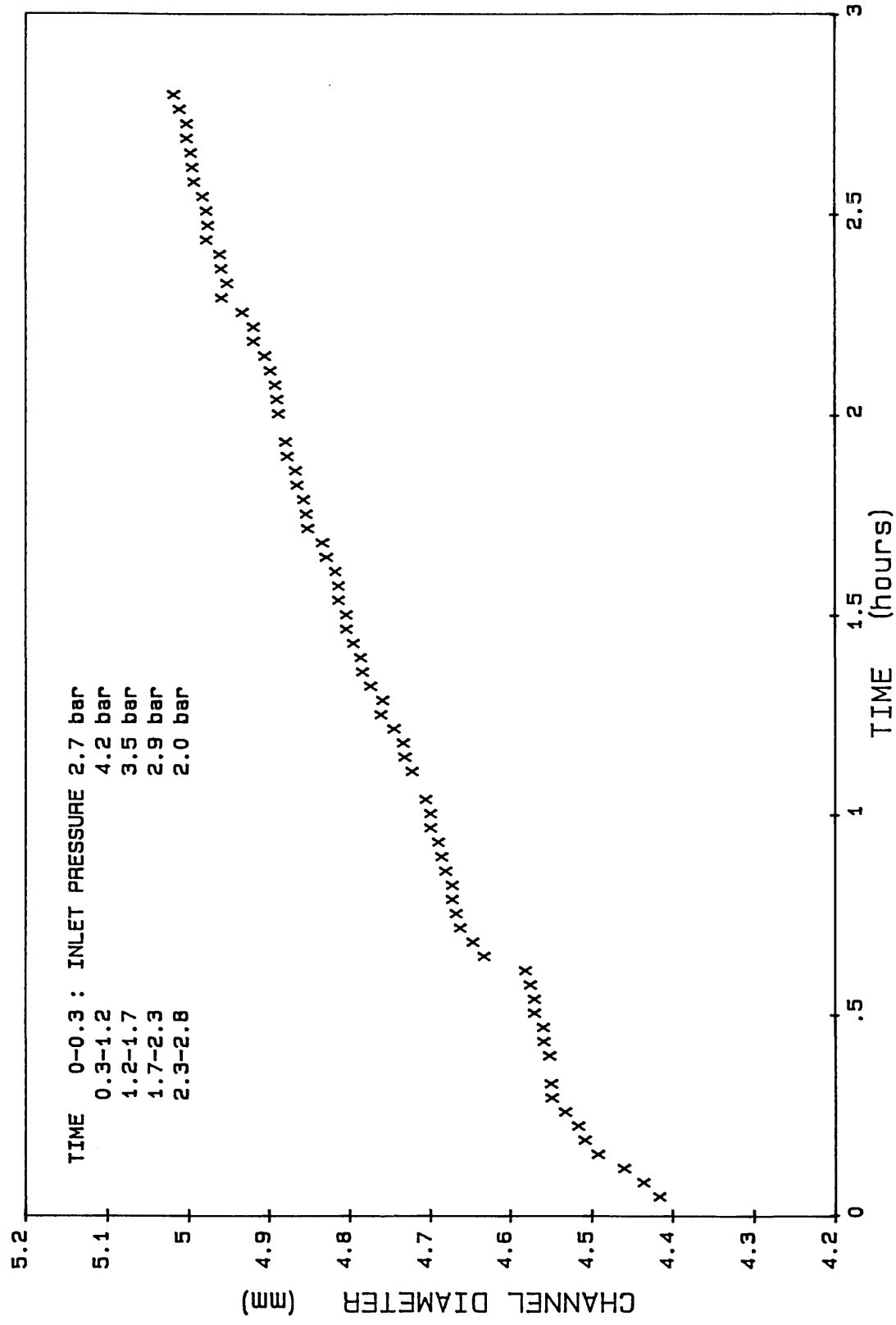
These two pieces of evidence suggest that a certain permeate velocity is required to hold the cake firmly to the membrane surface; however, once that is exceeded, normal forces acting on particles in the cake do not seem to influence resuspension. At low pressures, planes of weakness appear to be sited at the interface between cake and membrane.

(iv) Particle size

When tests were carried out with the 0.55 micron particles, no resuspension was noted up to flows of $9dm^3min^{-1}$ or pressures down to 0.1 bar . Following the arguments about cake expansion given at the end of section (ii) this is not a surprising result, because the axial drag force on a particle varies with the square of its radius, and the specific cake resistance with the inverse of radius squared. These effects imply that the crossflow required to cause cake expansion and re-entrainment with small particles must be greatly increased from the value appropriate to large particles. In effect, interparticle forces exceed drag forces with decreasing particle diameter. This is further illustrated by the fact that backwashing cake from the membrane was much more difficult with smaller particles.

FIGURE 5.16

RESUSPENSION : EFFECT OF OPERATING PRESSURE



## 5.3 Dynamic Filtration

### 5.3.1 Cake growth on a clean membrane

The transient approach to filtration equilibrium is outlined in this section. The main aim of this part of the work programme was to determine the influence of operating parameters such as crossflow, pressure and particle diameter on the variation of sticking factor defined by equation 3.18. This sticking factor is the fraction of particles convected to the membrane which become incorporated into the filter cake.

For a series of runs at different crossflows, the permeate flowrate - time loci are illustrated in figure 5.17. These data are for a Ceraver 0.1 micron membrane filtering large particles. The enhanced permeate flux at higher crossflow is seen. Assuming that the decline in permeate flowrate is entirely due to the build-up of filter cake, the cake mass can be obtained as a function of permeate flowrate using equation 3.22. Once cake mass is plotted against time, the cake growth rate can be estimated graphically. Equation 3.18 can then be used to obtain the sticking factor as a function of time. An example of this calculation is given in appendix D. Four main cases were studied experimentally: the combinations of both Carbosep and Ceraver 0.1 micron membranes with small and large particles. The main variable in each case was crossflow, although a limited study of pressure effects was undertaken using Carbosep membranes with small particles. Figures 5.18 to 5.21 show the variation of sticking factor with time for each test series.

So far, although the idea of a frictional force balance has been used to explain steady state filtration, the concept must also apply during cake growth. In general , due to cake build-up, permeate velocity decreases and shear stress increases with time. The normal and axial hydrodynamic forces follow the same pattern. Each particle on a particular approach path to the cake surface must have a sticking factor of either 0 or 1; however, when all approaches and geometries are averaged over the surface, the overall sticking factor may take an intermediate value. This average value depends on the

FIGURE 5.17

PERMEATE FLOWRATE vs. TIME : EFFECT OF CROSSFLOW

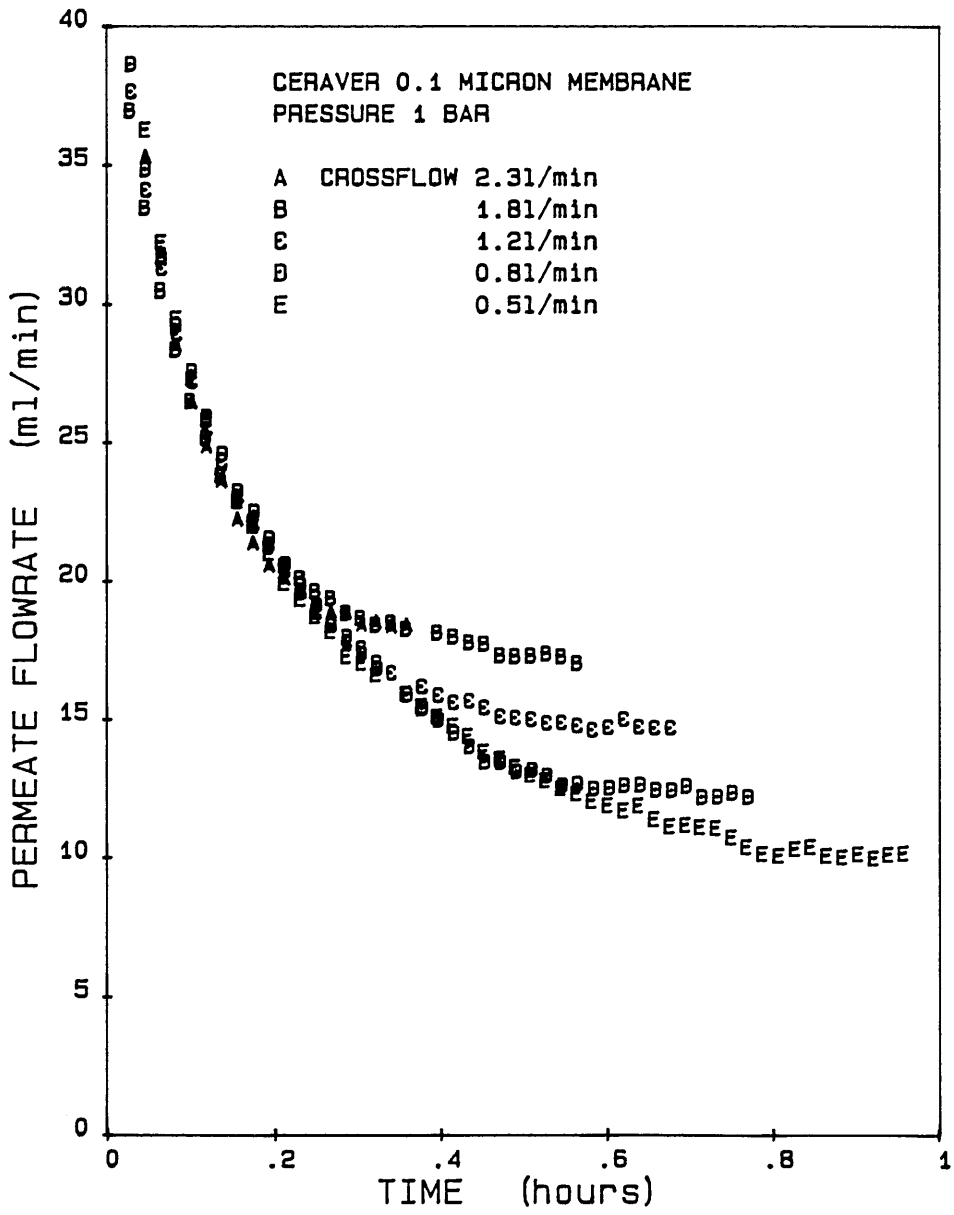


FIGURE 5.18

STICKING FACTOR vs. TIME : CARBOSEP TUBE & SMALL PARTICLES

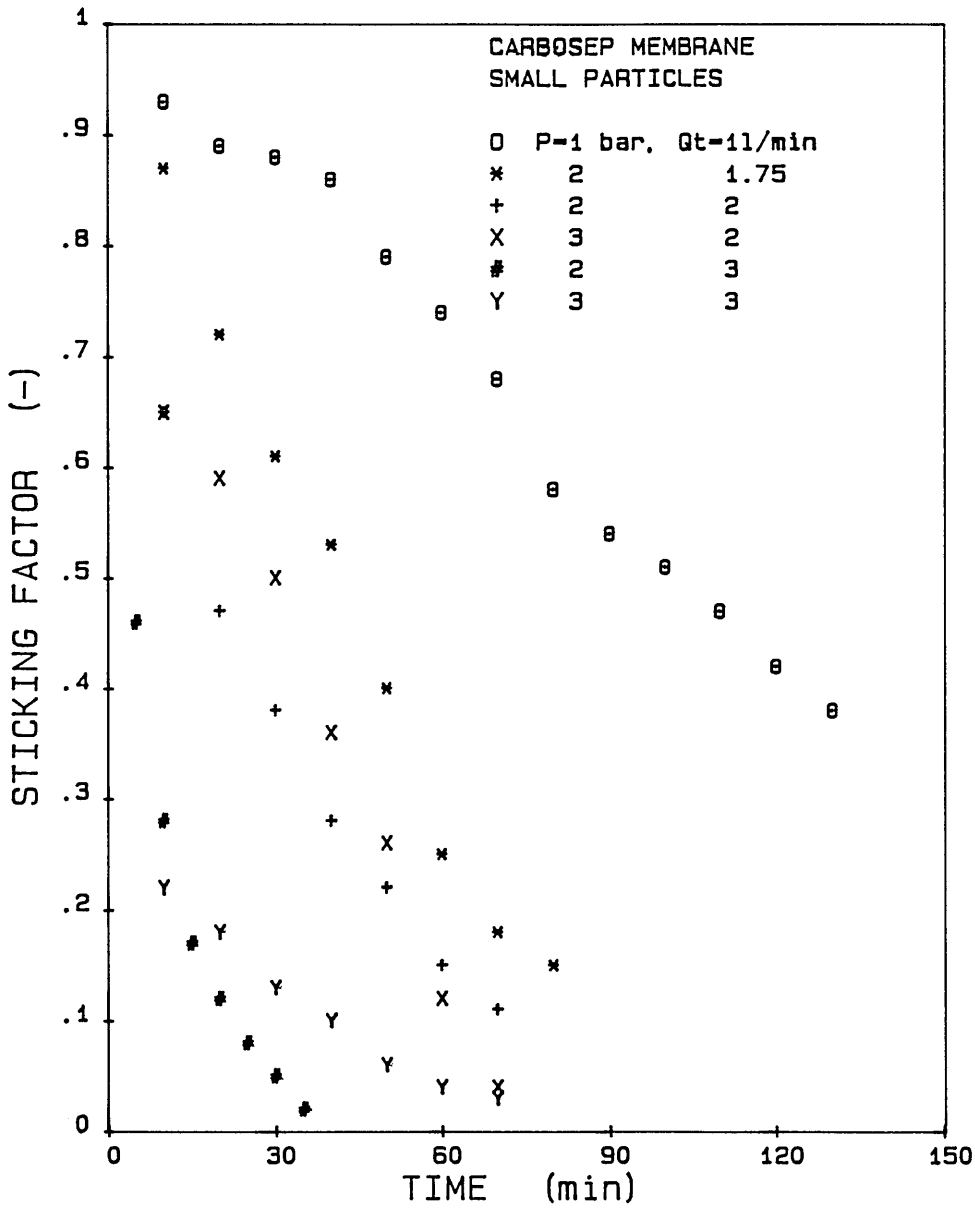


FIGURE 5.19

STICKING FACTOR vs. TIME : CARBOSEP TUBE & LARGE PARTICLES

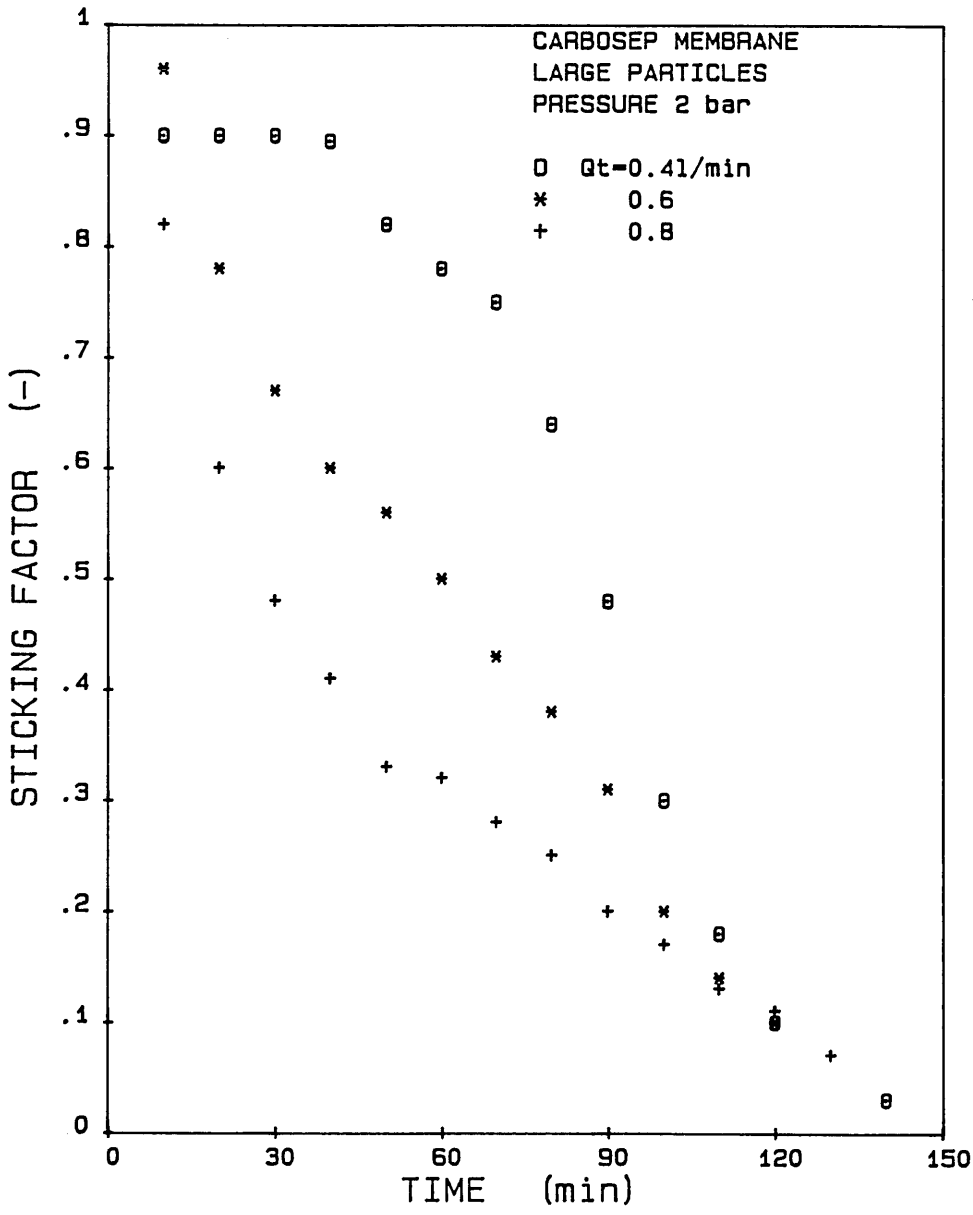


FIGURE 5.20

STICKING FACTOR vs. TIME : CERAVER TUBE & SMALL PARTICLES

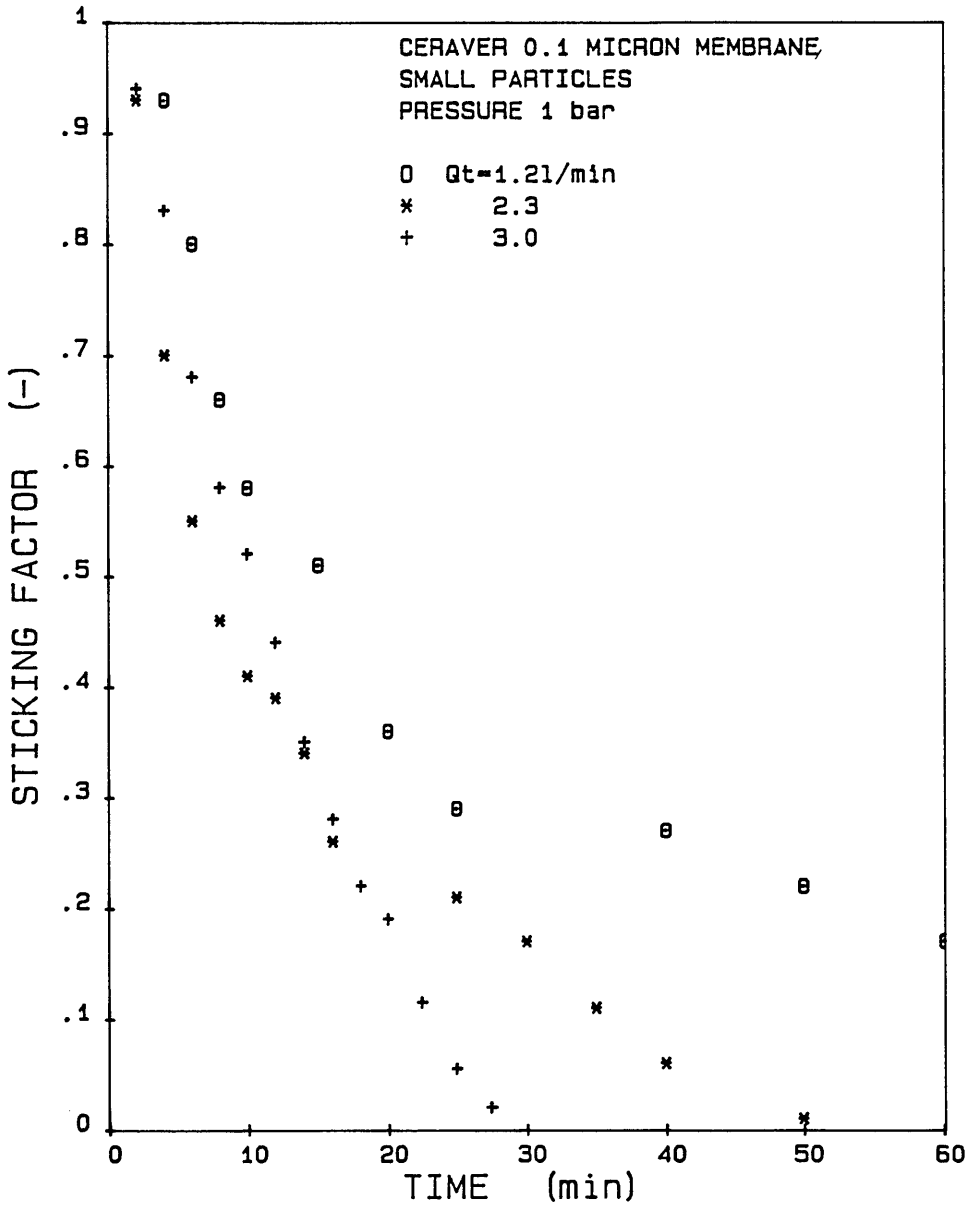
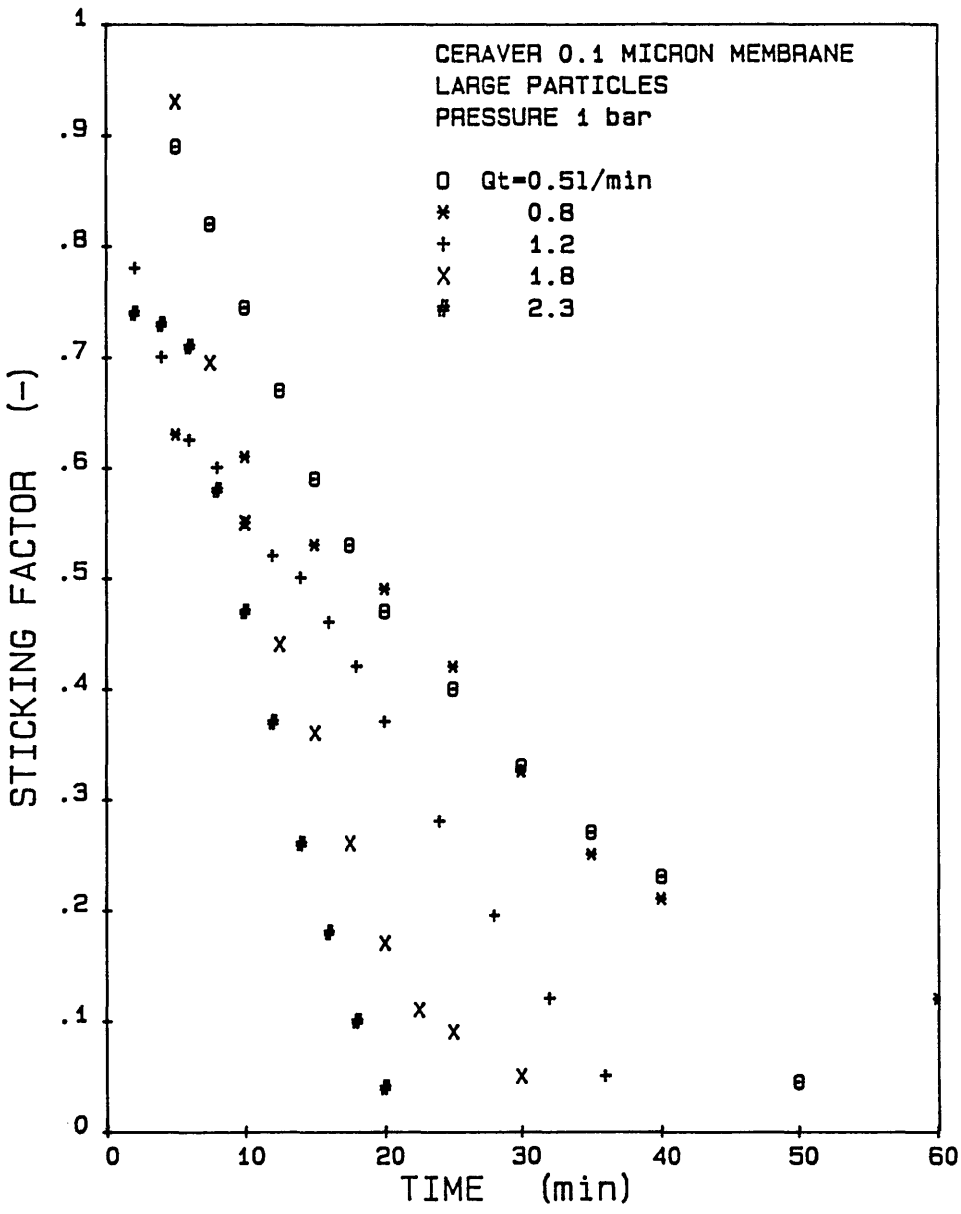


FIGURE 5.21

STICKING FACTOR vs. TIME : CERAVER TUBE & LARGE PARTICLES



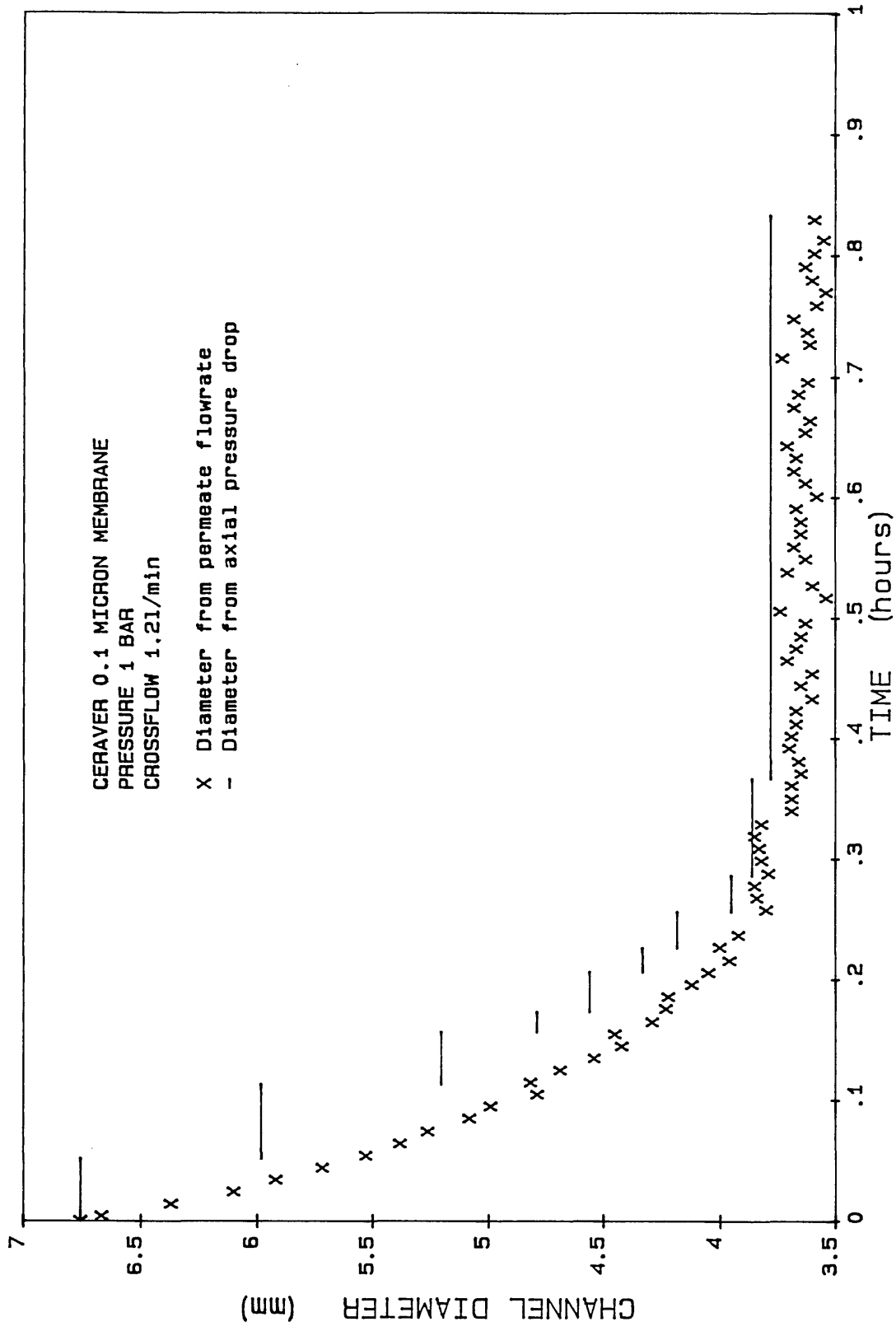
mean magnitude of axial and normal drag forces. Thus, as the balance of hydrodynamic forces changes during filtration, so does the sticking factor.

To demonstrate this, the natural method would be to plot sticking factor as a function of permeate velocity and shear stress. Unfortunately, both sticking factor and permeate velocity are evaluated from the permeate flowrate, rendering such a demonstration plot invalid due to interdependency of the axes. While figures 5.18 - 5.21 do not explicitly show the relation of sticking factor with the hydrodynamic forces, it is demonstrated that the sticking factor must be dependent on them. At lower crossflows ( lower shear stress ) each graph shows $\alpha$ to have higher values than at high crossflow. A simple approach to dynamic filtration, which defines the sticking factor to be unity until the critical $v - \tau$ value is reached, is shown to be inadequate.

There are slight inaccuracies in the calculated values of sticking factor which arise from pore blocking effects. In order to calculate the sticking factor, a value for specific cake resistance must be used in equation 3.22. It has previously been explained that $r_c$ appears to be a function of cake thickness due to pore blocking. However, the value of $r_c$ can only be determined at the end of a run, not during cake build-up. During cake growth, the value of specific resistance ( derived from the steady state permeate flow ) appears to be an underestimate. Therefore all values of channel diameter, cake mass or sticking factor calculated using that value of $r_c$ are also in error. To assess the magnitude of this inaccuracy during an experiment, the channel diameter derived from equations 3.19 and 3.20 ( using the erroneous value of $r_c$ ) can be compared to the actual channel diameter obtained from axial pressure drop measurements. These two estimated diameters are compared in figure 5.22, which shows that although the channel diameter calculated from permeate flow is an underestimate, the discrepancy with the true value is not large. This suggests that while the calculated values of sticking factor are not completely accurate, the systematic error is small. In these dynamic experiments, pressure drop measurements were not used to estimate channel diameter due to the discontinous function

FIGURE 5.22

COMPARISON OF CHANNEL DIAMETER : MEASURED AND CALCULATED VALUES



produced. Each bar on figure 5.22 represents an increase of 0.01 bar in axial pressure drop.

In the formulation of the deposition model ( equation 3.18 ) the use of bulk ( rather than wall ) concentration is proposed for the calculation of convective mass flux at the membrane surface. If a static cake is formed on the membrane, some of the filtration models ( such as axial convection or SIHD ) require the solids concentration adjacent to the wall to be fixed at a uniformly high value. When operating in turbulent flow, it may be argued that the whole fluid is well mixed. Plates 3.1 and 3.2 show the turbulent nature of the boundary layer without the added complications of wall porosity or suspended particles. The bulk concentration most often used in these experiments was 0.5wt% solids. In one experiment, this was halved to 0.24wt% and the decline of permeate flowrate was compared to a similar experiment, but with a bulk concentration of 0.52wt% . Figure 5.23 shows this comparison. The time to reach equilibrium was in proportion to the bulk concentration: 29 minutes at 0.24% and 16 minutes at 0.52% . This provides good support for the argument that it is the bulk concentration, not some fixed wall value, that should be used in the cake growth model. On this basis, the well-mixed assumption seems justified.

### 5.3.2 Re-establishment of equilibrium

Once steady state was reached, lowering the crossflow or raising the pressure produced a further decline in performance as more matter was deposited. Equilibrium was re-established when the critical values of permeate velocity and shear stress were regained. This is illustrated in figure 5.24, for operation with a 0.1 micron Ceraver membrane and variation of crossflow.

The point of greatest interest from figure 5.24 is the time taken to re-establish equilibrium. If diffusional processes played any part in mass transfer, the new equilibrium would be reached very quickly. Frictional arguments suggest that at a slight displacement from equilibrium, the sticking factor would still be close to zero;

FIGURE 5.23

CONCENTRATION EFFECT ON DYNAMIC PERMEATE FLOWRATE

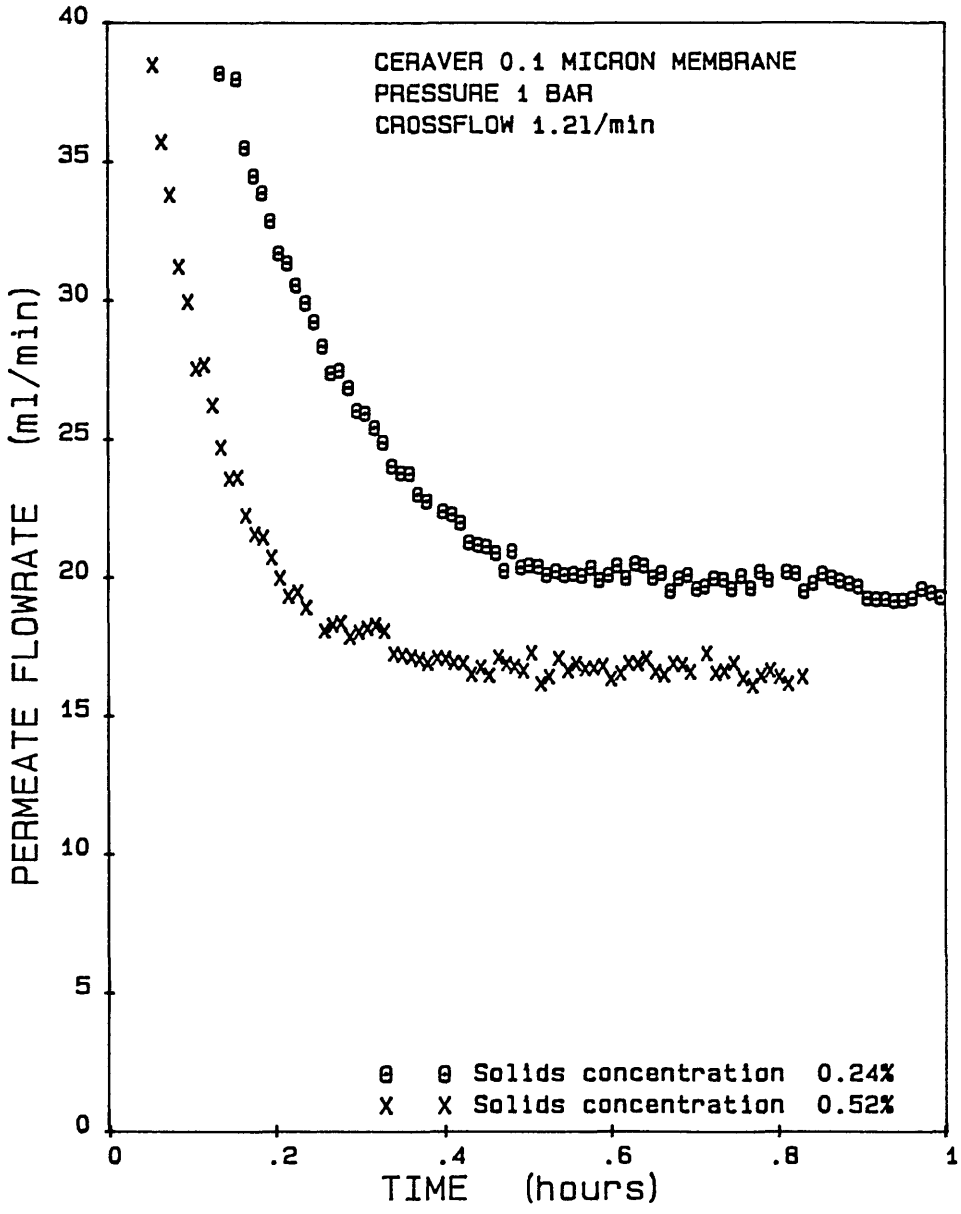
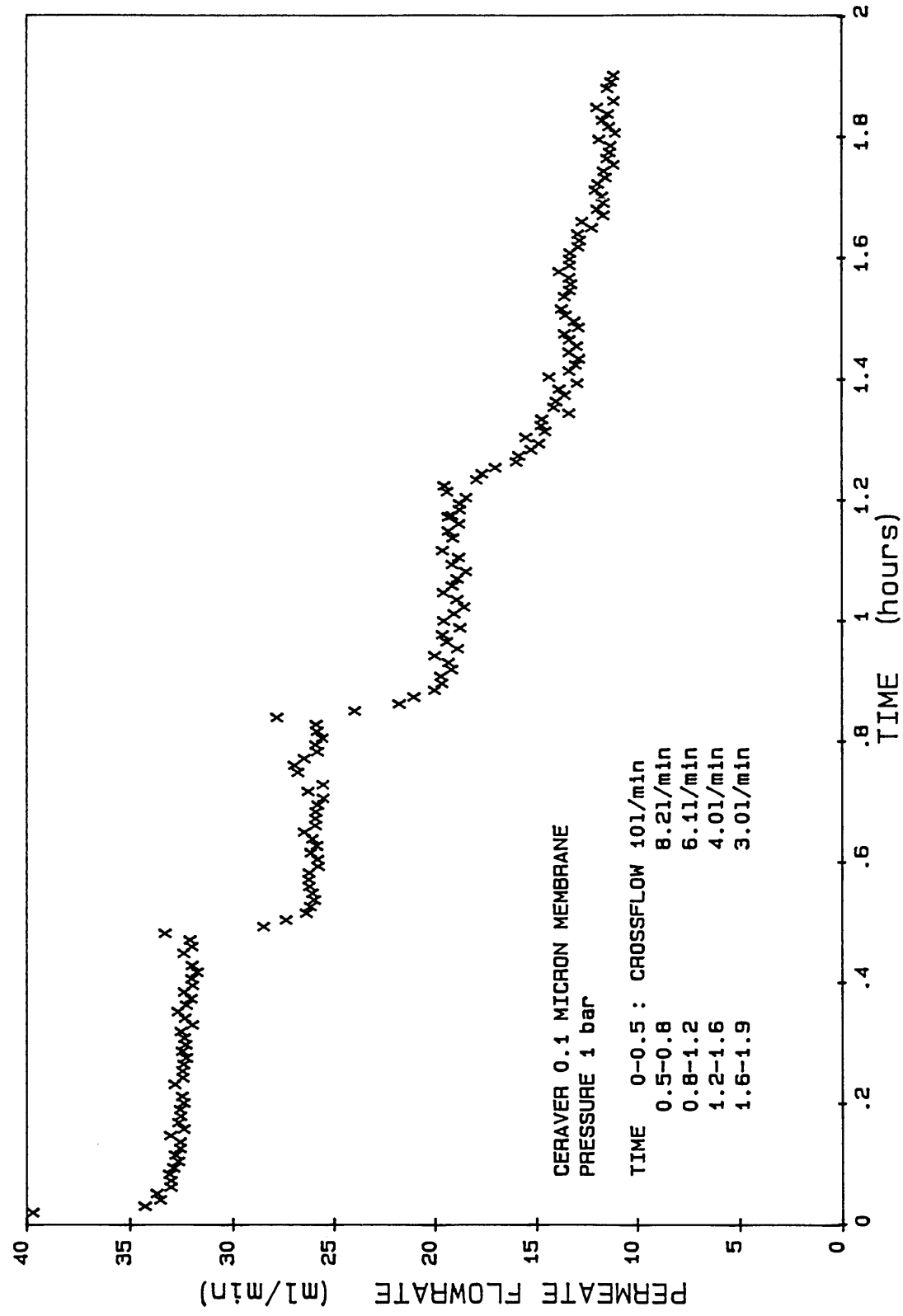


FIGURE 5.24

RE-ESTABLISHMENT OF EQUILIBRIUM WITH CHANGED CROSSFLOW



thus the additional mass required for a new steady state deposits at a low rate. This longer timescale is observed in figure 5.24, further reinforcing the friction model over diffusional arguments.

## 5.4 Summary

Experimental evidence presented in this chapter strongly supports the concept of filtration equilibrium being determined by a force balance on a particle at the cake surface. The permeate velocity - shear stress data show appropriate linearity and particle size dependency to confirm the model. Alternative models discussed in chapter 2 are not supported by the data; primarily due to their implied mathematical form of the $v - \tau$ relationship, but also because some models are based on a reversible mass-transport equilibrium, which was not observed in this study.

The original frictional force model, outlined in most detail by Rautenbach and Schock [46] has been shown to be limited in scope as only hydrodynamic forces were considered in the frictional balance. In this thesis, interparticle forces were shown to be important as the filter cake was not easily resuspended and a predicted intercept in the $v - \tau$ relationship was observed for some systems.

Extrapolation of the steady state frictional equilibrium to the dynamic case ( proposed in chapter 3 ) was validated. This suggested that only a certain fraction of mass convected to the membrane was incorporated into the cake. The sticking factor was found to decrease throughout an experiment from 1 to 0 as the axial drag force on particles grew larger with respect to permeate drag and interparticle forces.

# CHAPTER 6

## PREDICTION OF STEADY STATE FILTRATION

Solution of the porous media equations coupled with the frictional equilibrium condition is described in this chapter. The effect of crossflow, pressure and particle size on the steady state cake thickness and permeate flowrate are examined and compared to experimental data where appropriate. Discussion of the results and applicability of the model concludes the chapter.

### 6.1 Basis of Solution

Having demonstrated the validity of the frictional model for steady state filtration performance, it may now be used to generate performance data over a wide range of operating conditions with a minimum of empiricism. In addition to the hydrodynamic characteristics of the filtration system, the only information that needs to be determined before using the model is the locus of the equilibrium $v - \tau$ line. This information can be obtained from a small number of tests.

The most sensible parameters to gauge filtration performance are permeate flowrate per unit length of membrane tube and channel diameter. The first is of obvious importance to the design of a filtration process, while a knowledge of channel diameter allows calculation of the axial pressure drop.

In the following analysis, it was assumed that the $v - \tau$ line does not have an intercept, though the method of solution would be the same if that were not true. Eliminating the wall pressure from equations 3.20 and 3.21 gives the permeate flowrate per unit length of membrane tube

$$\frac{Q_p}{L} = \frac{\Pi P_b}{\mu_o (k_1 + k_2 \ln(d_o/d_f))} \qquad (6.1)$$

where $P_b$ is the bulk pressure, $d_o$ and $d_f$ are the membrane and channel diameters. The k coefficients are given by

$$k_1 = R_m / d_o \tag{6.2}$$

$$k_2 = r_c / 2 \tag{6.3}$$

$R_m$ is the hydraulic membrane resistance and $r_c$ the specific cake resistance. The permeate velocity at the wall is obtained by dividing equation 6.1 by $\Pi d_f$. In cylindrical geometry, the wall shear stress is given by the standard equation

$$\tau = \frac{8 f \sigma_f Q_t^2}{\Pi^2 d_f^4} \tag{6.4}$$

where f is the Fanning friction factor, $\sigma_f$ is the fluid density and $Q_t$ is the volumetric flowrate. The frictional equilibrium is expressed ( cf equation 3.17 using $k_0 = 0$ )

$$\frac{v_{w-}}{\tau} = k_{eq1} \tag{6.5}$$

where $k_{eq1}$ is dependent on particle diameter as follows

$$k_{eq1} = k_{eq2}\, d_p \tag{6.6}$$

$k_{eq1}$ and $k_{eq2}$ are the equilibrium constants for filtration. Substituting the expressions for permeate velocity ( from a suitably modified version of equation 6.1 ) and shear stress ( from 6.4 ) into equation 6.5, the following expression for channel diameter can be solved iteratively

$$d_f^3 = k_3 (k_1 + k_2 \ln(d_o / d_f)) \tag{6.7}$$

where

$$k_3 = \frac{8 \sigma_f \mu_o f Q_t^2 k_{eq1}}{\Pi^2 P_b} \tag{6.8}$$

$k_1$ and $k_2$ are defined by equations 6.2 and 6.3 .

Using the resulting value of channel diameter in equation 6.1 allows calculation of the permeate flowrate per unit length of membrane.

The assumptions of this analysis are those adopted elsewhere in this work: that the filter cake has uniform properties and that pore blocking is not appreciable ( or has been accounted for in specification of $R_m$ and $r_c$ ).

## 6.2 Example Predictions

In this section, the results from solution of the above system of equations are presented. The values of inputs to the model sometimes coincide with experimental operating conditions, but are often extrapolated beyond the range tested. In order to illustrate the predictions with data, the membrane characteristics used in these solutions were those listed in section 4.2, although generality of solution was maintained by calculating $r_c$ using the Carmen-Kozeny equation with a voidage of 0.36. The properties of water at 20°C were used, as were the experimentally-determined friction factors of 0.0061 and 0.0058 for Ceraver and Carbosep membranes. From figure 5.4, the implied values of $k_{eq2}$ are 14 and 5$kg^{-1}m$ s for the large and small particles.

The effects of crossflow, pressure and particle diameter on channel diameter and permeate flowrate per unit length were determined. Standard conditions adopted in all the calculations were P = 2 bar & $Q_t$ = 0.6$dm^3min^{-1}$ for Carbosep and P = 1 bar & $Q_t$ = 2$dm^3min^{-1}$ for Ceraver membranes.

Figures 6.1 to 6.12 show the performance predictions when cake is deposited on both Carbosep and Ceraver 0.1 micron membranes. Experimental data has been included where applicable. The trends are discussed in the next section.

FIGURE 6.1

CHANNEL DIAMETER vs. CROSSFLOW ( CARBOSEP TUBE )

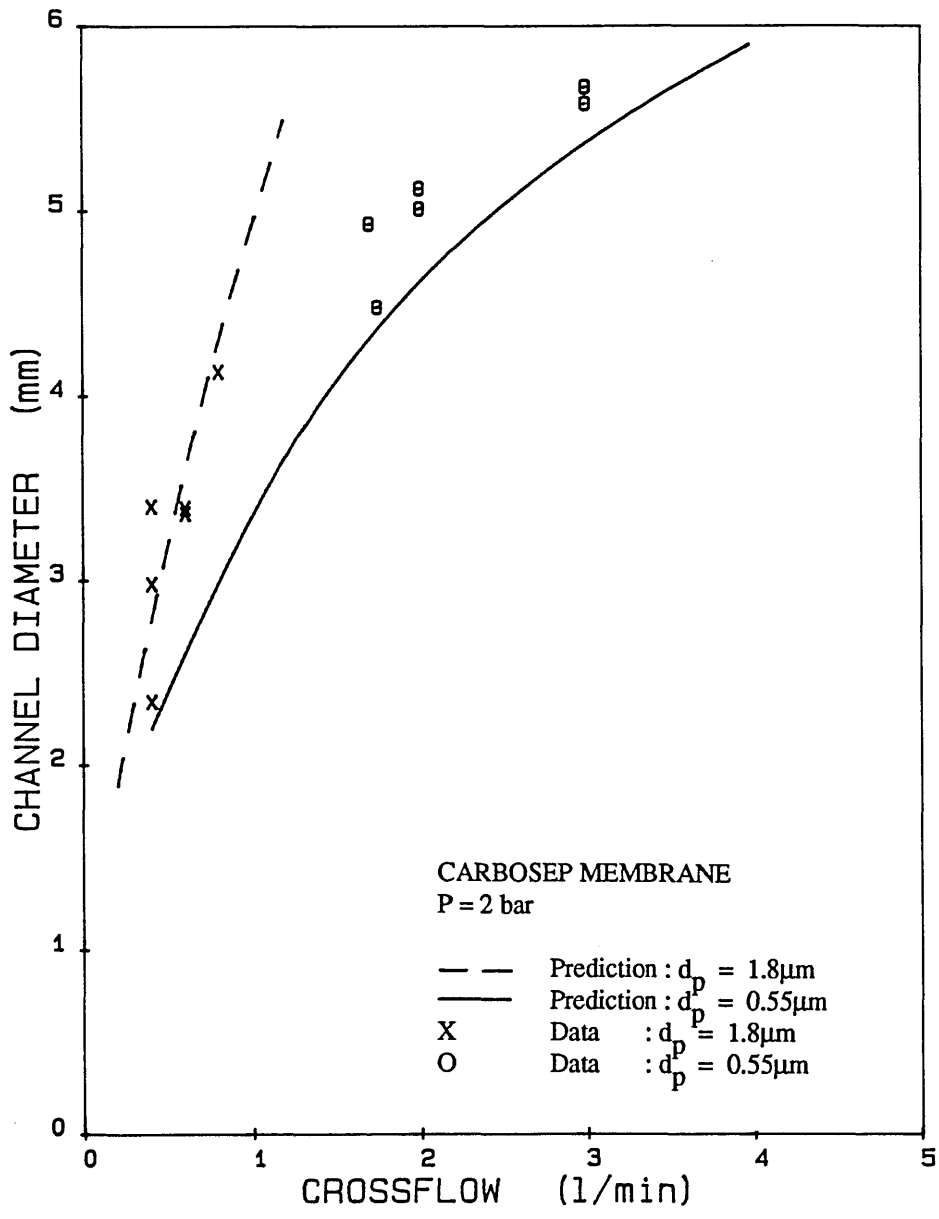


FIGURE 6.2

CHANNEL DIAMETER vs. PRESSURE ( CARBOSEP TUBE )

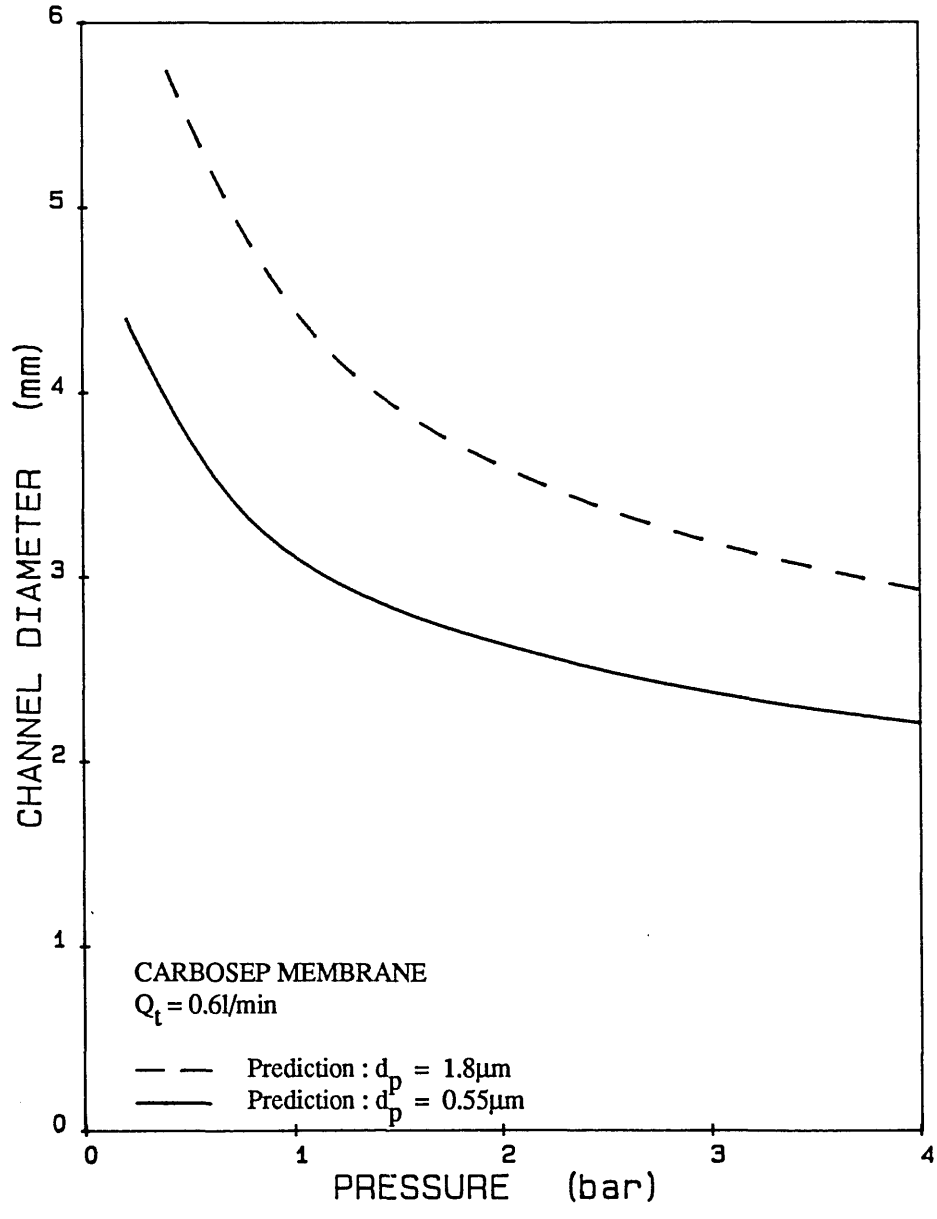


FIGURE 6.3

CHANNEL DIAMETER vs. PARTICLE DIAMETER ( CARBOSEP TUBE )

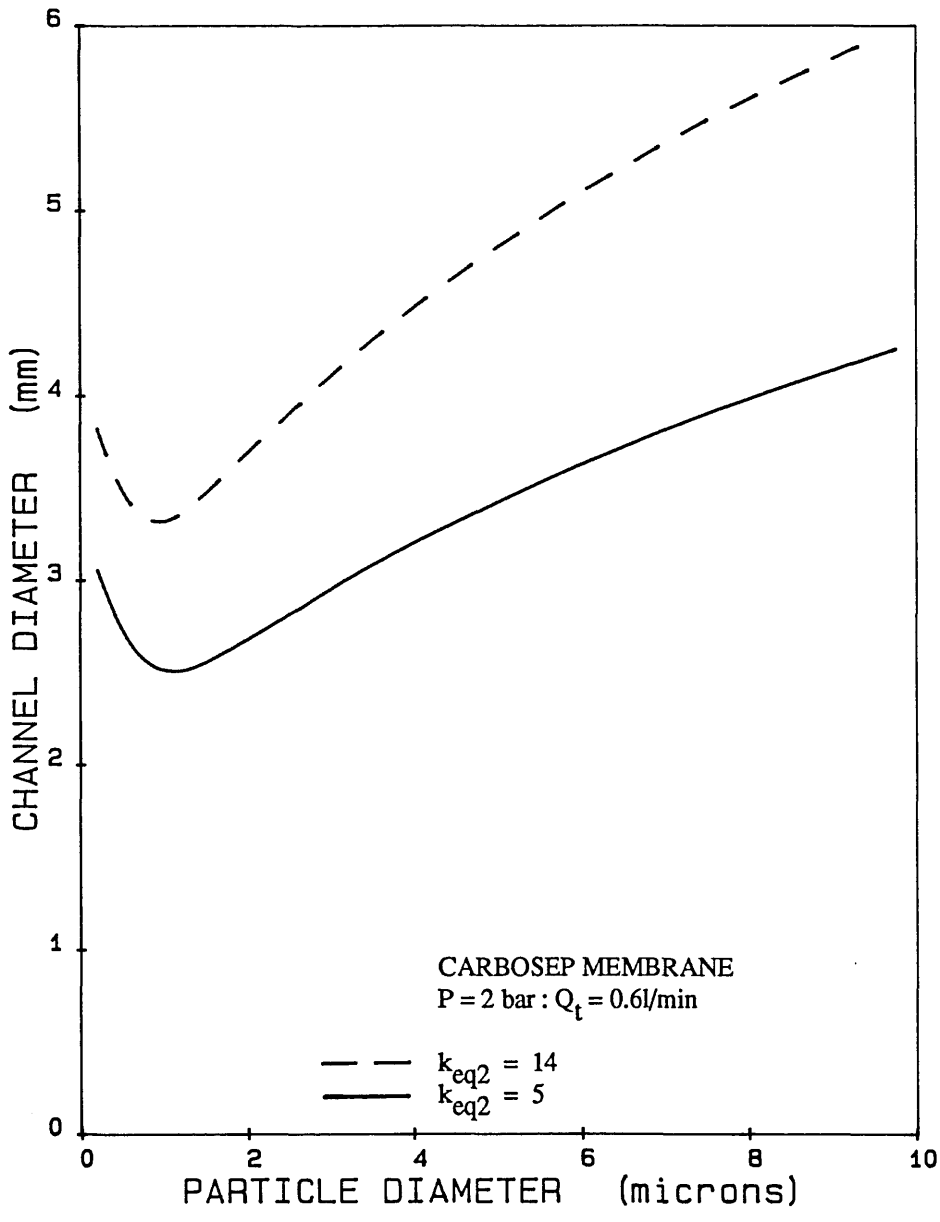


FIGURE 6.4

PERMEATE FLOW / LENGTH vs. CROSSFLOW ( CARBOSEP TUBE )

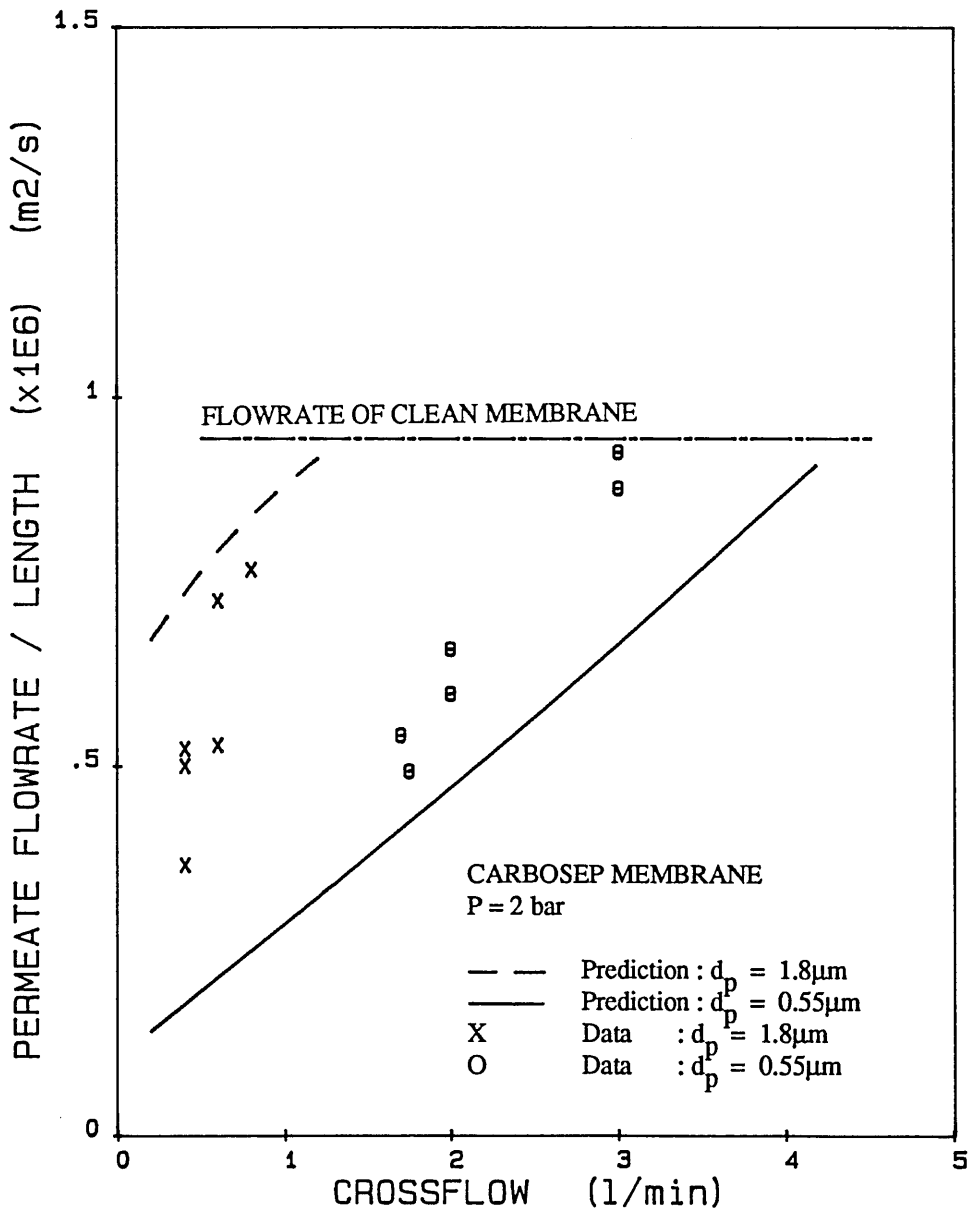


FIGURE 6.5

PERMEATE FLOW / LENGTH vs. PRESSURE ( CARBOSEP TUBE )

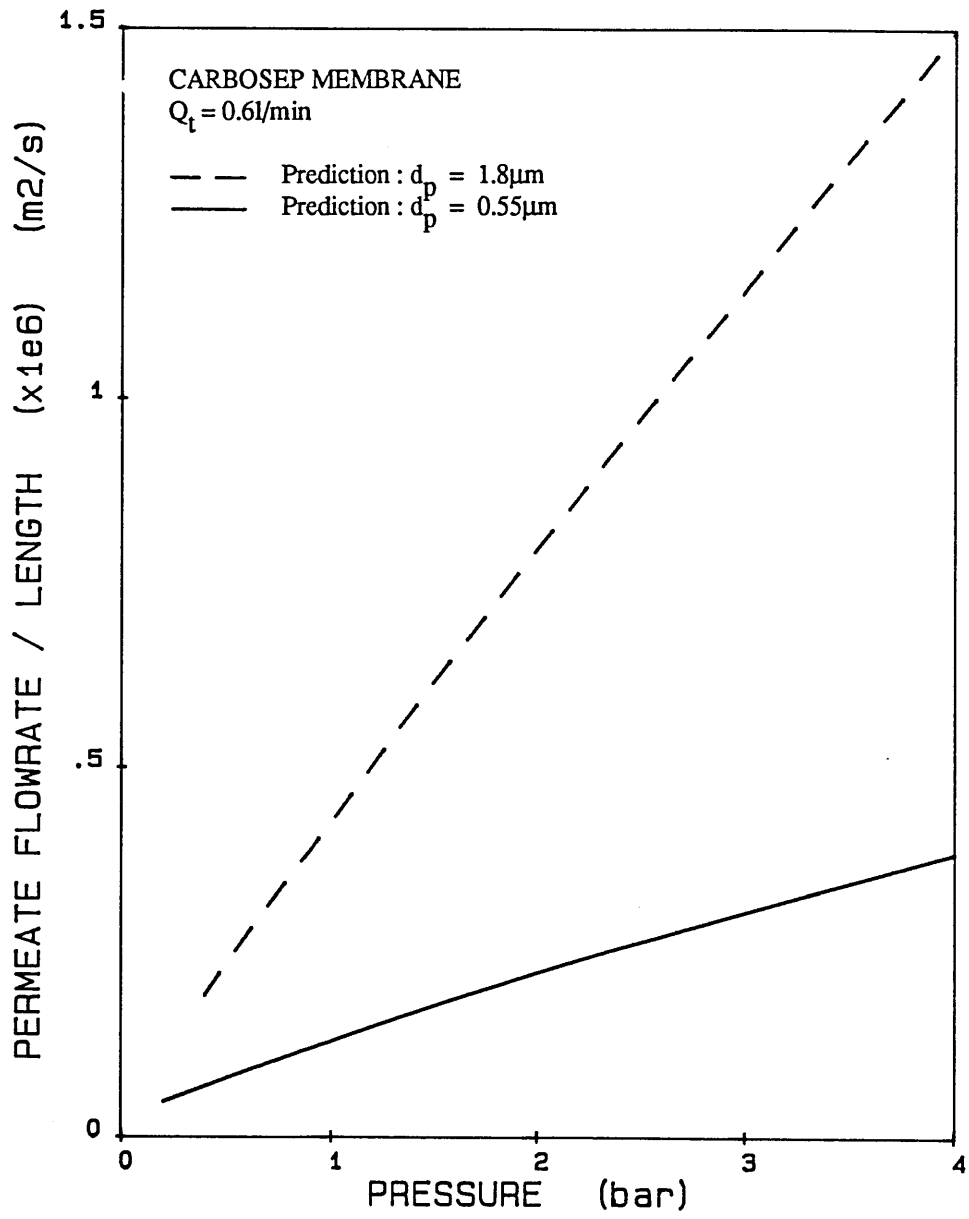


FIGURE 6.6

PERMEATE FLOW / LENGTH vs. PARTICLE DIAMETER ( CARBOSEP TUBE )

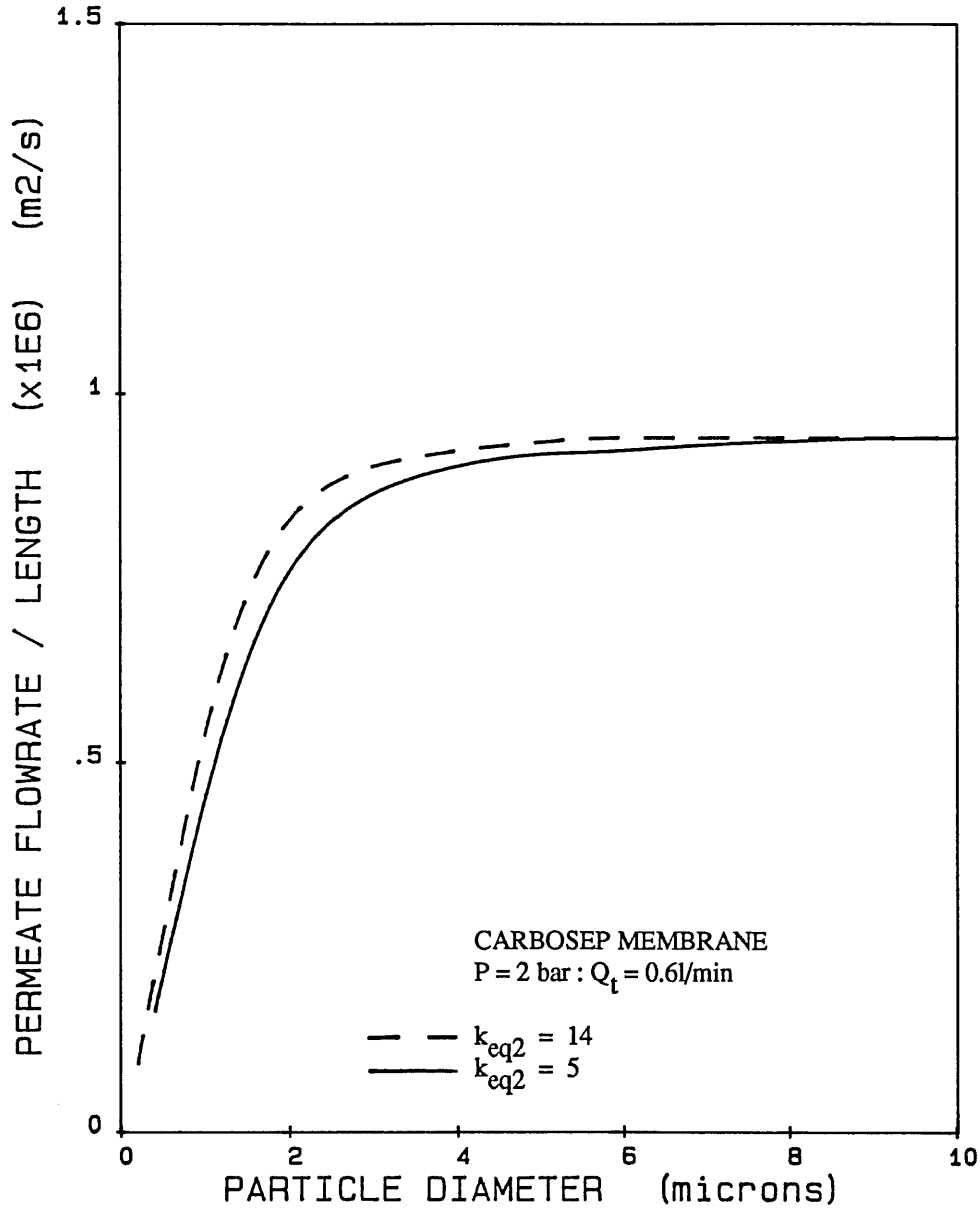


FIGURE 6.7

CHANNEL DIAMETER vs. CROSSFLOW ( CERAVER TUBE )

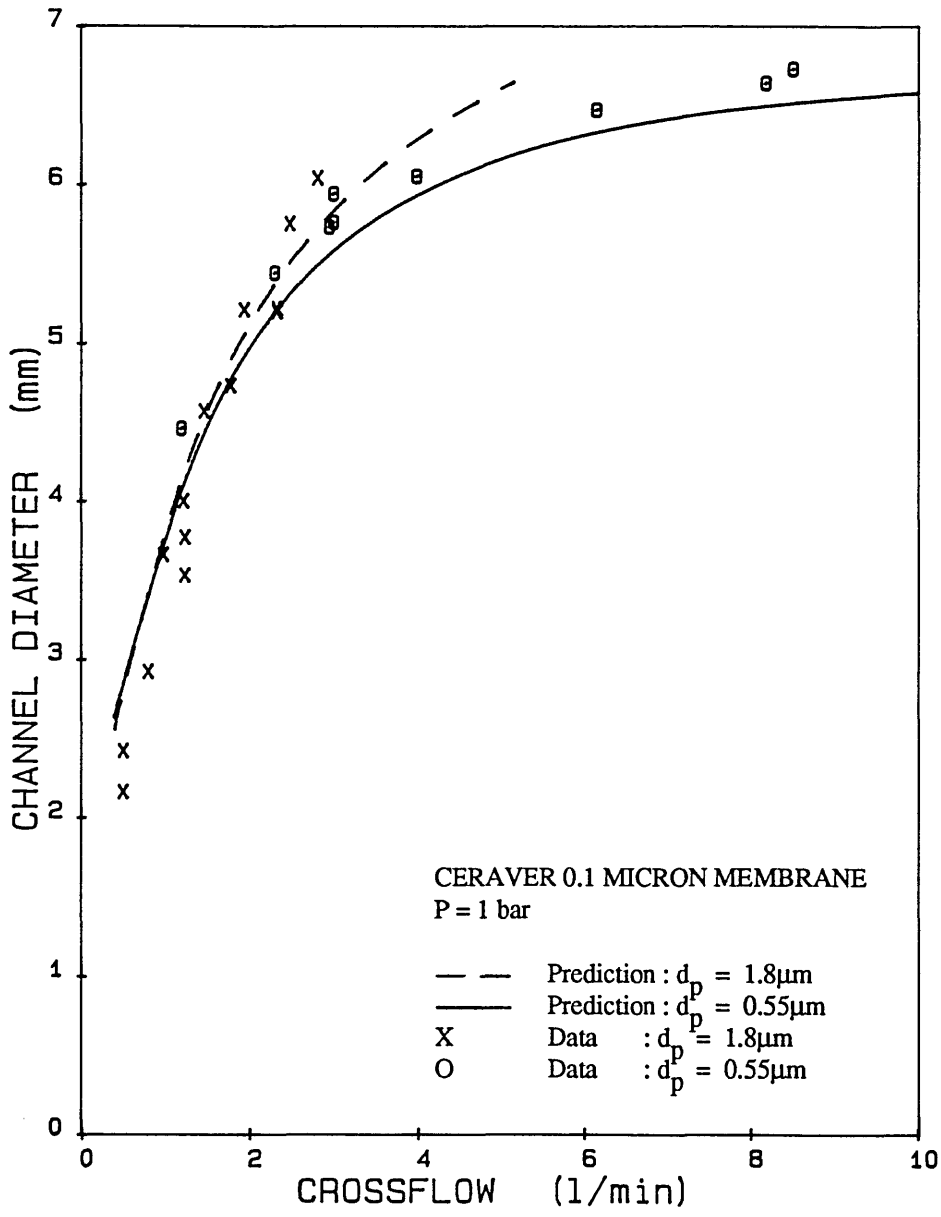


FIGURE 6.8

CHANNEL DIAMETER vs. PRESSURE ( CERAVER TUBE )

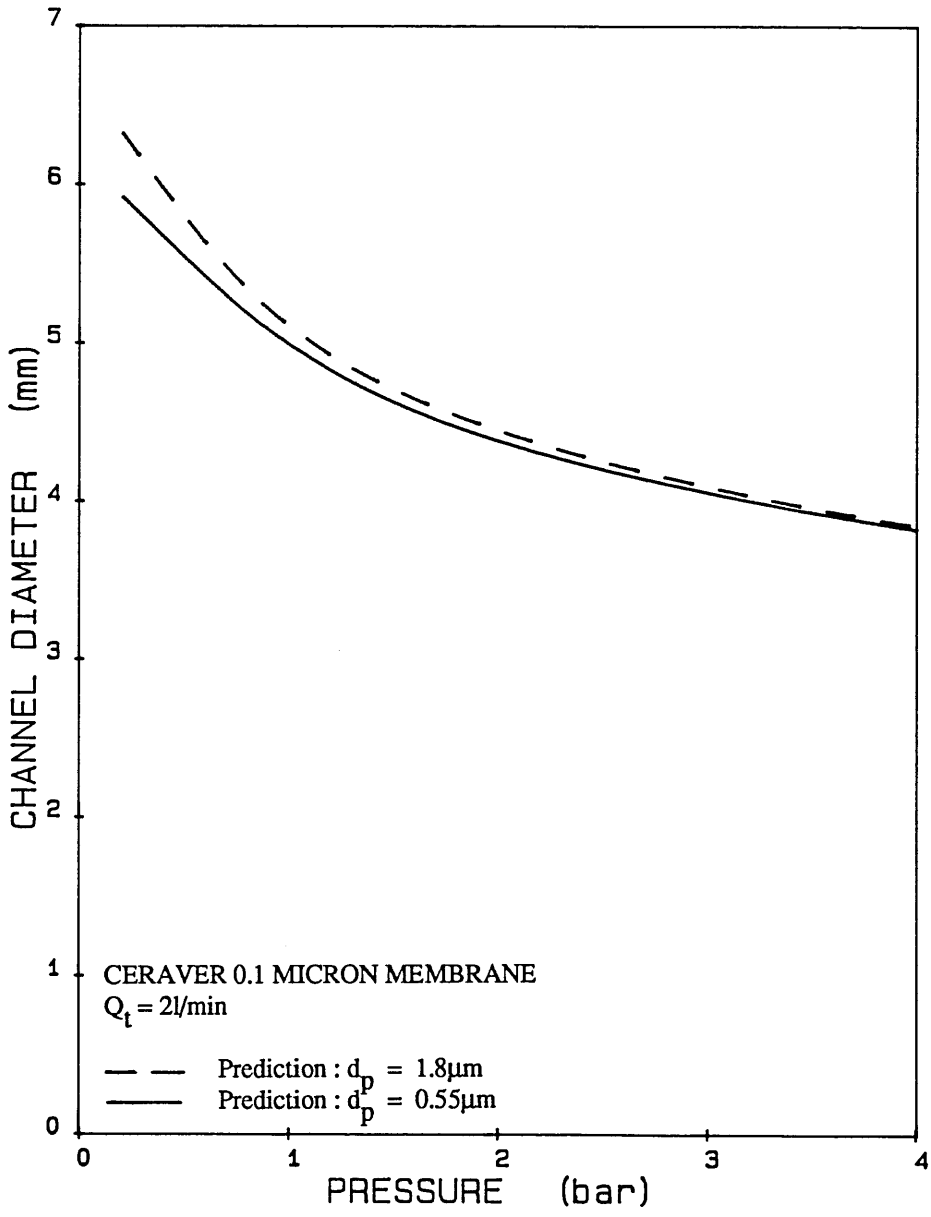


FIGURE 6.9

CHANNEL DIAMETER vs. PARTICLE DIAMETER ( CERAVER TUBE )

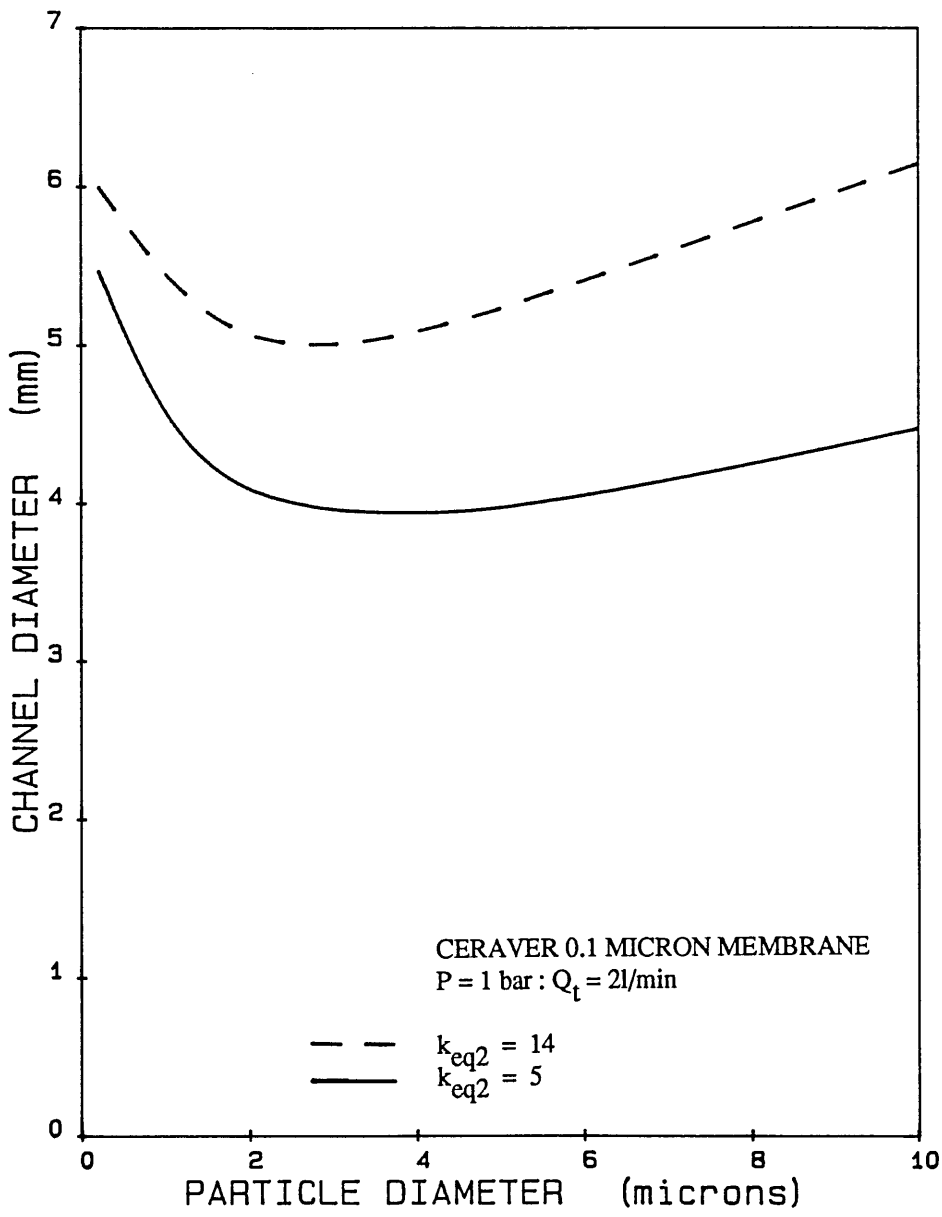


FIGURE 6.10

PERMEATE FLOW / LENGTH vs. CROSSFLOW ( CERAVER TUBE )

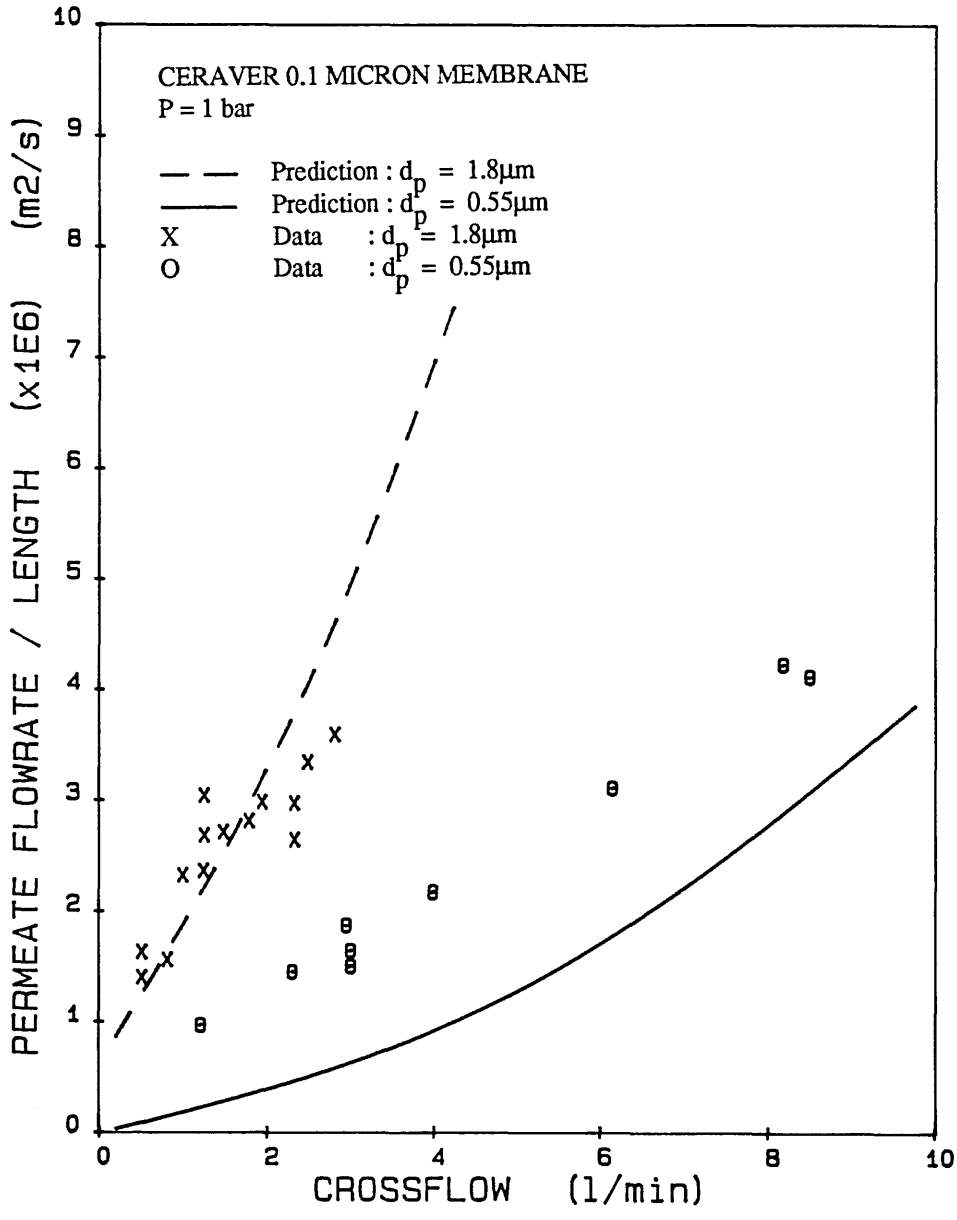


FIGURE 6.11

PERMEATE FLOW / LENGTH vs. PRESSURE ( CERAVER TUBE )

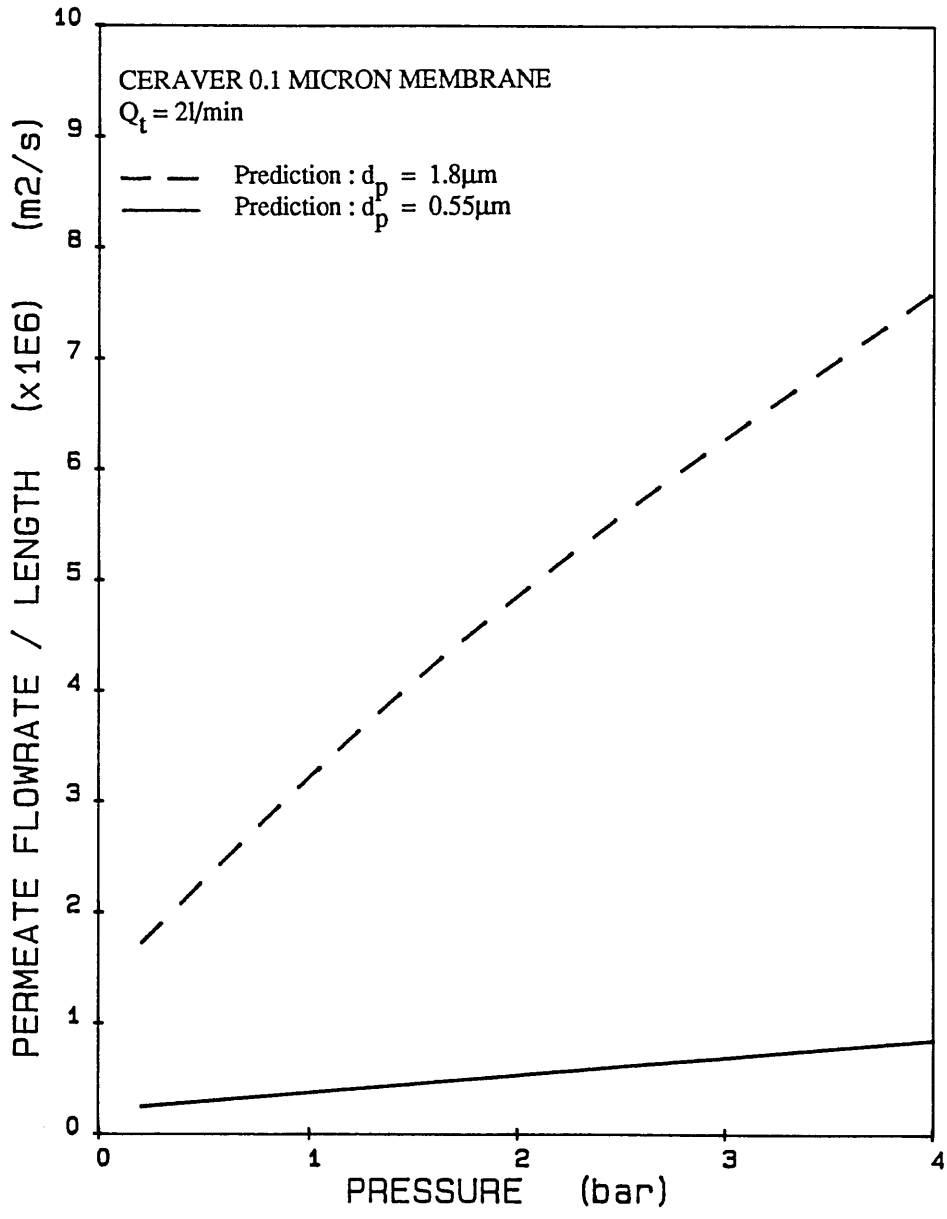
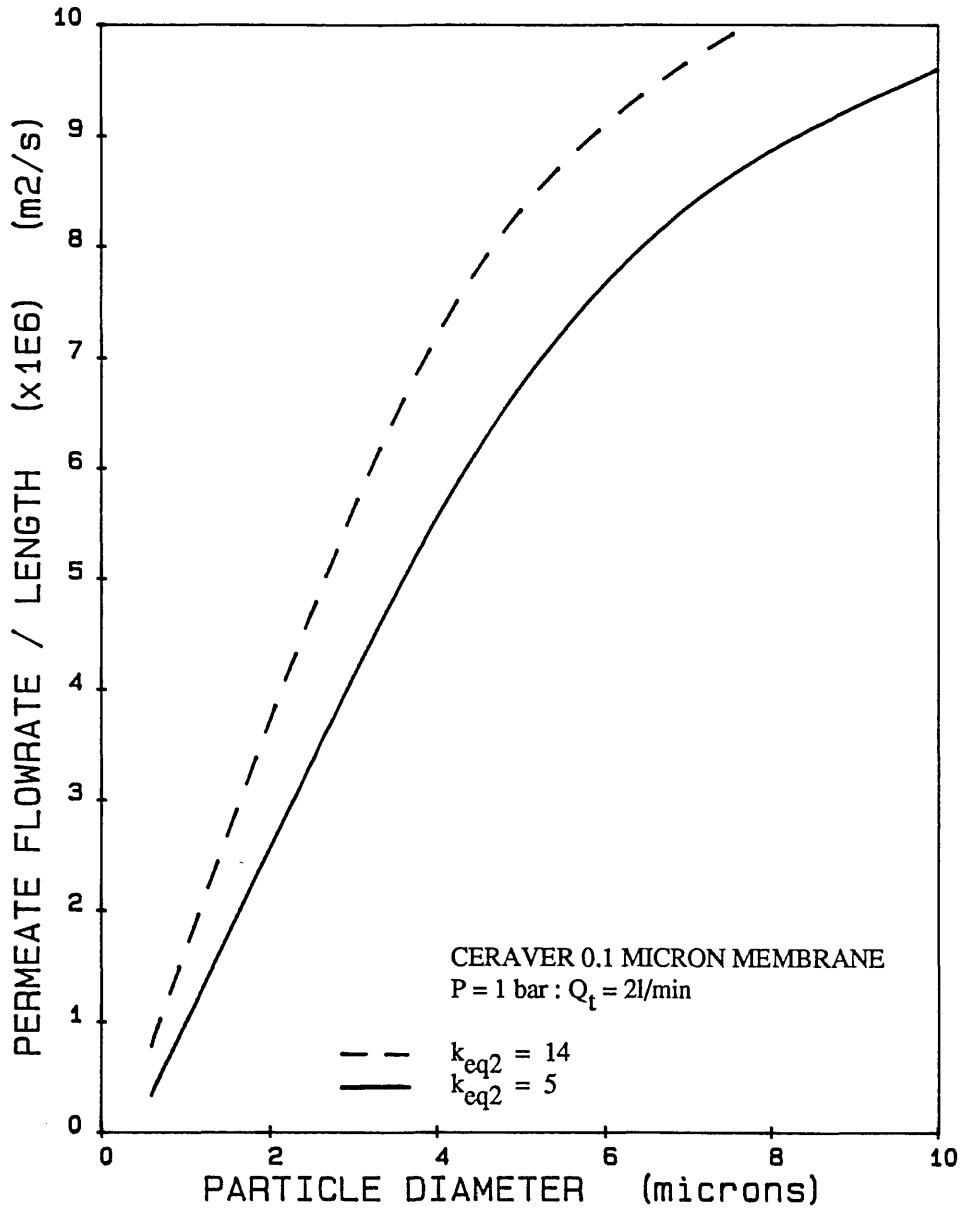


FIGURE 6.12

PERMEATE FLOW / LENGTH vs. PARTICLE DIAMETER ( CERAVER TUBE )



## 6.3 Discussion

Each of the four figures matching the model predictions to experimental data shows good agreement between theory and experiment, although this is to be expected as the values of $k_{eq2}$ were obtained from data. However, the predictions are not a complete re-working of experimental results: average values of membrane resistance were used and the specific cake resistance was calculated from the Carmen-Kozeny equation. In addition, the fact that the small particles filtered with a Ceraver tube exhibited an intercept on the permeate velocity - shear stress graph was not considered. This was in order to maintain consistency with the other three sets of predictions.

The assumptions listed above are manifest in the predictions. Figure 6.4 shows that the model does not appear to represent the data of the large particles very well, though reference to appendix C reveals that the cake and membrane resistances used in the calculations were not typical for these data. Similarly, figure 6.10 illustrates the effect of not accounting for the intercept in the $v - \tau$ data, as the predicted values for permeate flowrate are lower than the data.

The graphs showing the effect of particle size illustrate predictions made using the experimentally-determined parameter $k_{eq2}$. This was estimated to be $5 kg^{-1}$ m s in the case of the smaller particles and $14 kg^{-1}$ m s for the larger particles. Assuming a linear axial velocity profile, the frictional theory indicates that $k_{eq2}$ should be constant for a particular material. While use of different values seems to affect the predicted channel diameter, little effect on permeate flowrate is seen.

Application of this method to similar filtration systems is straightforward. In addition to the properties of the membrane, the friction factor, along with the cake resistance ( or voidage ) must be determined. Several tests must then be performed to estimate $k_{eq1}$ or $k_{eq2}$ from $v - \tau$ data. The fact that the equilibrium constants must be determined experimentally may be suggested as a weakness of the model because it introduces some empiricism. In fact, the reverse

is true because the parameter $k_{eql}$ combines several features of particle interactions, all of which are extremely difficult to determine independently. These features include the coefficient of friction and the magnitude of forces acting on a particle at a filter cake surface of unknown structure. While the functionalities of these forces are known, their magnitudes are specific to each system.

Two problems remain: treatment of non-spherical particles and polydisperse suspensions. Modelling the first case is rather easier than the second. The concept of a frictional force balance is as valid for non-spherical particles as for spherical: the experimental determination of $k_{eql}$ will reflect the particular balance of forces for each shape of particle, so the model can be used in the same manner. As with non-spherical particles, the force balance is valid for a polydisperse mixture; however, the assumption of constant filter cake properties will be violated as deposition occurs. When shear stress increases and permeate flow drops due to cake build-up, the larger particles in the suspension will be prevented from depositing. One suggestion for solution of the model in this case is to assume that all particles below the critical exclusion diameter are deposited in proportion to their occurrence in the bulk. Thus at any moment in time the distribution of depositing particles can be determined, which if coupled to the history of cake composition would enable calculation of the effective hydrodynamic cake properties by integration. Computer simulation would be needed for this application.

# CHAPTER 7

## CONCLUSIONS

1. Theoretical analyses for axial convection, shear-induced hydrodynamic diffusion and lift force models for crossflow filtration have shown the limited applicability of these approaches to filtration of micron-sized particles in turbulent flow. A new model based on a frictional balance of hydrodynamic and interparticle forces has been developed to predict steady state filtration performance.

2. The model was tested by filtration of spherical, monodisperse latex particles of 0.55 and 1.8 microns diameter in tubular, ceramic membranes. The form of the model suggests that the locus of steady state permeate velocity and shear stress should be a straight line. This feature was confirmed by experiment.

3. In addition to the linearity of the $v - \tau$ data, the slope of the equilibrium line it represents was found to be an increasing function of particle diameter. The theory suggests that these gradients should be in proportion to particle diameter. Two sizes of particle were tested. The results seemed to indicate that the slope varied as $d_p^{1.5}$, but with only two data sets, this relationship must be subject to some uncertainty.

4. The dependence of the equilibrium line locus particle diameter indicates that careful choice of initial operating conditions should enable separation of particles in a polydisperse mixture. Experiments using a bimodal particle distribution confirmed this phenomemon. During an experiment when the time dependent $v - \tau$ operating line crossed the equilibrium line for the larger particles, no more deposition of that particle species was observed. Other filtration theories predict a gradual, rather than sudden, cessation of large particle deposition.

5. When using the smaller particles with a highly permeable membrane, an apparent intercept in the $v - \tau$ data was found. The theoretical model suggests that interparticle forces are responsible for such a feature, although variation of one of these forces ( electrical repulsion ) did not produce a different intercept. Other frictional models reported in the literature have not taken account of this effect.

6. The main aim of the project was to develop a model which could predict the steady state performance of a crossflow filtration unit. Using an experimentally-determined equilibrium line, solution of the porous media equations for the cake and membrane allows such predictions to be made. Although the equilibrium line is empirical, only a small number of tests are required to establish its position. Attempts at theoretical calculation of the line are beset with problems, as accurate knowledge is required of several parameters, all difficult to estimate. Predictions for a wide range of possible operating conditions are in good agreement with experimental data, which confirms the usefulness of the model.

7. Despite the loss of performance due to filter cake growth on a membrane surface, there are circumstances in which the presence of a cake improves performance in the long term. It was noted that when operating above the maximum crossflow for deposition ( with particles of similar size to the membrane pores ), permeate flowrate declined to lower values than those obtained with an established cake. This feature is thought to depend on continued pore blocking by particles having freedom of movement on the membrane surface. Once developed, the structure of a filter cake stabilizes the first layer of particles adjacent to the membrane thus preventing further pore blocking.

8. The equilibrium of deposited mass was shown to be irreversible under most operating conditions. This emphasizes the role that surface forces play in the establishment of a filter cake. Theories based on a mass balance between the rate of particulate deposition and cake resuspension were shown to be inadequate to model the system under investigation. At very high flows ( typically 12m $s^{-1}$, for

which the associated shear stress was over 400N $m^{-2}$ ), the slow resuspension observed was assumed to be due to an erosion mechanism. However, this velocity is very high for a crossflow process, and considerably larger than that required to arrest the development of filter cake due to frictional equilibrium. For the latex suspension used in these experiments, resuspension of filter cake is of academic rather than practical importance.

9. Extrapolation of the frictional force balance from steady state performance to dynamic cake growth has been proposed. The rate of cake growth was shown to be a fraction of the convective mass transport rate to the cake surface. This fraction, the sticking factor, varies throughout the growth from 1 to 0, taking a value dependent on the values of permeate velocity and shear stress. As these variables change, some sites on the cake surface are unable to accept depositing particles due to the unfavourable force balance in that geometry. While rigorous modelling of the relationship between the sticking factor and ( $\tau$ , v ) was not possible, it was demonstrated that for a monodisperse distribution, the sticking factor can take all values between 0 and 1. This is not in contradiction with the result for mixed particles, which suggested that deposition occurs with the same distribution as the bulk suspension until the equilibrium line has been crossed. In the mixed particle case, the large-particle equilibrium line was crossed soon after the experiment began rather than gradually approached, therefore a decrease in the sticking factor for the large particles was not apparent.

In summary, the main aims of the project have been fulfilled: the mechanisms responsible for steady state filtration of particulate matter have been elucidated and consideration of these phenomena has led to the successful modelling of crossflow filter performance.

# CHAPTER 8

## SUGGESTIONS FOR FURTHER INVESTIGATION

With any piece of work, the possibilities for continued experimentation grow more numerous as progress is made. This has certainly applied to the present project. The most promising lines of further investigation are now outlined under the same headings as in chapter 5.

### 8.1 Steady State Filtration

(i) The most obvious continuation to characterize the permeate velocity - shear stress relationship is to use polystyrene latex particles of different sizes to determine the equilibrium line slope with respect to particle diameter. Secondly, an interesting feature of predictions from the model is that channel diameter seems to pass through a minimum with respect to particle size ( figures 6.3 and 6.9 ). This prediction should be investigated experimentally. Only two particle sizes were used in this work, though there is no reason why the latex-manufacturing technique should not produce a range of diameters.

(ii) In addition to using particles of other sizes, different types of polymer latex could be used to determine the exact role of interparticle forces in the frictional equilibrium. In the permeate velocity - shear stress relationship, both the slope and the intercept are dependent on Van der Waals and electrostatic forces. A simple test to assess the effect of double-layer forces was made by changing the suspension pH; however, no significant variation of Van der Waals force is possible with the same chemical species.

(iii) The third main area of further investigation would be to assess the effect of bulk concentration. While the force balance model does not explicitly predict a dependence of permeate velocity on concentration, some workers have reported that final permeate flux

decreases with increasing concentration [9,32]. In terms of the frictional model, this phenomenon must be interpreted as an increase in attractive particle interactions and deviation from the assumed forms of hydrodynamic forces due to crowding effects. While this task lay outside the original definition of the work programme, the effect should be examined.

## 8.2 Resuspension

While the experimental evidence was sufficient to ascribe an erosive mechanism to resuspension at high crossflow, no direct quantitative examination of the filter cake re-entrainment was possible. To obtain this information, a membrane test section should be constructed to allow visual examination of the cake, or a radioactive tracer technique employed, to get direct estimates of the cake loading. The second option would allow continued use of tubular filters.

## 8.3 Dynamic Filtration

In this work, the problems in assessing the relationship of sticking factor with permeate velocity and shear stress were due to the dependence of the calculated value of sticking factor on these two parameters. To resolve this, independent measurement of cake mass would be required. This could be provided by a radioactive tracer or by using high-accuracy pressure gauges to measure channel diameter. In this work the pressure gauges were reliable to 0.01 bar - accurate assessment of channel diameter should be possible with a resolution of 0.001 bar.

## NOMENCLATURE

| | |
|---|---|
| $a$ | particle radius |
| $A$ | area |
| $A_{131}$ | Hamaker constant |
| $C$ | concentration |
| $C_D$ | drag coefficient |
| $d$ | diameter |
| $D$ | diffusion coefficient |
| $e$ | cake voidage / charge on an electron |
| $F$ | force |
| $f$ | Fanning friction factor |
| $G$ | shear rate |
| $I$ | an integral |
| $J$ | permeate flux |
| $k$ | a constant |
| $k_B$ | Boltzmann's constant |
| $k_{cr}$ | crowding factor |
| $k_{eq1}$ | frictional equilibrium constant |
| $k_{eq2}$ | frictional equilibrium constant |
| $k_f$ | coefficient of friction |
| $K$ | ratio of a : $d_f$ |
| $K_D$ | Inverse Debye length |
| $K_e$ | erosion coefficient |
| $L$ | length |
| $m$ | mass |
| $N_{av}$ | Avagadro's number |
| $P$ | pressure |
| $Q$ | volumetric flowrate |
| $R_m$ | membrane hydraulic resistance |
| $r$ | radial co-ordinate |
| $r_c$ | specific cake resistance |
| $s$ | separation distance |
| $t$ | time |
| $T$ | temperature |
| $u$ | axial velocity |
| $v$ | normal velocity |

| | |
|---|---|
| $\underline{v}$ | velocity vector |
| V | volume |
| $V_z$ | zeta potential |
| x | axial co-ordinate |
| y | normal co-ordinate |
| z | valence |
| $\alpha$ | sticking factor |
| $\beta$ | dimensionless position |
| $\delta$ | boundary layer thickness / error in |
| $\Theta$ | slip coefficient |
| $\mu$ | viscosity |
| $[\mu]$ | intrinsic viscosity |
| $\Sigma_0$ | permittivity of vacuum |
| $\Sigma$ | relative permittivity of medium |
| $\sigma$ | density |
| $\tau$ | shear stress |
| $\Phi$ | volume fraction |
| $\underline{\Omega}$ | angular velocity vector |
| Re | Reynolds number |
| Sh | Sherwood number |
| Sc | Schmidt number |

Subscripts

| | |
|---|---|
| 1...n | succesive general subscripts |
| a | attractive / active |
| av | average |
| b | bulk |
| c | cake / concentrated flowing layer |
| cr | crowding |
| D | difference |
| eq | equilibrium |
| f | fluid / friction / free ( channel dimension ) |
| i | inlet |
| int | interface |

| | |
|---|---|
| ip | interparticle |
| l | lift |
| m | membrane / maximum |
| ns | no slip |
| o | original / outlet / vacuum / suspending fluid |
| p | permeate / particle |
| r | relative / repulsive |
| s | slip / suspension / section |
| ST | Stokes |
| t | tube / total |
| w | wall |
| x | axial direction |
| y | normal direction |

Superscripts

| | |
|---|---|
| n | an index |
| * | friction ( boundary layer variable ) |
| + | dimensionless variable |

## REFERENCES


1. Murkes J. and Carlsson C.G., Crossflow Filtration, John Wiley and Sons, Chichester, 1988
2. Gutman R.G., Membrane Filtration, Adam Hilger, Bristol, 1987
3. Michaels A.S., Chem. Eng. Prog. 64(12) (1968) 31
4. Leveque M.A., Ann. Mines 13 (1928)
5. Dittus F.W. and Boelter L.M.K., Univ. Calif. Berkeley Publ. Eng. 2 (1930) 443
6. Gekas V. and Hallstrom B., J. Memb. Sci. 30 (1987) 153
7. Belfort G. and Altena F.W., Desal. 47 (1983) 105
8. Anderson J.L., Ind. Eng. Chem. Fundam. 12(4) (1973) 488
9. Porter M.C., Ind. Eng. Chem. Prod. Res. Dev. 11(3) (1972) 234
10. Blatt W.F., David A., Michaels A.S. and Nelson L., in Membrane Science and Technology ed. J. Flinn, Plenum Press, New York, 1970
11. Leonard E.F. and Vassilieff C.S., Chem. Eng. Comm. 30 (1984) 209
12. Birdsell S.A., M.S. Thesis, Univ. Colerado (1985)
13. Davis R.H. and Birdsell S.A., Chem. Eng. Comm. 49 (1987) 217
14. Bernstein E.F., Blackshear P.L. and Keller K.H., Am. J. Surg. 114 (1967) 126
15. Eckstein E.C., Bailey D.G. and Shapiro A.H., J. Fluid Mech. 79(1) (1977) 191
16. Leighton D.T. and Acrivos A., J. Fluid Mech. 181 (1987) 415
17. Zydney A.L. and Colton C.K., Chem. Eng. Comm. 47 (1986) 1
18. Davis R.H. and Leighton D.T., Chem. Eng. Sci. 42(2) (1987) 275
19. Romero C.A. and Davis R.H., J. Memb. Sci. 39 (1988) 157
20. Segre G. and Silberberg A, J. Fluid Mech. 14 (1962) 115
21. Rubinow S.I., Keller J.B., J. Fluid Mech. 11 (1961) 447
22. Saffman P.G., J. Fluid Mech. 22 (1965) 385, and the associated corrigendum Saffman P.G., J. Fluid Mech. 31 (1968) 624
23. Clift R., Grace J.R. and Weber M.E., Bubbles, Drops and Particles, Academic Press, 1978
24. Jeffrey J.B., Proc. Roy. Soc. A 102 (1922) 161
25. Cox R.G. and Brenner H., Chem. Eng. Sci. 23 (1968) 147
26. Vasseur P. and Cox R.G., J. Fluid Mech. 78(2) (1976) 385
27. Green G. and Belfort G., Desal. 35 (1980) 129
28. Belfort G., Chin P. and Dziewulski D.M., Proc. World Filt.

Congress III (Sept. 1982) Philadelphia, V.2 548
29. Altena F.W., Belfort G., Otis J., Fiessinger F., Rovel J.M. and Nicoletti J., Desal. 47 (1983) 221
30. Altena F.W. and Belfort G., Chem. Eng. Sci. 39(2) (1984) 343
31. Kern D.Q. and Seaton R.E., Brit. Chem. Eng. (May 1959) 258
32. Schulz G. and Ripperger S., J. Memb. Sci. 40 (1989) 173
33. Fane A.G., Fell C.J.D. and Nor M.T., I. Chem. E. Symp. Ser. 73 (1982) C1
34. Fane A.G., J. Memb. Sci. 20 (1984) 249
35. Fage A. and Townsend H.C.H., Proc. Roy. Soc. A 135 (1932) 656
36. Kline S.J., Reynolds W.C., Schraub F.A. and Runstadler P.W., J. Fluid Mech. 30 (1967) 741
37. Corino E.R. and Brodkey S., J. Fluid Mech. 37 (1969) 1
38. Cleaver J.W. and Yates B., J. Coll. Int. Sci. 44(5) (1973) 464
39. Cleaver J.W. and Yates B., Chem. Eng. Sci. 30 (1975) 983
40. Cleaver J.W. and Yates B., Chem. Eng. Sci. 31 (1976) 147
41. Gutman R.G., The Chem. Eng. No. 322 (1977) 510
42. Knibbs R.H., Harwell Laboratory Report AERE - R 10269 (1984)
43. Yung B.P.K., Merry H. and Bott T.R., Chem. Eng. Sci. 44(4) (1989) 873
44. Hall D., J. Fluid Mech. 187 (1988) 451
45. Ebner H., Chem. Ing. Tech. 53(1) (1981) 25
46. Rautenbach R. and Schock G., J. Memb. Sci. 36 (1988) 231
47. Fischer E. and Raasch J., Proc. 4th World Filt. Cong. Ostende (1986) Part II 11.11
48. Lu W.-M. and Ju S.-C., Sep. Sci. Technol. 24(7&8) (1989) 517
49. McDonogh R.M., Fane A.G. and Fell C.J.D., J. Memb. Sci. 43 (1989) 69
50. Langmuir I., J. Phys. Chem. 6 (1938) 69
51. J. Th. Overbeek, in Colloid Science Vol. 1 ed. Kruyt H., Elsevier, Amsterdam 1952
52. Cohen R.D. and Probstein R.F., J. Coll. Int. Sci. 114(1) (1986) 194
53. Wakeman R.J. and Tarleton E.S., Chem. Eng. Sci. 42(4) (1987) 829
54. Kuo R.J. and Matijevic E., J. Coll. Int. Sci. 78(2) (1980) 407
55. Ishii K. and Hasimoto H., J. Phys. Soc. Jpn. 48(6) (1980) 2144
56. O'Neill M.E., Chem. Eng. Sci. 23 (1968) 1293
57. Chang E.Y. and Acrivos A., Phys. Chem. Hydr. 10(5/6) (1988) 579

58. Brinkman H.C., Appl. Sci. Res. A1 (1947) 27
59. Scott G.D., Nature 188 (1960) 908
60. Schenkel J.H. and Kitchener J.A., Trans. Farad. Soc. 56 (1960) 161
61. Prieve D.C. and Russel W.B., J. Coll. Int. Sci 125(1) (1988) 1
62. Israelachvili J.N., Intermolecular and Surface Forces, Academic Press, New York, 1985
63. Derjaguin B. and Landau L., Acta. Physicochim. 14 (1941) 633
64. Dodds P.W., Ph.D. Thesis (1985), Imperial College, London University
65. Schlichting H., Boundary Layer Theory, McGraw Hill, New York (1955)
66. Goodwin J.W., Hearn J., Ho C.C. and Ottewill R., Coll. Polym. Sci. 252 (1974) 464
67. Krieger I.M., Adv. Coll. Int. Sci. 3 (1972) 111
68. Coulson J.M. and Richardson J.F., Chemical Engineering Vol.2, 3$^{e}$ (1978) Pergamon Press
69. Massey B.S., Mechanics of Fluids, 4$^{e}$ (1979) Van Nostrand
70. Singh R., Chem. Eng. Prog. 85(6) (June 1979) 59
71. Beavers G.S., and Joseph D.D., J. Fluid Mech. 30(1) (1967) 197
72. Belfort G., J. Memb. Sci. 40 (1989) 123
73. Beavers G.S., Sparrow E.M., and Magnuson R.A., J. Basic Eng. 92 (1970) 843

# APPENDIX A

## RIG COMPONENTS

### 1. Pipework

George Fisher ( GF ) uPVC 1/2, 3/4 and 1 inch

Tank : polypropylene, 70 litre capacity

### 2. Pumping system

Lowara CK 120/55 1.8kW three phase centrifugal pump

Tungsten carbide mechanical seal

Speed control : Mitsubishi frequency converter FR-K-H5.5K

### 3. Heat exchanger

1.25" OD stainless steel tube. Area 0.17$m^2$.

### 4. Valves

| | |
|---|---|
| Downstream of tube flowmeter | Lancashire fittings 15mm ball. |
| Test section exit | GF DN15 diaphragm. |
| Test section bypass | GF DN15 diaphragm. |

### 5. Flowmeters

Tube : Krohne X1000 Altoflux meter DN10

SC100 signal converter 0-20mA output

Full scale variable between 2.3 and 50$dm^3min^{-1}$

Accuracy : 0.2% full scale

Permeate : Maywood Instruments Uniweigh 500g load cell

Output 0-10V

Accuracy : 0.15g

6. Pressure measurement

Transamerica BHL-3020 series transducers 10 bar full scale
Output 0-100mV
Accuracy : calibrated to NPL standards
consistent to 0.01 bar

7. Temperature measurement

CIL PCI 1002 unit with type T thermocouples
Output IEEE
Typical accuracy for type T : 0.4$^{o}$C

8. Signal processing

3D 12 bit analogue to digital converter
Inputs reconfigured to 0-20mA, 0-100mV and 0-10V
Output IEEE

9. Computer system

Commodore 8296 computer with 8250LP disk drive
Mains supply filtered with Centronic 500M

## APPENDIX B

## COMPUTER LOGGING PROGRAM

```
10   goto 10000

999  rem **********
1000 rem  interrogation of temperature unit
1001 rem **********
1002 z2=0
1003 z2=z2+1
1005 for tc=3 to 7
1010 open 9,9,tc:get#9,j$,k$
1020 k=asc(k$)-224:if k<0 then d=(k+32)*-1
1030 if k>=0 then d=k
1040 d=d*256
1050 if j$="" then j=0:goto 1070
1060 j=asc(j$)
1070 if k<0 then j=j*-1
1080 a(tc)=j+d:close9:next tc
1100 for tc=4 to 7
1110 t=a(tc)*2.5:cj=a(3)/40
1120 t(tc)=t(tc)+k(0)+k(1)*t+k(2)*t^2+k(3)*t^3+k(4)*t^4+cj
1130 next tc
1140 for tc=4to7:v(tc+1)=int(t(tc)*10/z2+0.5)/10:next tc

2000 rem **********
2001 rem  interrogation of a to d converter
2002 rem **********
2005 open 2,7,16:open 3,7,20:open 4,7,24
2010 for ac=0 to 4 step 2
2015 if ac=4 then ac=6
2020 open 7,7,ac
2030 get#7,a$:get#2,a$:get#3,a$:get#4,b$
2040 a=asc(a$+chr$(0)):b=asc(b$+chr$(0))
2050 b=b and 240:b=b/16
2060 d3(ac)=b+a*16
```

```
2080 close7
2085 next ac
2090 open 7,7,3
2095 rem *** loop for load cell interrogation ***
2100 for i=1 to 5
2110 get#7,a$:get$2,a$:get#3,a$:get#4,b$
2120 t1=ti-t1
2125 a=asc(a$+chr$(0)):b=asc(b$+chr$(0))
2130 b=b/16+a*16
2140 if z2=1 then b1=b
2150 sy=sy+b:sx=sx+t1:sb=sb+b*t1:s2=s2+t1*t1
2160 next i:close7
2170 close2:close3:close4
2210 ft=ft+fs*d3(6)/4096
2220 pi=pi+3.714e-3*d3(0)+0.193
2230 po=po+2.246e-3*d3(2)-0.078
2250 if ti-t1<dt goto 1003
2260 t2=ti:n=z2*5
2265 if b<b1 then f2=0:v(9)=0:goto 3000
2285 rem *** linear regression on load cell data ***
2286 rem *** for permeate flowrate ***
2290 v(9)=565.7*(sy*sx-n*sb)/(sx*sx-n*s2)

3000 rem **********
3001 rem  writing data to disk file
3002 rem **********
3010 t1=(t1-t0)/60: t2=(t2-t0)/60
3020 v(10)=int(0.5+b*100/4096)
3030 v(1)=int(10000*(t1+t2)/7200+0.5)/10000
3050 v(2)=ft*60000/z2:v(2)=int(v(2)*100+0.5)/100
3130 v(3)=int(pi*100/z2+0.5)/100
3150 v(4)=int(po*100/z2+0.5)/100
3205 if f1=0 or f2=0 goto 4004
3210 append#1,(f$),d1:for j=1 to 9:print#1,v(j):next j:dclose#1
```

```
4000 rem **********
4001 rem  set up screen printing of variables
4002 rem **********
4004 for j=1 to 10:for i=1 to 9:poke p(j)+i-1,32:next i:next j
4005 v(1)=int(v(1)*60*10+0.5)/10
4030 v(9)=int(100*v(9)+0.5)/100
4100 for j=1 to 10:a$=str$(v(j)):for i=1 to len(a$)
4110 a1$=mid$(a$,i,1): a=asc(a1$)
4120 poke p(j)+i,a:next i:next j:return

6000 rem **********
6001 rem  set up screen printing of headings
6002 rem **********
6010 print"Run code"tab(29);f$
6040 print"Elapsed time"tab(40)"minutes"
6060 print"Tube flow"tab(40)"litres/min"
6100 print"Inlet pressure"tab(40)"bar"
6120 print"Outlet pressure"tab(40)"bar"
6160 print"Inlet temperature"tab(40)"deg.C"
6180 print"Outlet temperature"tab(40)"deg.C"
6190 print"Tank temperature"tab(40)"deg.C"
6200 print"Ambient temperature"tab(40)"deg.C"
6210 print"Permeate flow"tab(40)"ml/min"
6220 print"Load cell output"tab(40)"%"
6250 if f1=0 then print"SHIFT L TWICE TO BEGIN LOGGING":goto 6280
6260 print"SHIFT E TO STOP LOGGING"
6280 return

7000 rem **********
7001 rem  create headings for disk file
7002 rem **********
7010 dopen$1,(f$),d1,w
7020 print#1,9,",chr$(34)(f$+str$(fc))chr$(34)
7030 print#1,"Time (hours)"
7040 print#1,"Tube flow (litres/min)"
7050 print#1,"Inlet pressure (bar)"
7060 print#1,"Outlet pressure (bar)"
7070 print#1,"Inlet temperature (deg.C)"
```

```
7080 print#1,"Outlet temperature (deg.C)"
7090 print#1,"Tank temperature (deg.C)"
7100 print#1,"Ambient temperature (deg.C)"
7130 print#1,"Test segment permeate flowrate (ml/min)"
7140 dclose#1:return

10000 rem **********
10001 rem  main body of controlling program
10002 rem **********
10004 dim tj(22):dim mm(22)
10005 dim a(8):dim t(8):dim d3(8):k(1)=2.5661e-2:dim v(11)
10006 dim p(11):k(0)=0:k(2)=-6.1955e-7:k(3)=2.2182e-11
10007 k(4)=-3.5501e-16:p(1)=33035:p(2)=33195:p(3)=33355:p(4)=33435
10008 p(5)=33595:p(6)=33675:p(7)=33755:p(8)=33835:p(9)=33995
10009 p(10)=34155
10010 input"Enter filename";f$
10020 input"Full scale value of test section flowmeter (m3/hr);fh
10025 fs=fh/3600
10030 input"Enter approximate time interval for data logging (s)";dt
10032 dt=dt*60
10034 gosub 6000
10035 t0=ti
10036 t1=ti:gosub 1000:ft=0:fp=0:pi=0:po=0:sy=0:sx=0:sb=0:s2=0
10038 for q=4 to 8:t(q)=0:next q
10040 get k$:if k$<>"L" goto 10036
10042 f1=1:gosub 6000:gosub 7000
10043 get k$:if k$<>"L" goto 10043
10045 t0=ti
10050 t1=ti:f2=1:gosub 1000:ft=0:fp=0:pi=0:po=0:sx=0:sy=0:sb=0:s2=0
10070 get k$:if k$="E" goto 12000
10076 for q=4 to 8:t(q)=0:next q
10080 goto 10050

12000 rem **********
12010 print"DATA COLLECTION ENDED"
12020 end
```

## APPENDIX C

### STEADY STATE RUN DATA

| Run code | Membrane type | $d_p$ (μm) | $Q_t$ ($dm^3 min^{-1}$) | P (bar) | $R_m x10^{-12}$ ($m^{-1}$) |
|---|---|---|---|---|---|
| 1 | Carbosep | 0.55 | 1.75 | 0.96 | 4.9 |
| 2 | | | 1.5 | 1.05 | 5.0 |
| 3 | | | 1.0 | 1.05 | 4.9 |
| 4 | | | 3.0 | 2.02 | 4.4 |
| 5 | | | 3.0 | 1.95 | 3.2 |
| 6 | | | 2.0 | 1.91 | 4.4 |
| 7 | | | 2.0 | 1.98 | 3.3 |
| 8 | | | 1.75 | 1.84 | 4.2 |
| 9 | | | 1.7 | 1.82 | 3.4 |
| 10 | | | 4.1 | 2.72 | 3.4 |
| 11 | | | 3.0 | 2.77 | 4.3 |
| 12 | | | 2.0 | 2.80 | 4.6 |
| 13 | Ceraver | 0.55 | 8.5 | 0.53 | |
| 14 | 0.1 | | 8.5 | 1.94 | |
| 15 | | | 8.2 | 0.83 | |
| 16 | | | 6.2 | 0.97 | |
| 17 | | | 4.0 | 1.08 | |
| 18 | | | 3.0 | 0.74 | |
| 19 | | | 3.0 | 0.90 | 0.22 |
| 20 | | | 3.0 | 2.29 | |
| 21 | | | 2.95 | 1.12 | |
| 22 | | | 2.3 | 0.92 | 0.21 |
| 23 | | | 1.2 | 0.94 | 0.22 |
| 24 | Ceraver | 0.55 | 5.0 | 0.84 | 0.12 |
| 25 | 0.2 | | 4.0 | 0.89 | |
| 26 | | | 3.0 | 0.91 | |
| 27 | | | 2.0 | 0.94 | |
| 28 | | | 2.0 | 0.96 | |

| Run code | $d_f$ (mm) | Re | e | $rx10^{-15}$ ($m^{-2}$) | $vx10^{5}$ ($m\ s^{-1}$) | $\tau$ ($N\ m^{-2}$) |
|---|---|---|---|---|---|---|
| 1 | 5.86 | 6330 | | | 1.8 | 4.7 |
| 2 | 5.77 | 5510 | 0.384 | | 1.8 | 3.6 |
| 3 | 4.88 | 4340 | 0.369 | 4.5 | 1.7 | 3.1 |
| 4 | 5.58 | 11400 | | 2.4 | 5.0 | 13.3 |
| 5 | 5.67 | 11200 | | 5.4 | 5.2 | 13.6 |
| 6 | 5.01 | 8460 | | 4.5 | 3.8 | 8.5 |
| 7 | 5.12 | 8280 | 0.414 | 5.3 | 4.1 | 8.8 |
| 8 | 4.48 | 8280 | | 3.3 | 3.5 | 7.7 |
| 9 | 4.93 | 7310 | 0.415 | 5.1 | 3.5 | 6.8 |
| 10 | 5.87 | 14800 | | | 6.6 | 22.2 |
| 11 | 5.52 | 11500 | | 4.5 | 5.6 | 15.2 |
| 12 | 4.89 | 8670 | | 3.9 | 4.9 | 13.4 |
| 13 | 6.73 | 26800 | | | 19.5 | 51.9 |
| 14 | 6.54 | 27600 | | | 25.2 | 57.9 |
| 15 | 6.64 | 26100 | | | 20.3 | 50.2 |
| 16 | 6.47 | 20200 | | | 15.3 | 31.5 |
| 17 | 6.05 | 14000 | | | 11.4 | 16.5 |
| 18 | 5.94 | 10700 | | | 8.8 | 10.2 |
| 19 | 5.76 | 11000 | 0.346 | 2.0 | 8.3 | 11.5 |
| 20 | 5.16 | 12300 | 0.361 | 2.4 | 13.0 | 17.6 |
| 21 | 5.73 | 10900 | 0.363 | 2.4 | 10.4 | 11.8 |
| 22 | 5.44 | 8960 | 0.354 | 1.6 | 8.5 | 7.8 |
| 23 | 4.46 | 5700 | 0.356 | 1.4 | 6.9 | 5.1 |
| 24 | 6.39 | 16600 | 0.412 | | 13.3 | 21.9 |
| 25 | 6.17 | 13700 | 0.358 | | 11.8 | 15.9 |
| 26 | 5.83 | 10900 | 0.361 | | 9.8 | 11.7 |
| 27 | 5.25 | 8080 | 0.359 | | 9.2 | 7.5 |
| 28 | 5.23 | 8110 | 0.394 | | 9.3 | 6.3 |

| Run code | Membrane type | $d_p$ (μm) | $Q_t$ ($dm^3 min^{-1}$) | P (bar) | $R_m x10^{-12}$ ($m^{-1}$) |
|---|---|---|---|---|---|
| 29 | Carbosep | 1.8 | 0.8 | 1.86 | 3.9 |
| 30 | | | 0.6 | 1.86 | 4.0 |
| 31 | | | 0.6 | 1.87 | 5.1 |
| 32 | | | 0.4 | 2.12 | 7.7 |
| 33 | | | 0.4 | 1.83 | 4.6 |
| 34 | | | 0.4 | 2.11 | 6.2 |
| 35 | Ceraver | 1.8 | 2.8 | 1.00 | |
| 36 | 0.1 | | 2.5 | 1.01 | |
| 37 | | | 2.3 | 0.90 | 0.24 |
| 38 | | | 2.3 | 0.91 | 0.27 |
| 39 | | | 1.9 | 1.02 | |
| 40 | | | 1.8 | 0.89 | 0.27 |
| 41 | | | 1.5 | 1.02 | |
| 42 | | | 1.25 | 0.89 | 0.15 |
| 43 | | | 1.25 | 0.92 | 0.10 |
| 44 | | | 1.25 | 0.89 | 0.25 |
| 45 | | | 1.0 | 1.00 | |
| 46 | | | 0.8 | 0.85 | 0.23 |
| 47 | | | 0.5 | 0.91 | 0.23 |
| 48 | | | 0.5 | 0.88 | 0.33 |
| 49 | Ceraver | 1.8 | 5.0 | 0.80 | 0.12 |
| 50 | 0.2 | | 4.0 | 0.86 | |
| 51 | | | 3.0 | 0.89 | |
| 52 | | | 2.0 | 0.92 | |
| 53 | | | 1.5 | 0.94 | |
| 54 | Ceraver | 1.8 + | 7.0 | 0.78 | |
| 55 | 0.1 | 0.55 | 6.0 | 0.82 | 0.21 |
| 56 | | | 5.1 | 0.87 | |
| 57 | | | 4.0 | 0.92 | |
| 58 | | | 3.0 | 0.96 | |
| 59 | | | 2.3 | 0.91 | 0.20 |
| 60 | | | 0.5 | 0.97 | 0.21 |

| Run code | $d_f$ (mm) | Re | e | $rx10^{-15}$ ($m^{-2}$) | $vx10^{5}$ ($m\ s^{-1}$) | $\tau$ ($N\ m^{-2}$) |
|---|---|---|---|---|---|---|
| 29 | 4.13 | 4110 | 0.342 | 0.57 | 5.9 | 4.9 |
| 30 | 3.39 | 3750 | 0.353 | 0.46 | 6.8 | 5.8 |
| 31 | 3.36 | 3790 | 0.368 | 0.81 | 5.0 | 4.6 |
| 32 | 2.98 | 2850 | 0.357 | 1.4 | 3.9 | 4.0 |
| 33 | 2.34 | 3620 | 0.365 | 0.79 | 6.8 | 5.6 |
| 34 | 3.40 | 2490 | 0.358 | 1.0 | 4.9 | 4.6 |
| 35 | 6.04 | 9860 | | | 18.9 | 8.6 |
| 36 | 5.75 | 9140 | | | 18.5 | 8.2 |
| 37 | 5.20 | 9500 | 0.380 | 0.38 | 18.2 | 10.4 |
| 38 | 5.22 | 9460 | 0.394 | 0.49 | 16.1 | 10.4 |
| 39 | 5.21 | 7890 | | | 18.2 | 7.4 |
| 40 | 4.62 | 7750 | 0.369 | 0.27 | 19.5 | 9.2 |
| 41 | 4.57 | 6820 | | | 18.9 | 7.2 |
| 42 | 3.53 | 7450 | 0.398 | 0.25 | 24.2 | 10.1 |
| 43 | 3.77 | 6970 | | 0.26 | 25.7 | 9.7 |
| 44 | 4.00 | 6520 | | 0.28 | 18.8 | 9.1 |
| 45 | 3.66 | 5680 | | 0.33 | 20.2 | 7.8 |
| 46 | 2.92 | 5810 | | 0.29 | 17.0 | 12.5 |
| 47 | 2.42 | 4380 | | 0.26 | 21.5 | 10.4 |
| 48 | 2.16 | 4910 | 0.381 | 0.26 | 20.6 | 8.0 |
| 49 | 6.34 | 16700 | | 1.0 | 25.4 | 19.9 |
| 50 | 6.09 | 13900 | | 0.89 | 22.2 | 15.7 |
| 51 | 5.73 | 11100 | | 0.66 | 21.8 | 11.5 |
| 52 | 5.19 | 8170 | | 0.61 | 18.0 | 7.4 |
| 53 | 4.42 | 7200 | | | 16.0 | 8.8 |
| 54 | 6.64 | 22400 | | | 16.3 | 37.1 |
| 55 | 6.57 | 19400 | | | 16.1 | 28.2 |
| 56 | 6.44 | 16500 | | | 14.3 | 22.1 |
| 57 | 6.24 | 13600 | | | 11.5 | 14.3 |
| 58 | 5.91 | 10800 | | | 10.4 | 10.1 |
| 59 | 5.62 | 8680 | 0.356 | 1.7 | 9.0 | 6.4 |
| 60 | 4.40 | 2410 | 0.323 | 1.2 | 7.4 | 1.2 |

## APPENDIX D

## EXAMPLE CALCULATIONS

A complete example calculation is followed through to illustrate the processing of experimental data. The experiment is number 40 in appendix C. Data are listed in convenient units, but all calculations are performed in S.I. . Values of data may be listed to greater accuracy than experimental errors allow, this is to prevent rounding errors in calculation.

Direct experimental data:

| | |
|---|---|
| Tube type | Ceraver 0.1 |
| Initial tube diameter ($d_o$) | 6.78mm |
| Final tube diameter ($d_f$) | 4.62mm |
| Length of membrane from which permeate flow measurements were taken ($L_s$) | 0.102m |
| Length of membrane over which the filter cake adhered ($L_a$) | 0.700m |
| Cake mass (m) | 0.00905kg |
| Tube flowrate ($Q_t$) | $1.8 dm^3 min^{-1}$ |
| Operating temperature | $17.5^oC$ |
| Viscosity | $1.067 mN\ s\ m^{-2}$ |
| Solids concentration ($C_b$) | $4.18 kg\ m^{-3}$ |
| Suspension volume in rig | $0.025 m^3$ |
| Initial conditions: | |
| Permeate flowrate ($Q_p$) | $42.2 ml\ min^{-1}$ |
| Entry pressure ($P_i$) | 1.01bar |
| Exit pressure ($P_o$) | 0.86bar |
| Final conditions: | |
| Permeate flowrate | $17.3 ml\ min^{-1}$ |
| Entry pressure | 1.01bar |
| Exit pressure | 0.81bar |

Calculations:

(i) Shear stress

At the end of the run, the axial tube pressure drop was 0.20 bar of which 0.13 bar was gravity head between the pressure gauges. In Ceraver tubes, the pressure drop due to shear stress on the cake surface was 80% of the total frictional loss. In cylindrical geometry, the following equation for shear stress applies

$$\tau = \frac{P_D\, d_f}{4\, L_a} \qquad \text{(D1)}$$

where $P_D$ is the axial pressure drop due to friction ( other variables are defined on the previous page ). Substitution of the appropriate values gives $\tau = 9.2\text{N m}^{-2}$.

(ii) Permeate velocity

Permeate velocity is calculated from the flowrate by

$$v_w = Q_p / \Pi\, d_f\, L_s \qquad \text{(D2)}$$

Substitution of the listed values gives $1.95\text{x}10^{-4}\text{m s}^{-1}$.

(iii) Bulk pressures

For Ceraver tubes, the values of the constants in equation 4.5 are $k_1 = 0.34$, $k_2 = 0.66$, $k_3 = 811$ and $k_4 = 2700$. For the initial and final data sets, the actual bulk pressures at the permeate measurement point are 0.935 and 0.889 bar.

(iv) Hydraulic membrane resistance

Use of equation 3.20 with the initial conditions ( $P_w = P_b$ ) gives the result that $R_m = 2.707\text{x}10^{11}\text{m}^{-1}$.

(v) Cake voidage

Re-arranging equation 3.19 gives an expression for voidage in terms of directly measured variables. Substitution of experimental values gives e = 0.369 .

(vi) Specific cake resistance

Having obtained the value of membrane resistance, equation 3.20 can be used with the final conditions to calculate the pressure at the cake-membrane interface ( $P_w$ ). The result is 0.383 bar. Using this value in equation 3.21 results in a specific cake resistance of $2.748 \times 10^{14} m^{-2}$.

(vii) Cake mass

From the experimental data of tube flowrate, inlet and outlet pressures, and permeate flowrate, the cake mass as a function of time can now be calculated. Bulk pressure is calculated from equation 4.5, using the value of channel diameter from calculation of the previous data point ( or the original value for the first point ). This is an approximation to make calculation easier, although it means that the m - t curve will be slightly offset from its true position; however, this deviation is much smaller than errors from other sources. Ultimate convergence of cake mass to the experimental value is assured by the nature of the calculation. Equation 3.22 is used to calculate cake mass and channel diameter is obtained from equation 3.19. Overleaf, table D1 shows the values for experiment 40.

The mass data are plotted against time in figure D1 from which the gradient is evaluated graphically. At each point where the mass deposition rate is estimated, the permeate flowrate can be found by interpolation of the tabulated data in table D1. To extend the calculation over the whole membrane, the permeate flowrate is multiplied by 0.7 / 0.102 ( ratio of total membrane length to that from which permeate was collected ). From the cake mass, the solids concentration in the rig can be evaluated by a mass balance. This step is necessary to compensate for the decrease in bulk

concentration, which by the end of run 40 had dropped by 9% . Use of equation 3.18 then gives the sticking factor. The values used for the example calculations are given in table D2.

TABLE D1

CALCULATION OF CAKE MASS

| Time (min) | $P_i$ (bar) | $P_o$ (bar) | $Q_p$ (ml/min) | $P_b$ (bar) | $d_f$ (mm) | m (g) |
|---|---|---|---|---|---|---|
| 1.6 | 1.00 | 0.86 | 37.0 | 0.931 | 6.52 | 1.28 |
| 2.7 | 1.01 | 0.86 | 33.5 | 0.934 | 6.29 | 2.36 |
| 3.8 | 1.01 | 0.86 | 30.5 | 0.933 | 6.07 | 3.36 |
| 4.9 | 1.01 | 0.87 | 28.4 | 0.939 | 5.88 | 4.21 |
| 6.0 | 1.01 | 0.87 | 26.5 | 0.939 | 5.70 | 4.97 |
| 7.1 | 1.01 | 0.86 | 25.2 | 0.931 | 5.59 | 5.44 |
| 8.2 | 1.01 | 0.86 | 23.8 | 0.931 | 5.43 | 6.07 |
| 9.4 | 1.01 | 0.86 | 22.9 | 0.930 | 5.32 | 6.48 |
| 10.4 | 1.01 | 0.86 | 22.2 | 0.929 | 5.24 | 6.82 |
| 11.6 | 1.01 | 0.85 | 21.3 | 0.922 | 5.14 | 7.19 |
| 12.7 | 1.01 | 0.85 | 20.6 | 0.921 | 5.04 | 7.55 |
| 13.8 | 1.01 | 0.85 | 20.1 | 0.920 | 4.97 | 7.81 |
| 14.9 | 1.01 | 0.85 | 19.6 | 0.920 | 4.90 | 8.08 |
| 16.0 | 1.01 | 0.84 | 19.4 | 0.912 | 4.89 | 8.10 |
| 17.1 | 1.01 | 0.84 | 18.9 | 0.912 | 4.82 | 8.38 |
| 18.2 | 1.01 | 0.83 | 18.7 | 0.905 | 4.81 | 8.41 |
| 19.3 | 1.01 | 0.83 | 18.4 | 0.905 | 4.76 | 8.58 |
| 21.5 | 1.01 | 0.83 | 18.3 | 0.904 | 4.74 | 8.63 |
| 23.8 | 1.01 | 0.82 | 18.1 | 0.897 | 4.73 | 8.67 |
| 26.0 | 1.01 | 0.82 | 17.8 | 0.897 | 4.68 | 8.85 |
| 28.3 | 1.01 | 0.82 | 17.3 | 0.897 | 4.60 | 9.14 |
| 30.5 | 1.01 | 0.82 | 17.3 | 0.896 | 4.60 | 9.13 |
| 32.7 | 1.01 | 0.82 | 17.3 | 0.896 | 4.60 | 9.13 |
| 34.9 | 1.01 | 0.81 | 17.3 | 0.889 | 4.62 | 9.05 |
| 37.2 | 1.01 | 0.81 | 17.1 | 0.889 | 4.58 | 9.18 |
| 39.4 | 1.02 | 0.81 | 17.3 | 0.889 | 4.62 | 9.05 |
| 41.6 | 1.01 | 0.81 | 17.3 | 0.889 | 4.62 | 9.06 |

FIGURE D1

CAKE MASS vs. TIME

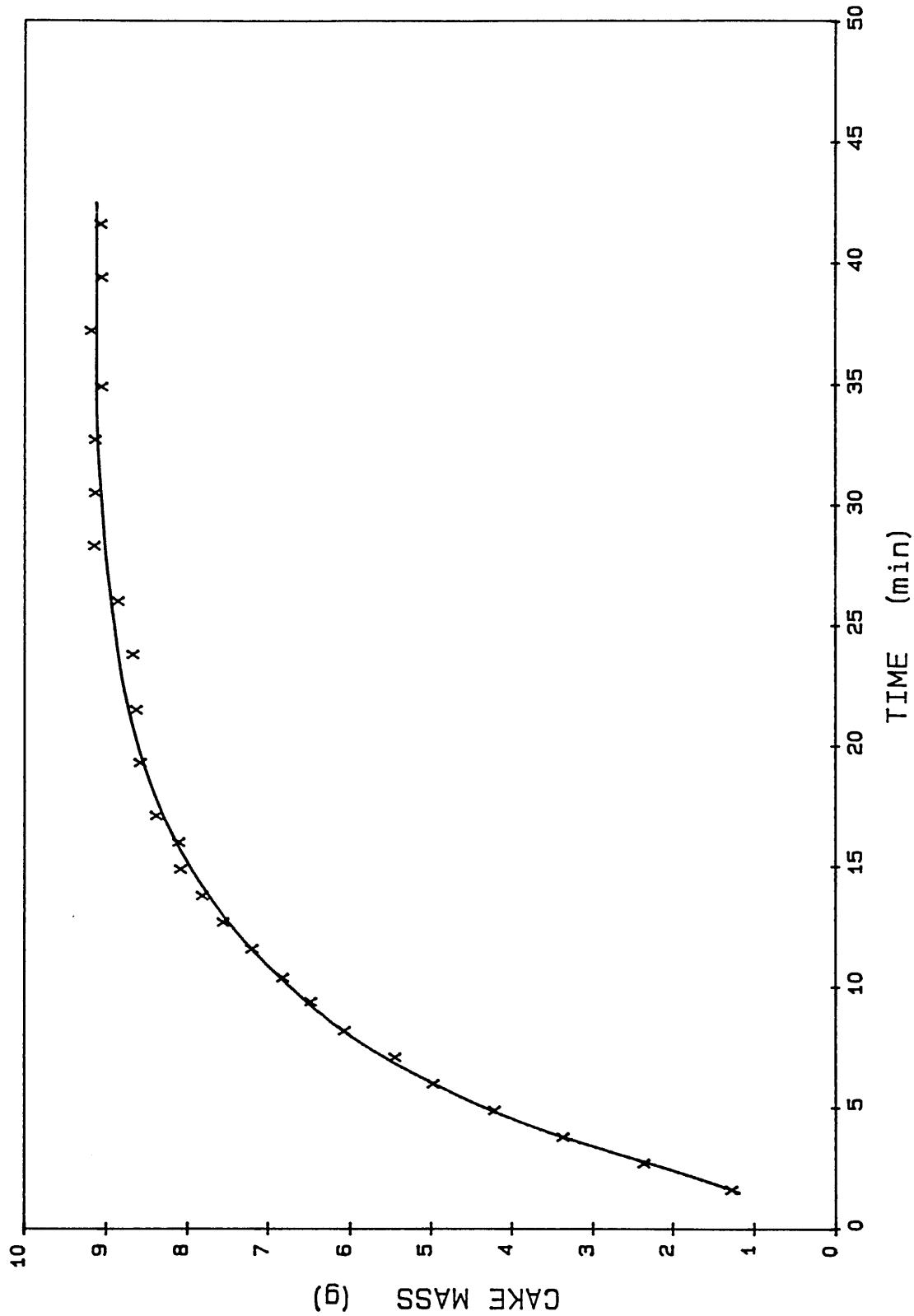


TABLE D2

CALCULATION OF STICKING FACTOR

| Time (min) | $\frac{dm}{dt} \times 10^6$ (kg $s^{-1}$) | $Q_p$ (ml/min) | m (g) | $C_b$ (kg $m^{-3}$) | $\alpha$ (-) |
|---|---|---|---|---|---|
| 2.5 | 16.11 | 34.1 | 2.16 | 4.09 | 1.01 |
| 5 | 11.99 | 28.2 | 4.28 | 4.01 | 0.93 |
| 7.5 | 7.74 | 24.7 | 5.66 | 3.95 | 0.69 |
| 10 | 5.50 | 22.5 | 6.73 | 3.91 | 0.55 |
| 12.5 | 4.04 | 20.7 | 7.44 | 3.88 | 0.44 |
| 15 | 3.10 | 19.6 | 7.97 | 3.86 | 0.36 |
| 17.5 | 2.14 | 18.9 | 8.35 | 3.85 | 0.26 |
| 20 | 1.38 | 18.4 | 8.61 | 3.84 | 0.17 |
| 22.5 | 0.89 | 18.2 | 8.79 | 3.83 | 0.11 |
| 25 | 0.70 | 17.9 | 8.90 | 3.82 | 0.09 |
| 30 | 0.35 | 17.3 | 9.05 | 3.82 | 0.05 |

The value of 1.01 for the first sticking factor arises from the approximation of no pore blocking. This limitation was discussed in section 5.3.1.

## APPENDIX E

## ERROR ANALYSIS

In this analysis, random errors in the calculated parameters are estimated from the observed random variation in directly measured variables. Systematic errors are not considered as they are difficult to determine and, as the basis of calculation in this work is consistent, they do not affect comparison of experimental results.

To determine the random error in calculated variables, a standard technique of differential calculus is applied. For the following general relation

$$y = f(x_1, x_2, x_3 \ldots\ldots x_n) \qquad \text{(E1)}$$

the random error in y, if the fluctuations in each $x_i$ are small, is approximated by

$$\delta y \approx [\sum_{i=1}^{n} (dy/dx_i)^2 \, (\delta x_i)^2]^{1/2} \qquad \text{(E2)}$$

This is applied to all the formulae used for calculation.

### Errors in measured variables

Tube flowrate ($Q_t$) : While each particular measurement of tube flowrate had a high degree of accuracy, some flow variation was caused by pump fluctuations due to the build-up of filter cake. Over an entire experiment the total variation was kept to within $\pm 0.05 dm^3 min^{-1}$.

Permeate flowrate ($Q_p$) : The error in this variable depended on the chosen time interval for the logging cycle. Usually a time interval of 2 minutes was set, which seemed to reduce the random fluctuations in permeate flowrate to $\pm 0.1 ml\ min^{-1}$.

Pressure measurements ($P_i$, $P_o$) : The pressure gauges were consistent and accurate upon calibration to NPL standards. The estimated

variation was probably less than ±0.01 bar.

Cake mass (m) : This was estimated to within ±0.1g by weighing the dried cake from backwashing.

Channel volume ($V_f$) : The channel or tube diameter was estimated by filling with water and weighing that volume to within ±0.1g.

The errors in the first three variables were caused by the measurement instruments used, while the last two were due to the limitations of experimental technique.

Errors in calculated variables

The data of run 40 in appendix C and appendix D are used to obtain typical values of errors. Calculated values are taken as appropriate to the whole data set because the limited accuracy of this error analysis does not warrant its repeated application for all experiments.

Tube and channel diameter : From direct measurement, the channel volume was 11.73ml, therefore channel diameter was calculated to be 4.62mm by geometry. Applying equation E2 to the volume of a cylinder, the errors listed above imply that the typical error on channel diameter is ±0.02mm.

Wall shear stress : Application of equation E2 to equation 4.4 with $\delta P_D$ = 0.01 bar and $\delta d_f$ = 0.02mm gives an error on wall stress of ± 1.6N $m^{-2}$. For the whole range of experimental data where the limits of shear stress were 1 - 58 N $m^{-2}$, the associated error varies between 1 and 2N $m^{-2}$.

Permeate velocity : Calculation of permeate velocity is carried out using equation 4.3. With uncertainties of $\delta Q_p$ = 0.1ml $min^{-1}$ and $\delta d_f$ = 0.02mm the error analysis gives the random error on $v_w$ as ± $10^{-6}$m $s^{-1}$. The range of permeate velocity was from $1x10^{-5}$ - $26x10^{-5}$m $s^{-1}$.

Cake voidage : Re-arranging equation 3.19 gives an expression for cake voidage. For errors of $\delta m = 0.1g$ and $\delta d_f = \delta d_o = 0.02mm$, the voidage uncertainty is $\pm 0.01$ ( 3-4% ).

Membrane resistance : As some pore blocking was inevitable the systematic error in this variable is significant but unquantifiable to an acceptable accuracy ( see section 5.1.3 ). However, this inaccuracy did not affect the assessment of steady state equilibrium data. The random error in the resistance can be calculated by equation 3.20 with the following uncertainties: $\delta P_w = 0.01$ bar, $\delta d_o = 0.02mm$, $\delta Q_p = 0.1ml\ min^{-1}$ and $\delta\mu = 10^{-5}N\ s\ m^{-2}$ ( arising from an uncertainty in temperature measurement of $0.5^oC$ ). The error in $R_m$ is around 2% .

Specific cake resistance : The systematic error is large for this variable for the same reasons as those applying to membrane resistance. The random error is calculated from equation 3.21 using the errors determined previously and $\delta( P_b - P_w ) = 0.01$ bar. The result is an error of approximately 3% .

Due to the influence of pore blocking factors an error analysis applied to the dynamic data is inappropriate.